

## TABLE OF CONTENTS

ABSTRACT.....	ii
RELATED PUBLICATIONS .....	iv
DEDICATION.....	v
ACKNOWLEDGEMENT .....	vi
TABLE OF CONTENTS .....	vii
LIST OF FIGURES.....	xi
LIST OF TABLES .....	xviii
<b>1. INTRODUCTION.....</b>	<b>1</b>
1.1 Background.....	1
1.2 Research objectives and scope.....	4
1.2.1 Particle size .....	5
1.2.2 Compaction load.....	6
1.2.3 Time and temperature .....	6
1.2.4 Sintering atmoshpere.....	7
1.3 Outline of thesis .....	7
<b>2. LITERATURE REVIEW OF TITANIUM SINTERING .....</b>	<b>10</b>
2.1 Introduction.....	10
2.2 Basics of sintering process .....	11
2.2.1 Targets of titanium sintering .....	11
2.2.2 Stages of titanium sintering .....	11
2.2.3 Parameters of titanium sintering .....	13
2.3 Manufacturing methods of titanium powders.....	14
2.4 Effect of impurities in titanium powders on sintering.....	16
2.4.1 Carbon and nitrogen .....	16
2.4.2 Hydrogen .....	17
2.4.3 Oxygen.....	18
2.4.4 Chlorides .....	20
2.5 Effect of compaction pressure and methods on sintering.....	23
2.5.1 Cold compaction .....	24

2.5.2	<i>Isostatic pressing</i> .....	25
2.5.3	<i>Equal channel angular pressing (ECAP)</i> .....	27
2.6	Development of low-cost titanium alloys.....	29
2.6.1	<i>Addition of iron</i> .....	29
2.6.2	<i>Addition of silicon</i> .....	33
2.7	Review of novel sintering methods.....	37
2.7.1	<i>Microwave-assisted sintering</i> .....	37
2.7.2	<i>Additive manufacturing (3D printing)</i> .....	41
2.7.3	<i>Spark plasma sintering</i> .....	42
2.8	Problems and challenges in titanium sintering.....	43
<b>3.</b>	<b>EXPERIMENTAL METHODS</b> .....	<b>45</b>
3.1	Experimental materials.....	45
3.2	Compaction and sintering.....	46
3.3	Density measurement and phase determination.....	49
3.4	Metallography preparation.....	49
3.5	Microstructural observation and semi-quantitative compositional analysis.....	50
3.6	Quantitative chemical composition analysis.....	50
3.7	Surface chemistry analysis.....	51
<b>4.</b>	<b>INVESTIGATION OF CHLORIDE IMPURITIES IN KROLL-PROCESSED HYDROGENATED-DEHYDROGENATED TITANIUM POWDERS</b> .....	<b>52</b>
4.1	Introduction.....	52
4.2	Experimental.....	54
4.3	Results and discussion.....	55
4.4	Conclusions.....	64
<b>5.</b>	<b>EFFECT OF CONTAMINANTS ON MICROSTRUCTURAL EVOLUTION AND MECHANICAL PROPERTIES OF COMMERCIAL PURE TITANIUM SINTERED IN A GRAPHITE FURNACE BACKFILLED WITH ARGON ATMOSPHERE</b> .....	<b>65</b>
5.1	Introduction.....	66
5.2	Experimental.....	67
5.2.1	<i>Materials, compaction and sintering</i> .....	67
5.2.2	<i>Characterization</i> .....	68
5.2.3	<i>Mechanical testing</i> .....	68
5.3	Results.....	69
5.3.1	<i>Density measurement</i> .....	69

5.3.2	<i>Metallography of the bulk sintered samples</i> .....	72
5.3.3	<i>Close-up observation of surface contaminants</i> .....	74
5.3.4	<i>Phase characterization of the surface and the interior</i> .....	76
5.3.5	<i>Mechanical properties and fractography</i> .....	78
5.4	Discussion.....	81
5.4.1	<i>Densification</i> .....	81
5.4.2	<i>Effect of interstitials on microstructure evolution and mechanical properties</i> .....	83
5.5	Conclusions.....	88
<b>6.</b>	<b>EFFECT OF RESIDUAL CHLORIDE IMPURITIES ON COMMERCIALY PURE TITANIUM SINTERED IN A GRAPHITE FURNACE</b> .....	<b>90</b>
6.1	Introduction.....	90
6.2	Experimental.....	91
6.3	Results .....	92
6.3.1	<i>Characterization of as-received Ti and Ti-6Al-4V powders</i> .....	92
6.3.2	<i>Surface microstructural observations</i> .....	94
6.3.3	<i>Metallography and microhardness of the bulk sintered specimens</i> .....	98
6.4	Discussion.....	100
6.5	Conclusions.....	103
<b>7.</b>	<b>DEVELOPMENT OF A CLEAN SINTERING ENVIRONMENT IN A GRAPHITE FURNACE</b> .....	<b>105</b>
7.1	Introduction.....	105
7.2	Experimental.....	107
7.3	Results .....	109
7.3.1	<i>Density measurement</i> .....	109
7.3.2	<i>As-sintered surface morphological observation</i> .....	111
7.3.3	<i>Macrostructural cross-section observation</i> .....	114
7.3.4	<i>Mechanical properties and fractural morphology</i> .....	115
7.4	Discussion.....	118
7.4.1	<i>Origin of carbon source</i> .....	118
7.4.2	<i>Theoretical calculation of scale thickness based on Fick's second law</i> .....	119
7.4.3	<i>Effect of contamination reduction solutions</i> .....	123
7.4.4	<i>Role of sintering atmosphere</i> .....	124
7.5	Conclusions.....	124

<b>8. PRESSURELESS SINTERING OF Ti-Al-V-Fe TITANIUM ALLOYS FROM ULTRAFINE HYDROGENATED-DEHYDROGENATED TITANIUM POWDER.....</b>	<b>126</b>
8.1 Introduction.....	126
8.2 Experimental.....	129
8.2.1 <i>Materials</i> .....	129
8.2.2 <i>Theoretical density measurement</i> .....	129
8.2.3 <i>Press-and-sinter</i> .....	131
8.2.4 <i>Characterization and mechanical testing</i> .....	132
8.3 Results .....	133
8.3.1 <i>Characteristics of as-received powders</i> .....	133
8.3.2 <i>Densification</i> .....	135
8.3.3 <i>Microstructure observation and compositional analysis</i> .....	137
8.3.4 <i>Phase determination</i> .....	142
8.3.5 <i>Mechanical properties and fractography</i> .....	143
8.4 Discussion.....	146
8.4.1 <i>Microporosity formation</i> .....	146
8.4.2 <i>Macroporosity formation</i> .....	149
8.4.3 <i>Microstructural evaluation and phase transformation</i> .....	155
8.4.4 <i>Mechanical properties</i> .....	156
8.5 Conclusions.....	159
<b>9. OVERALL SUMMARY AND KEY FINDINGS.....</b>	<b>161</b>
<b>10. CONCLUSIONS .....</b>	<b>164</b>
<b>11. FUTURE WORKS.....</b>	<b>167</b>
11.1 Effect of chloride additions on titanium sintering .....	167
11.2 Effect of sintering atmosphere pressures on titanium sintering in a graphite furnace ..	168
11.3 Development of titanium alloys with ultrafine titanium powders using oxygen getter	168
<b>12. REFERENCES.....</b>	<b>170</b>

## LIST OF FIGURES

Figure 1-1: Schematic graphs of crystal structures of titanium: (a) hcp $\alpha$ phase and (b) bcc $\beta$ phase [1, 3].....	3
Figure 2-1: Macrographs of sintered titanium specimens at different sintering temperatures with a constant holding time of 4 hours: a) 1100 °C, b) 1250 °C and c) 1400 °C (under polarised light) 13	
Figure 2-2: TEM images of Ti-6Al-4V alloy containing 1.2 wt% hydrogen: (a) hydride laths and (b) corresponding SAED pattern of hydride [64] .....	18
Figure 2-3: Effect of oxygen on the elongation (a) and ultimate tensile strength (b) of C.P. Ti and Ti-6Al-4V [61].....	19
Figure 2-4: SEM images showing shells consisting of fine NaCl particles in macropores: (a) Ti-6Al-4V; (b) Ti-6Al-4V-10%TiB. Both samples contained 800 ppm Cl and were sintered at 1300 C for 16 hours [67] .....	21
Figure 2-5: Finite elements (FE) simulation of relative density distribution during alumina compaction: (a) initial condition, and a total height reduction of (b) 20%, (c) 40% and (d) 56% [76] .....	23
Figure 2-6: Sintered densities of -100 mesh titanium powder after cold compaction at 100 – 800 MPa. The full sigmoidal curve is a least-squares fit to the 400 MPa data except those at high values of the delta integral, where close to the fully dense [78] .....	24
Figure 2-7: Optical micrographs of (a) pre-alloyed Ti-6Al-4V after press-and-sinter, (b) further HIP at 1000 °C of Ti-6Al-4V, (c) pre-alloyed Ti-3Al-2.5V after press-and-sinter and (d) further HIP at 1000 °C of Ti-3Al-2.5V [79].....	26
Figure 2-8: Equal channel angular pressing (ECAP) of powder: (a) unit for elevated-temperature ECAP with back pressure; (b) schematic of the process [81].....	27
Figure 2-9: Influence of shear on pore size and distribution and realignment of large and fragmented particles after ECAP with 263 MPa of back pressure at room temperature [81] .....	28

- Figure 2-10: The schematic of the phases present in sintered Ti-7Fe under different cooling processes: furnace cooling (1150 °C - 740 °C/640 °C/550 °C) + holding for 24 hours (740 °C/640 °C/550 °C) + fan cooling (740 °C/640 °C/550 °C – 60 °C) [97]..... 31
- Figure 2-11: TEM images of sintered Ti-7Fe under different cooling processes: furnace cooling (1150 °C - 740 °C/640 °C/550 °C) + holding for 24 hours ( a: 740 °C, b: 640 °C, c: 550 °C) + fan cooling (740 °C/640 °C/550 °C – 60 °C) [97] ..... 32
- Figure 2-12: Effect of iron content on the microstructure of C.P. Ti under polarized light with different iron content: (a) 0.15 wt% Fe; (b) 0.3 wt% Fe [1]..... 33
- Figure 2-13: TEM analysis of the fine precipitates in the alpha phase: (a) a bright-field image of sintered Ti-3Fe-xSi ( $x \leq 1$ ), (b) and (c) SAED patterns taken from the marked areas in (a) [99]... 34
- Figure 2-14: Tensile strengths and elongation of Ti-3Ni-xSi sintered at 1300 °C with a holding time of 120 min in vacuum [100]..... 35
- Figure 2-15: Optical microstructures of Ti-3Ni-xSi sintered at 1300 °C with a holding time of 120 min in vacuum (a) 0 wt% Si, (b) magnification of the marked area in (a), (c) 1 wt% Si, (d) 1.5 wt% Si, (e) 2 wt% Si, and (f) 3 wt% Si [100]..... 36
- Figure 2-16: Variations in temperature, vacuum and microwave powder reflection ratio during temperature fluctuations. (b) and (c) are images of specimens when electric arcs are discharging (D) and extinguishing (E) marked in (a). TiH<sub>2</sub> powders were applied here.[103] ..... 38
- Figure 2-17: Tensile mechanical properties of specimens sintered by microwave-assisted (MW) and conventionally vacuum (CV) under different conditions. (a) CP-Ti; (b) Ti-6Al-4V, compacted from blends of elemental Ti and Al powders and Al-V master alloy powder (particle size <150 μm) at 600 MPa [39] ..... 39
- Figure 2-18: Optical micrographs and corresponding fractographs of microwave-sintered C.P. titanium (< 150 μm) and Ti-6Al-4V (<63 μm Ti, 75-150 μm Al-V, 3 μm Al). Specimens were pressed at 600 MPa and sintered at 1300 C with a soaking of 2 hours [39]..... 40

Figure 2-19: Illustration of the selective laser sintering process [117] .....	41
Figure 2-20: Schematic of spark plasma discharge setup [119] .....	43
Figure 3-1: Pressureless/pressure-assisted sintering experiment process flow chart (CIP is optional).....	47
Figure 3-2: Schematic diagram of high-temperature graphite furnace .....	47
Figure 3-3: Illustration of heating curve for titanium sintering .....	48
Figure 4-1: As-received HDH Ti -200 mesh powder: (a) XRD phase determination; (b) particle size distribution [135].....	56
Figure 4-2: Jigsaw-like particles on the surface of as-received HDH titanium powders: a) back-scattered electron image; b) high-magnification secondary electron image of selected area on the surface of one Ti particle; c) EDS compositional analysis [135] .....	57
Figure 4-3: Surface chemistry of as-received titanium HDH powders: a) survey scan; b) Mg 1s; c) Cl 2p; d) Ti 2p; e) O 1s [135] .....	59
Figure 4-4: Schematic diagram of the originating process of chloride impurities in HDH titanium powders [135] .....	61
Figure 4-5: Thermogravimetric analysis (TGA) of hydrated magnesium chloride powders [135]	62
Figure 4-6: Dehydration mechanism of hydrated magnesium chlorides [135] .....	63
Figure 5-1: Schematic preparation of slices taken from the as-sintered cylinder.....	69
Figure 5-2: Relative sintered densities (a) and densification levels (b) under various sintering conditions.....	71
Figure 5-3: Macrographs of cross-sections of sintered specimens at different sintering conditions: a) 1100 °C, 4 hours and b) 1250 °C, 4 hours and c) 1400 °C, 4hours .....	72
Figure 5-4: Macrographs of cross sections of sintered specimens at various sintering conditions using crossed polarized light.....	73

Figure 5-5: Surface morphologies and semi-quantitative EDS analysis of as-received Ti powder (a, d), sintered specimen surface at 1250 °C with a 4-hour holding (b, e) and sintered specimen surface at 1400 °C with a 4-hour soaking (c, f) .....	75
Figure 5-6: XRD patterns of the surface (a) and cross-sections (b) of sintered Ti specimens with a holding time of 4 hours.....	77
Figure 5-7: Representative engineering stress-strain curves for slices prepared from different positions.....	79
Figure 5-8: Fracture surfaces of tensile slices from sintered titanium samples: (a) S4, (b) S5, (c) S6, and (d) S7.....	80
Figure 5-9: Schematic of the formation process of the scale and cracks .....	84
Figure 5-10: Phase constitutes of tensile slices manufactured from different positions of the large cylinder (a); fracture surface of S3 (b) .....	86
Figure 6-1: Micrographs of -200 mesh (a) Ti powder and (b) Ti-6Al-4V alloy powder [152].....	93
Figure 6-2: XRD patterns of as-received powders.....	94
Figure 6-3: Micrographs of the sintered surfaces of Ti (a, b) and Ti-6Al-4V (c and d). Both samples were sintered at a temperature of 1250 °C for 6 hours[152] .....	95
Figure 6-4: Spheres on the surface of sintered Ti at a) 1100 °C, 4 hours; b) 1250 °C, 4 hours; c) 1400 °C, 4 hours.....	96
Figure 6-5: Broken spheres on the surface of Ti specimens sintered at a) 1100 °C, 6 hours; b) 1250 °C, 4 hours.....	97
Figure 6-6: Subsurface micrograph morphology of Ti specimens sintered at 1100 °C holding for 4 hours .....	98
Figure 6-7: Macrographs of Cross-section of sintered specimens at different sintering conditions: a) 1100 °C, 4 hours and b) 1400 °C, 4 hours.....	99



Figure 6-8: Macrograph of cross section (a) and corresponding EDS data and microhardness (b) of the sintered titanium (1100 °C, 6 hours) [152] .....	100
Figure 6-9: Process modelling of the effect of residual chlorides on titanium sintering .....	101
Figure 6-10: Relative density of compacts and sintered specimens under different sintering temperatures for C.P. Ti and pre-alloyed Ti-6Al-4V. All samples were sintered for 6 hours ....	103
Figure 7-1: Different solutions for titanium sintered in a graphite furnace: a) control solution: exposed directly to the furnace atmosphere on a BN plate; b) solution A: placed in a BN tray wrapped by Al <sub>2</sub> O <sub>3</sub> beads in a large-sized Al <sub>2</sub> O <sub>3</sub> crucible; c) solution B: placed in a Mo crucible wrapped by 1mm-diameter titanium particles served as contamination getter .....	108
Figure 7-2: Materials applied in the experimental setup: a) compacts; b) BN tray; c) titanium contamination getter; d) Al <sub>2</sub> O <sub>3</sub> beads.....	109
Figure 7-3: (a) sintered densities and (b) densification levels of Ti and Ti-6Al-4V specimens sintered under different protection solutions at the temperature of 1250 °C in vacuum with a holding time of 4 hours.....	110
Figure 7-4: As-sintered surface morphologies of Ti specimens sintered under vacuum using different contamination-reduction solutions.....	112
Figure 7-5: as-sintered surface of Ti specimens sintered with contamination-reduction solution A (a) and high magnification picture of grain boundary (b) and corresponding EDS spectrum (c)	113
Figure 7-6: Macrostructural cross-section observations of titanium specimens sintered under vacuum with (a) control solution and (b) contamination reduction solution B .....	114
Figure 7-7: Representative engineering and true stress-strain curves for Ti specimens sintered at varied sintering atmospheres with the same contamination-reduction solution A .....	116
Figure 7-8: Fractural surfaces at varied sintering atmospheres (a) atmosphere sintering and (b) vacuum sintering for sintered titanium using contamination-reduction solution A at the temperature of 1250 °C with a holding time of 4 hours .....	117

Figure 7-9: Phase diagram of titanium-carbon [167] .....	120
Figure 7-10: Schematic graph of different layers formed at sintering temperature and room temperature .....	122
Figure 8-1: Heating schedule for blended elemental sintered titanium alloys .....	131
Figure 8-2: SEM images and particle size distribution of ultrafine Ti (a) 60Al-40V master alloy (b) and Fe powders (c).....	134
Figure 8-3: XRD patterns of as-received powders.....	135
Figure 8-4: Relative sintered density (a) and densification level (b) as a function of iron content for samples sintered at different temperatures .....	136
Figure 8-5: Cross-sectional SEM images of sintered titanium alloys at various temperatures and compositions .....	137
Figure 8-6: EDS line scanning of blended elemental Ti-6Al-4V specimens sintered at (a) 1150 °C and (b) 1250 °C .....	139
Figure 8-7: EDS mapping of blended elemental Ti-6Al-4V specimens sintered at (a) 1150 °C and (b) 1250 °C .....	140
Figure 8-8: EDS mapping (a) and EDS line scanning (b) of Ti-3.6Al-2.4V-4Fe sintered at 1350 °C.....	141
Figure 8-9: XRD patterns of (a) Ti-6Al-4V sintered at various temperatures and (b) Ti-Al-V-Fe of various Fe concentrations sintered at 1350 °C .....	143
Figure 8-10: Tensile strength (a) and elongation (b) of sintered titanium alloys as a function of master alloy powder content at various temperatures .....	144
Figure 8-11: Representative fracture morphologies of Ti-2.4Al-1.6V-6Fe sintered at 1250 °C: (a) macropores and (b) brittle fracture surface.....	145
Figure 8-12: SEM fractographs with micropores of tensile specimens sintered at various temperatures and compositions.....	147

Figure 8-13: Temperature dependence of ratio of interdiffusion coefficients to selfdiffusion coefficient of $\beta$ -Ti .....	149
Figure 8-14: Macropores shown in fracture surface of Ti-6Al-4V specimens sintered at 1150 °C .....	150
Figure 8-15: The dependence of evaporation rate and saturated vapour pressure on temperature .....	154
Figure 8-16: Dependence of oxygen content on median particle size of HDH titanium powder	157

## LIST OF TABLES

Table 2-1: Classification of solid-state sintering stages .....	12
Table 2-2: Characteristics of different feedstocks for titanium sintering .....	15
Table 2-3: Solubility of carbon and nitrogen in alpha titanium and beta titanium .....	16
Table 2-4: Mechanical properties of low-cost titanium alloys in comparison with Ti-6Al-4V alloys[87] .....	30
Table 4-1: Impurity contents (O, C, N, H) in C.P. Ti for ASTM Grade 4 specification and as-measured titanium powder[135] .....	55
Table 5-1: Tensile mechanical properties of titanium slices prepared from a large-sized cylinder sintered at 1250 °C with a holding time of 4 hours .....	78
Table 5-2: Densities and densification level for large cylinder prepared for tensile testing .....	82
Table 5-3: Interstitial contents of different slices and as-received titanium powders.....	85
Table 5-4: Relative sintered densities for slices taken from the large cylinder .....	87
Table 6-1: C, H, O, N, Mg, Cl contents determined in as-received powders .....	93
Table 6-2: Semi-quantitative testing contents of spheres on the surface of Ti specimens sintered at varied conditions .....	97
Table 7-1: Relative sintered densities of C.P. Ti compacts sintered at atmosphere and vacuum respectively at the sintering temperature of 1250 °C with a holding time of 4 hours.....	111
Table 7-2: Tensile mechanical properties at varied contamination-reduction solutions and sintering atmospheres for titanium compacts sintered at the temperature of 1250 °C with a holding time of 4 hours.....	115
Table 8-1: Impurity levels, particle morphology and particle size for as-received powdes.....	129
Table 8-2: Selfdiffusion of $\beta$ -Ti and Interdiffusion of Al, V and Fe in Pure $\beta$ -Ti [171] .....	148

## Co-Authorship Form

This form is to accompany the submission of any PhD that contains research reported in published or unpublished co-authored work. **Please include one copy of this form for each co-authored work.** Completed forms should be included in all copies of your thesis submitted for examination and library deposit (including digital deposit), following your thesis Acknowledgements.

Please indicate the chapter/section/pages of this thesis that are extracted from a co-authored work and give the title and publication details or details of submission of the co-authored work.

Chapter 4 of this thesis is extracted from "Yu, C.Z. and M.I. Jones, Investigation of chloride impurities in hydrogenated-dehydrogenated Kroll-processed titanium powders. Powder Metallurgy, 2013. 56(4): p. 304-309".

Nature of contribution by PhD candidate

experiment design, operation and analysis, manuscript preparation

Extent of contribution by PhD candidate (%)

85


### CO-AUTHORS

Name	Nature of Contribution
Dr. Mark Ian Jones	supervision of the project and writing polishing

### Certification by Co-Authors

The undersigned hereby certify that:

- ❖ the above statement correctly reflects the nature and extent of the PhD candidate's contribution to this work, and the nature of the contribution of each of the co-authors; and
- ❖ in cases where the PhD candidate was the lead author of the work that the candidate wrote the text.

Name	Signature	Date
Dr. Mark Ian Jones		16/09/2013
		Click here
		Click here
		Click here
		Click here
		Click here

## Co-Authorship Form

This form is to accompany the submission of any PhD that contains research reported in published or unpublished co-authored work. **Please include one copy of this form for each co-authored work.** Completed forms should be included in all copies of your thesis submitted for examination and library deposit (including digital deposit), following your thesis Acknowledgements.

Please indicate the chapter/section/pages of this thesis that are extracted from a co-authored work and give the title and publication details or details of submission of the co-authored work.

Chapter 6 of this thesis is extracted from "Yu, C.Z., P. Cao, and M.I. Jones, Effect of Contaminants on Sintering of Ti and Ti-6Al-4V alloy Powders in an Argon-Back-Filled Graphite Furnace. Key Engineering Materials, 2012. 520: p. 139-144".

Nature of contribution by PhD candidate	experiment design, operation and analysis, manuscript preparation
Extent of contribution by PhD candidate (%)	85

### CO-AUTHORS

Name	Nature of Contribution
Dr. Peng Cao	writing polishing and assistance to develop the sphere-formation discussion
Dr. Mark Ian Jones	supervision of the project and writing polishing

### Certification by Co-Authors

The undersigned hereby certify that:

- ❖ the above statement correctly reflects the nature and extent of the PhD candidate's contribution to this work, and the nature of the contribution of each of the co-authors; and
- ❖ in cases where the PhD candidate was the lead author of the work that the candidate wrote the text.

Name	Signature	Date
Dr. Peng Cao		18/09/2013
Dr. Mark Ian Jones		16/09/2013
		Click here
		Click here
		Click here
		Click here

## Co-Authorship Form

This form is to accompany the submission of any PhD that contains research reported in published or unpublished co-authored work. **Please include one copy of this form for each co-authored work.** Completed forms should be included in all copies of your thesis submitted for examination and library deposit (including digital deposit), following your thesis Acknowledgements.

Please indicate the chapter/section/pages of this thesis that are extracted from a co-authored work and give the title and publication details or details of submission of the co-authored work.

Sections 5.3.1, 5.3.2 and 5.3.3 are extracted from "Yu, C.Z., P. Cao, and M.I. Jones, Optimization of parameters for pressureless sintering of titanium and Ti-6Al-4V powders by a Taguchi method, in the 12th World Conference on Titanium, I. Zhou, et al., Editors. 2011, Science Press Beijing: Beijing, China. p. 1719-1721".

Nature of contribution by PhD candidate	experiment design, operation and analysis, manuscript preparation
Extent of contribution by PhD candidate (%)	85



### CO-AUTHORS

Name	Nature of Contribution
Dr. Peng Cao	co-supervision of the project and writing polishing
Dr. Mark Ian Jones	supervision of the project and writing polishing

### Certification by Co-Authors

The undersigned hereby certify that:

- ❖ the above statement correctly reflects the nature and extent of the PhD candidate's contribution to this work, and the nature of the contribution of each of the co-authors; and
- ❖ in cases where the PhD candidate was the lead author of the work that the candidate wrote the text.

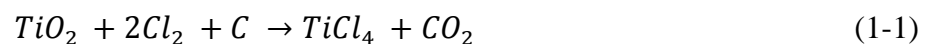
Name	Signature	Date
Dr. Peng Cao		18/09/2013
Dr. Mark Ian Jones		16/09/2013
		Click here
		Click here
		Click here
		Click here

## 1. INTRODUCTION

### 1.1 Background

Titanium is the fourth most abundant structural metal element after aluminium, iron and magnesium in the Earth's crust at a level of around 0.6 %. It has a high strength to weight ratio, large fracture toughness, excellent corrosion resistance and biocompatibility as well as good creep resistance (up to 550 °C), which makes titanium and its alloys attractive for many applications especially in aerospace and biomedical instruments [1, 2]. It exists in nature mainly as a state of mineral sands and rutile mainly composed of titanium oxide, and never found in a pure state due to its chemical activity which makes it difficult to extract pure titanium from ores and realise its commercial potential. This is evidenced by the very origin of the name Titanium, initially discovered by the British mineralogist William Gregor in Cornwall (England) in 1791, it was so named four years later by the Berlin chemist Martin Heinrich Klaproth because the difficulty in extracting titanium from ore was considered akin to the Titans in Greek mythology who were imprisoned by their father [3].

Pure titanium metal was first isolated in 1910 by Matthew Albert Hunter from Rensselaer Polytechnic Institute in Troy (New York, USA) through reduction of titanium tetrachloride ( $TiCl_4$ ) with sodium in a steel bomb, leading to the so-called Hunter process [4]. The starting materials were rutile ( $TiO_2$  is the main component), coke and  $Cl_2$ , and the reactions for the formation of titanium metal are illustrated as follows:





In 1937 the process was updated and almost fully replaced by another effective method named the Kroll process invented by William Justin Kroll from Luxembourg [5]. The largest difference in the two processes is the replacement of sodium by less expensive magnesium [1]:



In this Mg-reduction method ~0.5 kg titanium powder or sponges were produced per batch [5]. Meanwhile, 14 binary titanium alloys were compacted and sintered in argon by Kroll, which is the first documented attempt to fabricate titanium alloys with powder [5]. Based on Kroll's early work, the first commercial titanium production was developed by DuPont using the technology from Bureau of Mines with a quantity of 3 tonnes in 1948 [4, 5]. Because of the significance of his efforts, Kroll is recognised as the father of the Ti industry.

Pure titanium crystallizes at low temperature in a hexagonal close packed (hcp) structure, known as  $\alpha$  titanium. After heating to a temperature of 882 °C ( $\beta$ -transus temperature) or above, the body-centered cubic (bcc) structure is stable and referred to as  $\beta$  titanium. Figure 1-1 highlights the difference between the hcp and bcc structures of the titanium polymorphs with lattice parameters labelled [1, 3].

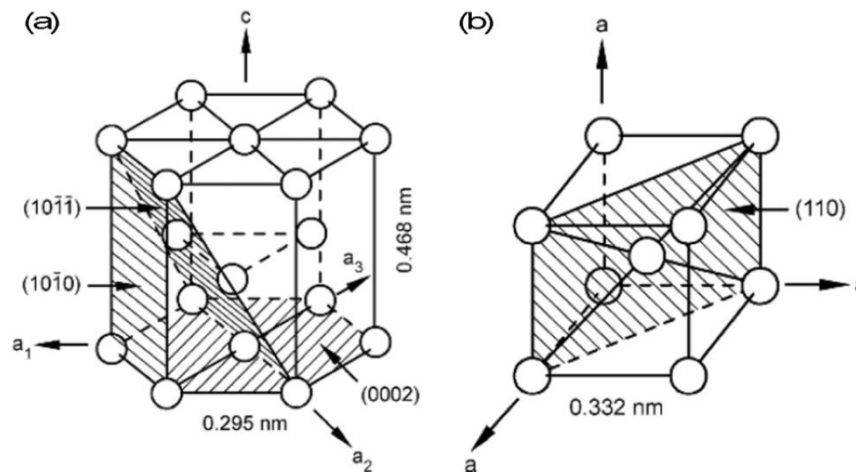


Figure 1-1: Schematic graphs of crystal structures of titanium: (a) hcp  $\alpha$  phase and (b) bcc  $\beta$  phase [1, 3]

The knowledge of crystal structure affords understanding of the mechanical property differences between the alpha and beta titanium phases [3]. For example, there are 48 slip systems per cell of beta titanium while there are only 3 slip systems for alpha titanium per unit cell. This can be ascribed as one reason why beta titanium has high ductility.

The affordability of Ti is the main obstacle to a wider application arising from the cost of both raw materials and manufacturing processes [6, 7]. Titanium and titanium alloys processed by traditional methods such as casting and/or forging, normally produce an average material utilisation factor of only 10 %-15 % for finished components [2, 5]. The target of “Project Black Ti” introduced by Lockheed Martin is to reduce the buy-to-fly ratio to 5:1 for the F-35 joint strike fighter (JSF) program [8]. The buy-to-fly ratio is the weight ratio between the raw material required and the finished components. It can be seen that this would still produce 80% scrap. The ability of near net shaping and compositional controllability makes powder metallurgical technology promising as a low-cost solution for titanium production [9, 10]. This is the main driving force for the R&D of titanium powder metallurgy. In recent major milestone

developments to the powder metallurgical titanium industry, near-net-shape Ti-6Al-4V products manufactured by Dynamet Technology, Inc. have been approved for commercial airplane components by Boeing [11, 12], and the manufacture of titanium powder metal products has received standardized quality management system AS9100/ISO9001 certification on April 2013 [12]. However, there are still many issues to be addressed for understanding of titanium sintering process and these will be discussed in the following chapter.

## 1.2 Research objectives and scope

The general objective of this project is to investigate the fundamental relationships and mechanisms underlying sintering of c. p. titanium and titanium alloys such as the commonly used Ti-6Al-4V. Specifically, this research work investigates the effects of material and processing parameters on densification, microstructure and mechanical properties of sintered specimens, which includes the effects of

- i) particle size
- ii) sintering temperature
- iii) sintering atmosphere
- iv) alloy powder composition
- v) holding time
- vi) compaction pressure
- vii) chloride impurities in powders

These sintering parameters such as particle size, holding time and etc. as well as impurities from as-received powders and sintering atmosphere have a combined influence on sintering of titanium and its alloys. According to solid-state sintering theory, there are many sintering mechanisms of mass transport basically consisting of surface transport and bulk transport [13]. However, only bulk-transport-controlled sintering results in densification or shrinkage such as lattice diffusion and grain boundary diffusion [14]. The linear shrinkage ( $\Delta L/L$ ) for lattice diffusion and grain boundary diffusion can be given below according to the classic two-sphere model [15]:

$$\text{Lattice diffusion:} \quad \Delta L/L = (20\gamma V_v D_1 / \sqrt{2} kT)^{2/5} t^{2/5} / r^{6/5} \quad (1-4)$$

$$\text{Grain boundary diffusion:} \quad \Delta L/L = (3\gamma d V_v D_{gb} / kT)^{1/3} t^{1/3} / r^{4/5} \quad (1-5)$$

where  $\gamma$  is surface energy,  $V_v$  volume of the vacancy,  $D_1$  self-diffusion coefficient,  $k$  Boltzmann constant,  $T$  absolute temperature (K),  $t$  sintering time,  $r$  particle radius,  $d$  boundary thickness,  $D_{gb}$  diffusion coefficient for grain boundary diffusion. According to the above equations, it can be realised that the densification is proportional to sintering temperature and sintering time and inversely proportional to particle size. It can also be seen that shrinkage is more strongly dependent on particle size than sintering temperature and time. This means that particle size has a larger effect on densification than the other two sintering parameters, which is in good agreement with the literature [13]. For solid-state sintering of Ti and Ti alloys, the specific effects of sintering parameters are described below:

### 1.2.1 Particle size

Particle size reduction increases the surface to volume ratio and surface free energy thereby accelerating the sintering process and enhancing densification. However the oxygen content

derived from thin titanium oxide layer on the particle surface increases with decreasing particle size, which is detrimental to the mechanical properties such as ductility although there is no apparent correlation between sintering densification and oxygen content. The size fractions of titanium powders used in PM are usually within the range from 5 to 500 micrometers. The fractions  $<150\ \mu\text{m}$  and  $<45\ \mu\text{m}$  are mostly commonly reported [16]. Smaller particle sizes like less than  $20\ \mu\text{m}$  are expected to be used in future, if the oxygen content can be controlled to the required extent.

### 1.2.2 Compaction load

In order to achieve the desired specimen shape, proper compaction pressure and die design are necessary. Generally higher uniaxial compaction loads lead to higher green density, better dimensional control and less sintering shrinking, and therefore it can lead to better sintering densification. In order to yield high sintered density ( $\sim 98\%$  of theoretical density), extremely high uniaxial compaction pressure was adopted up to 1800 MPa to boost the green density ( $\sim 90\%$  of theoretical density) of Ti-6Al-4V compacts with particle size  $< 150\ \mu\text{m}$  [6, 17]. However, such high compaction pressure is not commonly seen in titanium industrial production. Literature indicates uniaxial compaction pressures in the range of 200-700 MPa have been generally utilized by many researchers for titanium sintering [18-21]. It is also reported that in industry CIP pressure up to 413 MPa is already able to give sufficient green density ( $\sim 85\%$  theoretical density) [22].

### 1.2.3 Time and temperature

Sintering densification is sensitive to sintering temperature, since the sintering process is a diffusion-controlled process highly dependent on the temperature. It is reported that green compacts sintered at the temperature ranging from  $1100^\circ\text{C}$  to  $1400^\circ\text{C}$  [19, 23-26]. Long-term soaking time at elevated temperature can benefit sintering densification; however the problem of

associated grain growth and economic cost cannot be neglected. A solution to find novel sintering method such as microwave sintering can essentially lower the holding time and raise the sintering efficiency. In addition, short holding times are believed to be able to depress grain growth and raise the corresponding static mechanical properties.

#### 1.2.4 Sintering atmosphere

The nature of the sintering atmosphere may play a role in the densification behaviour of the samples. Titanium sintering can be carried out under vacuum or in an inert gas atmosphere. Most of the available literature describes production of Ti alloy components by vacuum sintering [19-21, 23, 25-29] leading to better mechanical properties and higher densification in contrast with inert-gas sintering. However, vacuum sintering has a fatal drawback that it is not accessible to realize the aim of industrial continuous production. Therefore, the cost of production is more expensive compared with inert gas sintering. Currently, there is little work carried out to describe the effects of inert gas atmosphere or pressure, and also there is a lack of knowledge surrounding the mechanism of vacuum sintering and argon sintering especially under high pressures. Whether high pressure inert gas can lead to larger densification is an issue to be discussed.

### 1.3 Outline of thesis

In order to realise the above research targets, commercially pure titanium and titanium alloy powders have been sintered under different atmospheres including argon and vacuum, and sintered in different kinds of furnaces such as graphite-heating-element and molybdenum-heating-element furnaces.

Chapter 2 describes a literature review of titanium sintering. After describing the sintering process, several specific problematic issues are raised and discussed accordingly in regard to

titanium sintering. Addressing some of these issues forms the basis of the following experimental chapters. A general description of common experimental methodologies employed throughout the thesis are presented in Chapter 3, with more detailed, specific experimental setup and analytical techniques described in each individual chapter.

In order to lower the overall cost of titanium component production, hydrogenated-dehydrogenated Kroll-processed titanium powders are generally much cheaper than powders manufactured from other approaches [7]. However, the densification and mechanical properties of specimens sintered with HDH titanium powders are always adversely affected by the chloride impurities [30]. Therefore, it is necessary to investigate the chloride impurities in hydrogenated-dehydrogenated Kroll-processed titanium powders. This work is presented in Chapter 4.

Chapter 5 describes an assessment on the suitability of isothermal atmospheric sintering of commercially pure titanium powders in a graphite furnace under argon. It was found that a contaminated scale formed on the surface of titanium bulks during sintering. Such contamination is not beneficial to titanium sintering, and this chapter discusses the effect of contaminants on microstructural evolution and mechanical properties.

The use of a graphite furnace may be beneficial, but the work presented in Chapter 5 showed that the samples tended to be contaminated, particularly at the external surfaces exposed to the furnace environment. Sintering of both c. p. Ti and pre-alloyed Ti-6Al-4V powders showed differing features that are considered to be related to the residual chloride impurities investigated in Chapter 4. Analysis of the effect of residual chlorides on titanium sintering and a possible formation mechanism of different surface features form the basis of Chapter 6.

The main contamination observed in the sintering of these samples in the graphite furnace under argon, potentially arising from the sintering environment (graphite heating element and liners, and small amount of nitrogen and oxygen coming from the argon gas and/or poor vacuum level

are detrimental to poor densification (only around 85-90 % of theoretical density for c. p. Ti at the sintering temperature of 1100 °C and 1250 °C) and low mechanical properties (almost no ductility for specimens exposed to the furnace atmosphere). Chapter 7 describes attempts to reduce the contamination through employing different crucible arrangements to reduce the contact area with furnace atmosphere and utilize contamination gettering and investigates the effects of such methods on the densification and mechanical properties of sintered specimens.

Chapter 8 discusses the effects of particle size of Ti powders and the presence of alloying elements on sintering of Ti alloys. This is achieved through the use of powders prepared by a novel ultrafine titanium powder production method and the development of potentially low cost Ti-Al-V-Fe titanium alloys from ultrafine hydrogenated-dehydrogenated titanium powder by pressureless sintering.

An overall summary of the work is given in Chapter 9 and conclusions are presented in Chapter 10. Chapter 11 provides insights in to where future research efforts may be focussed.



## 2. LITERATURE REVIEW OF TITANIUM SINTERING

Chapter 1 gave a general introduction to this work and highlighted the issues to be addressed in this thesis. This chapter presents a general literature review in order to introduce the current state of knowledge of titanium sintering. More detailed literature relevant to each of the following chapters is reserved for the introductions to those chapters.

### 2.1 Introduction

Powder metallurgical technology is defined as the art and science of producing powders and of utilizing powders for the production of bulk materials and shaped objects [13, 31]. The concerns of feedstock powder handling processes include particle size distribution, particle shape, microstructure, impurities etc. Powder metallurgical processes, as related to the formation of bulk materials from powder, typically consist of three major steps. Initially, the powder is sieved to obtain the desired particle size distribution as feed material, followed by cold or hot compaction. In the compaction stage, the powder is pressed into a die or a mould to produce a cohesive structure near the dimensions of the final products (green body). The ultimate stage is the complicated but crucial process of sintering; a thermal treatment for bonding particles together into a strong solid structure via mass transportation that occurs largely at the atomic level [14]. Stages from powder handling, compaction and sintering are also present in specific titanium sintering.

## **2.2 Basics of sintering process**

### 2.2.1 Targets of titanium sintering

Sintering is classified into two types described as either solid phase sintering or liquid phase sintering. The process is defined as solid state sintering when the powder compact is sintered wholly in a solid state at the sintering temperature, while there is liquid phase present in liquid state sintering [32]. Most cases of titanium sintering belong to solid state sintering, such as sintering of c. p. titanium powders and sintering of pre-alloyed Ti-6Al-4V powders [33, 34]. Sintering can also be divided into pressureless sintering and pressure-assisted sintering depending on whether additional pressure is applied during sintering. Both can be seen in titanium sintering [9, 22, 35-38]. Pressure-assisted sintering can help to eliminate internal porosity and therefore densify specimens, while pressureless sintering is generally low-cost and beneficial to density homogeneity in conjunction with hot pressing [5].

The target of titanium sintering is to produce required near-net or net shapes with desired mechanical properties. Through suitably controlled sintering processes, the engineering properties such as strength, ductility, conductivity, magnetic permeability and corrosion resistance can be improved accordingly [14].

### 2.2.2 Stages of titanium sintering

The classic stages of sintering are outlined in Table 2-1 in regard to geometric categories for analysing the mass flow process [14].

Table 2-1: Classification of solid-state sintering stages

Stage	Process	Densification	Coarsening
Adhesion	Particle contact	None	None
Initial	Neck growth	Small	Small
Intermediate	Pore rounding and elongation	Significant	Grain growth
Final	Pore closure	Slow	Extensive grain and pore growth

Initial particle contacting is created in green compacts since powders are pressed together. At this stage, there is no grain or pore growth. After heating green compacts to a certain temperature, initial-stage sintering occurs and small amounts of densification and coarsening of grains and pores can be expected. In the intermediate-stage sintering, the pore structure becomes rounded and significant densification occurs. Since pores have a pinning effect against grain growth, the grain growth is not strong at this stage [14]. As the pores shrink and become isolated, extensive grain growth is observed in the final-stage of sintering because less grain boundary pinning occurs in comparison with the previous sintering stages. The process is also witnessed by solid-state titanium sintering conducted by the author as illustrated in Figure 2-1. C. p. HDH titanium powders ( $<75 \mu\text{m}$ ) in Figure 2-1 were sintered at three different temperatures under argon atmosphere with a pressure of 1.1 atm ( $1.11 \times 10^5 \text{ Pa}$ ) in a graphite furnace. More detailed experimental work of these samples is described in Chapter 5, but these images are presented here to describe the general sintering process.

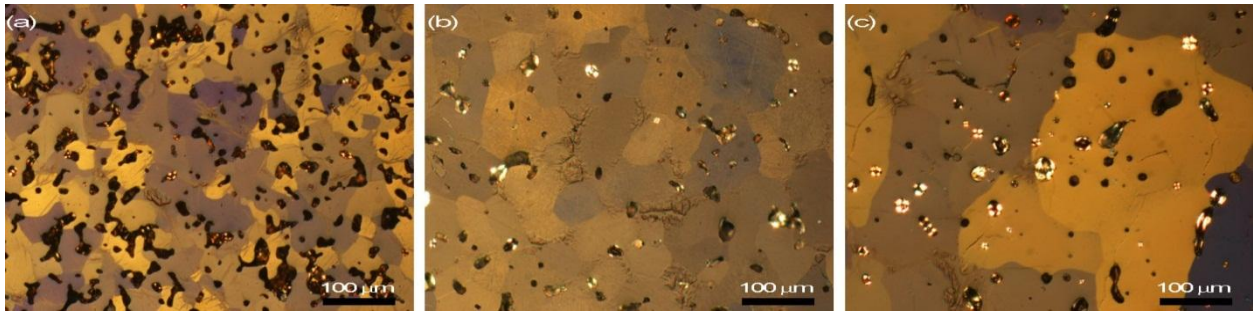


*Figure 2-1: Macrographs of sintered titanium specimens at different sintering temperatures with a constant holding time of 4 hours: a) 1100 °C, b) 1250 °C and c) 1400 °C (under polarised light)*

Remarkable grain growth is observed at the final-stage sintering when sintered at a temperature of 1400 °C with a holding time of 4 hours in Figure 2-1 (c) in comparison with lower temperatures illustrated in Figure 2-1 (a) and (b). Porosity also decreased with increasing sintering temperature from 1100 °C to 1400 °C, which means the densification increased with the increment of temperature. Spherical pore closure was also witnessed at the final-stage sintering shown in Figure 2-1 (c) and the size of some pores were even larger than at lower temperature shown in Figure 2-1 (b). Such pore coarsening is suggested to result from the vacancy flow since large pores can be the vacancy sink and neighbouring pores are vacancy source [13].

### 2.2.3 Parameters of titanium sintering

The initial stage of sintering can be empirically modelled in terms of isothermal neck growth as measured by the neck size ratio  $X/D$  [13, 14]:

$$(X/D)^n = Bt/D^m \quad (2-1)$$

where  $D$  is the particle diameter,  $X$  = neck diameter,  $t$  = isothermal sintering time and  $B$  is a collection of material and geometric constants. The values of  $n$ ,  $m$ ,  $B$  depend on the mechanism of mass transport. The above empirical equation indicates that sintering is highly sensitive to the particle size, with a smaller particle size giving rise to more rapid sintering. The sintering data compiled by Robertson et al. confirms that a finer particle size is beneficial for titanium powder densification [16].

Therefore, it can be seen according to the discussion shown above that sintering temperature, particle size and particle size distribution are important variables to titanium sintering. The effects of these variables and levels will also be seen and discussed in other chapters in this thesis.

### **2.3 Manufacturing methods of titanium powders**

With the target to reduce the cost of titanium components manufactured by powder metallurgy, generally there are two approaches currently under development. One is to optimize sintering variables and levels and apply new sintering approaches for example microwave-assisted sintering [39] to lower the production cost. This will be discussed later. The other approach is to develop novel production methods such as FCC-Cambridge process [40] and ITP-Armstrong process [41] aiming to lower the cost of powder feedstocks. Different production methods have varied characteristics summarized in Table 2-2 [42].

Table 2-2: Characteristics of different feedstocks for titanium sintering

Process	Powder type	Advantages	Disadvantages / notes
Hunter	Elemental	Low cost; good compactability	High chloride impurities
HDH Kroll	Elemental	Lower cost; compactable	Mainstream process; impurity
TiH <sub>2</sub>	Elemental	Low cost; compactable	High potential for scale-up
HDH alloys	Pre-alloyed	Readily available	High cost
Gas atomized	Pre-alloyed	High purity	High cost; not suitable for cold compaction
(GA)			
Plasma rotating			
electrode process	Pre-alloyed	High purity	High cost; not suitable for cold compaction
(PREP)			
ITP-Armstrong	Elemental; Pre-alloyed	Potential low cost; compactable	Quality control and to be scale-up
FCC-Cambridge	Elemental; Pre-alloyed	Potential extremely low cost	Under development
CSIRO-TiRO	Elemental; Pre-alloyed	Potential low cost	The issue of high chloride impurity to be addressed

Among the production processes listed in Table 2-2, inexpensive HDH titanium powders produced from the mainstream Kroll process provide the most cost-affordable basis for current titanium sintering [7]. In the production of titanium sponge powders, the Kroll process is the mainstream process utilizing molten magnesium to reduce titanium tetrachloride [1], but is being modified by recently-developed processes [43-45], such as TiRO<sup>TM</sup> [46, 47] because of continuous production capability and low cost. Ti sponge fines are hydrogenated, ground and then dehydrogenated in the production of HDH powders. However, in this process chloride is an inevitable impurity in HDH-produced titanium powders originating from the sponge production process in either the Kroll [1, 48, 49] or modified processes [43, 44, 46].

## 2.4 Effect of impurities in titanium powders on sintering

The impurity issues always exist in and affect titanium sintering especially from titanium powders including interstitial impurities (C, H, O, N) and chloride impurities originating from the production process.

### 2.4.1 Carbon and nitrogen

Carbon and nitrogen are not generally found at high concentrations in titanium specimens [50] because it is not common to be introduced from either titanium powder production processes or consolidation of titanium powders. There are exceptions however such as metal injection moulding [51-53]. The presence of polymer-based binders during powder injection moulding increases the chances of carbon contamination during sintering [26, 54]. Therefore, the debinding of the polymer is always a crucial issue in titanium injection moulding [54]. The effect of these impurities on the mechanical properties of titanium specimens is pronounced even at low concentration [50]. This can be understood from the solubility of carbon and nitrogen in titanium shown in Table 2-3 [55].

*Table 2-3: Solubility of carbon and nitrogen in alpha titanium and beta titanium*

Phase	Temperature (°C)	Carbon, wt%	Nitrogen, wt%
Alpha Ti	— 882	0 – 0.4	0 – 8
Beta Ti	882 — 1670	0 – 0.2	0 – 1.9

It can be seen that the solubility of interstitials in titanium, especially carbon, is very low for both alpha (0 – 0.4 wt%) and beta (0 – 0.2 wt%) titanium. This probably means secondary phases would precipitate from Ti grains and form along the grain boundaries after reaching the saturation

point and therefore reduce mechanical properties hugely [56, 57]. According to the phase diagrams of Ti-C and Ti-N depicted in the ASM handbook [55], the solubility decreases with decreasing temperature. Due to the low solubility at room temperature, it is much easier to precipitate secondary phases during cooling from high temperature. This is supported by two latest findings [58, 59]. Although the carbon content takes only 0.032 wt%, which is well below the maximum limit of carbon content (0.1 wt%) specified by ASTM standard F2066-08 for wrought Ti-15Mo alloys, a noticeable presence of carbon-rich phase ( $Ti_2C$ ) was observed and formed along grain boundaries of Ti-15Mo alloys [58]. Similar finding was also noticed by another published work when dealing with sintering of Ti-Nb alloys [59]. Therefore, the ASTM standard for maximum carbon limit may need to be reassessed especially for  $\beta$ -Ti alloys consisting of Ti-Mo and Ti-Nb alloys [58].

For these interstitial contents such as nitrogen [60] below the maximum solid solubility limit, corresponding strengths can be increased because of solid solution strengthening [61, 62]. More works are presented on the microstructural evolution in chapter 5 and chapter 7.

#### 2.4.2 Hydrogen

In order to obtain pure titanium powders from titanium sponges, the HDH process is becoming popular because of its low cost as well as the convenience to break brittle titanium hydrides into fine particles [1]. However, possible problems associated with the high hydrogen content in titanium powders if the dehydrogenation process is not sufficient [19]. The high hydrogen content in Ti specimens would result in embrittlement [63] arising from the formation of hydride laths along grain boundaries as shown in Figure 2-2 [64].



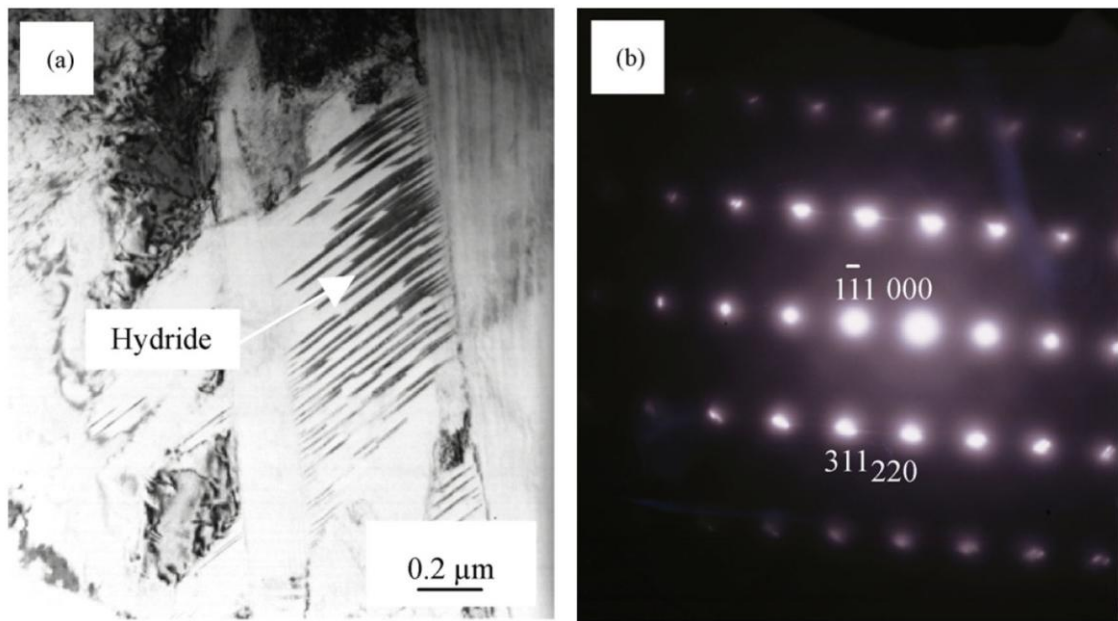


Figure 2-2: TEM images of Ti-6Al-4V alloy containing 1.2 wt% hydrogen: (a) hydride laths and (b) corresponding SAED pattern of hydride [64]

Figure 2-2 (a) shows that hydrides prefer to precipitate at grain boundaries in the bright field (BF) image, and the selected-area electron diffraction (SAED) pattern suggests the FCC structure belonging to  $\delta$  titanium hydride. It is interesting to note that hydrogen can also affect mechanical properties without forming a hydride phase by increasing dislocation motion along narrow slip bands and the literature reports that the detrimental effects of hydrogen are stronger in commercially pure titanium alloys with higher oxygen contents even at a low concentration of 70-80 ppm [63].

### 2.4.3 Oxygen

Oxygen is a common interstitial element for titanium [50] and both surface oxide layer and oxygen in solid solution contribute to the contamination in Ti powder metallurgy [61]. During the sintering process, the furnace atmosphere and racking materials sometimes introduces the oxygen

contamination [50]. Oxygen occupies octahedral sites of the alpha titanium lattice and increases the lattice parameters as well as the  $c/a$  ratio in the crystal when at low concentration, and the oxygen interacts with both the hydrostatic and shear stress fields dislocations, affecting both edge and screw dislocation motion [50, 61, 63]. Therefore, oxygen can increase the tensile strength and hardness but decrease the ductility [61]. This is in accordance with the results shown in Figure 2-3 in regard to the correlation between oxygen content and mechanical properties of sintered Ti and Ti-6Al-4V.

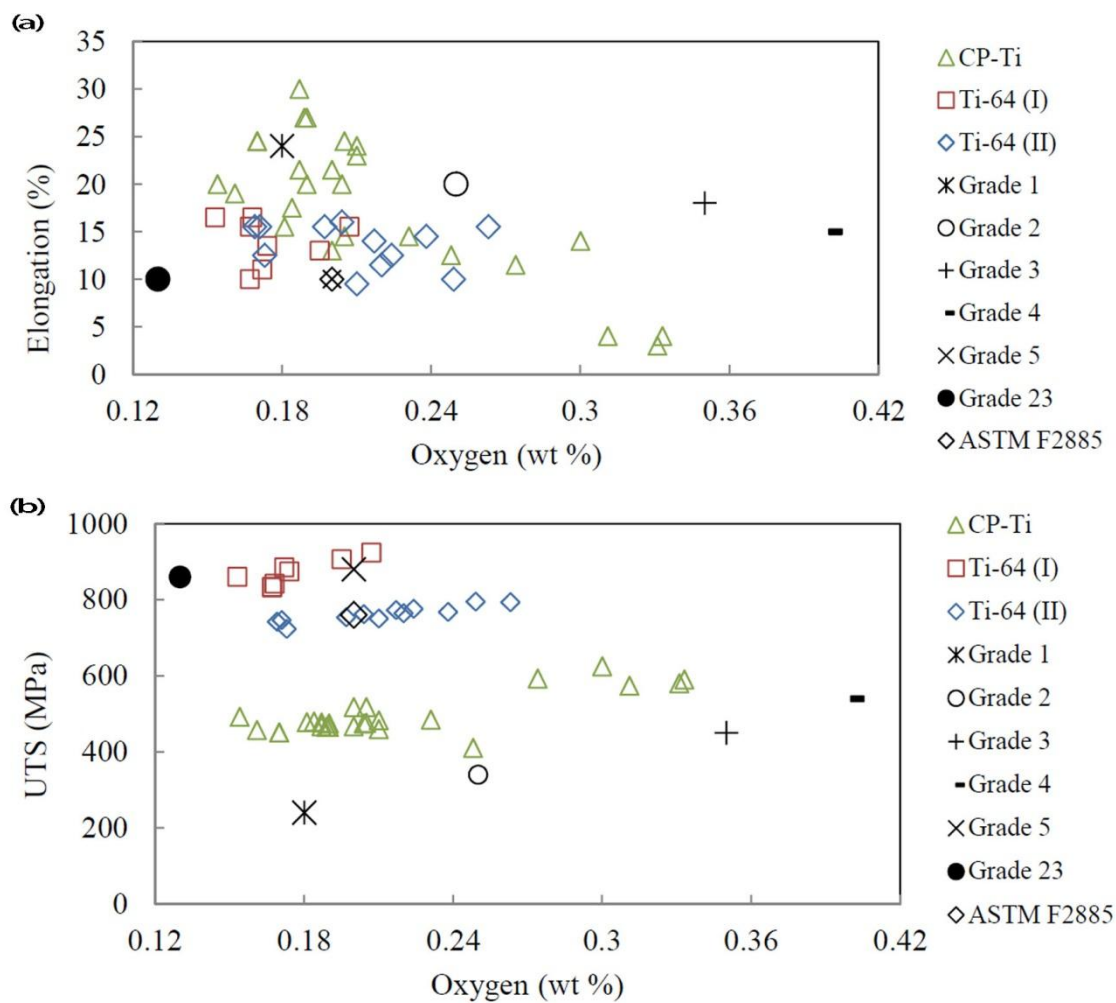


Figure 2-3: Effect of oxygen on the elongation (a) and ultimate tensile strength (b) of C.P. Ti and Ti-6Al-4V [61]

From Figure 2-3, it can be seen that in general the ductility decreases with increasing oxygen content for C.P. titanium and becomes more sensitive to oxygen when the content is above 0.24 wt%. The dependence of mechanical properties on oxygen content is also seen in different grades of ASTM Ti specimens (ASTM Grade 1 – 4, ASTM Grade 5 is for Ti-6Al-4V). Different grades of titanium are assigned in ASTM mainly according to their oxygen content. The oxygen content increases from 0.18 wt% (ASTM Grade 1) to 0.4 wt% (ASTM Grade 4). Correspondingly, the ductility decreases from around 25 % for Grade 1 to 15 % for Grade 4 while the ultimate tensile strength increases from 240 MPa for Grade 1 Ti to 552 MPa. This highlights the effect of oxygen content on titanium's mechanical properties. It is noted that in order to ensure tensile elongation  $\geq 10\%$ , the critical O content for Ti-6Al-4V is around 0.32 wt% as presented in Figure 2-3(a) and  $O \leq 0.3\%$  is required by ASTM B988-13 for as-sintered Ti-6Al-4V. The effect of oxygen interstitial content on titanium sintering is also reported in following chapters including chapter 5, chapter 7 and chapter 8.

#### 2.4.4 Chlorides

Chloride impurities in titanium powders originate from the powder production process. In titanium powder metallurgy, the most widely used and most economic titanium powders are either titanium sponge fines or HDH powders. Ti sponge fines are produced by either the Hunter or Kroll processes followed by crushing, while in the production of HDH powders, sponge fines are hydrogenated, ground and then dehydrogenated. Vacuum distillation is the main approach to remove the residual chloride from the sponges with the advantage over other methods of in situ removal in the reactor vessel [1, 65], and about 80% of this effort is to remove 1-2 wt%  $MgCl_2$  deep in the Ti sponges [5]. However, it is still impossible to remove the chloride completely.

The existence of chloride impurity adversely affects powder densification [17, 66], weldability [5], grain boundary embrittlement and microinclusions [17, 67], and significantly affects fatigue behaviour [2, 6, 68-71]. During the welding of P/M Ti products it has been shown that the residual chlorides from the titanium powders volatilized rapidly leading to a build-up on the welding electrode during the fusion process and resulting in inconsistent weld quality. In order to overcome this problem the Cl content was required to be  $<0.005$  wt% [5]. Fan et al. [67] investigated the effect of chloride in a Ti-6Al-4V alloy and a titanium metal matrix composite and reported some interesting and unusual results. They claimed that the presence of chloride does not appreciably affect the sintered density but does cause grain refinement. As a result the ductility of the sintered Ti-6Al-4V increases significantly with the content of chloride. They also identified three different forms of chlorides in the sintered samples: agglomerates of NaCl in pores seen in Figure 2-4, and isolated precipitates either in the matrix, or segregated to beta prior grain boundaries.

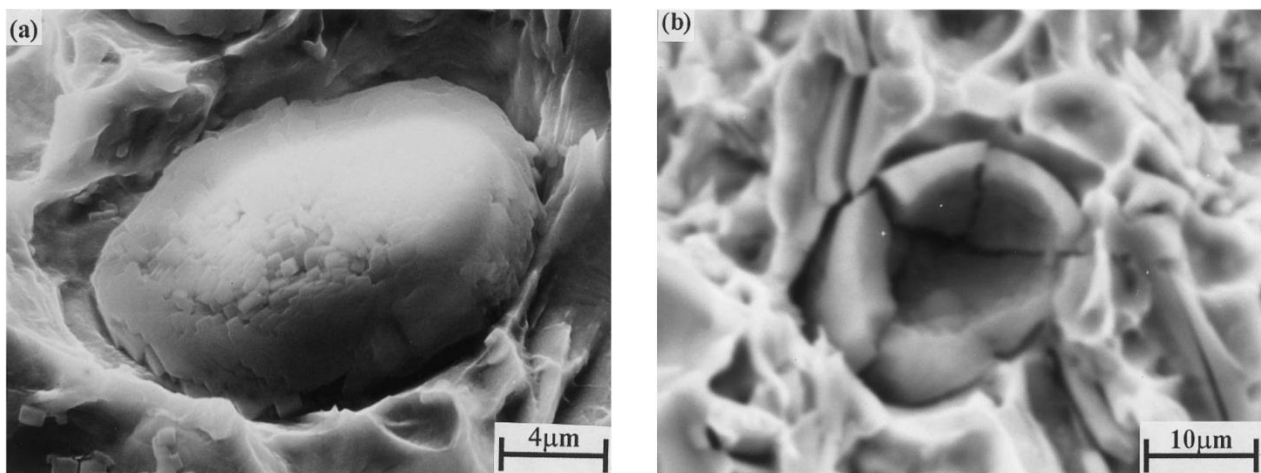


*Figure 2-4: SEM images showing shells consisting of fine NaCl particles in macropores: (a) Ti-6Al-4V; (b) Ti-6Al-4V-10%TiB. Both samples contained 800 ppm Cl and were sintered at 1300 C for 16 hours [67]*

Furthermore, the pores caused by dissociation of chloride cannot be closed by simple sintering; even hot isostatic pressing, forging and hot pressing cannot completely remove or close these pores, thus lowering the fatigue limit [2, 6, 68-71].

Since the residual chloride has a critical effect on titanium sintering utilising powders made from the Kroll and Hunter processes, there are currently two potential solutions to solve the issue. One is to avoid the chloride effect by fabricating extra-low chloride (ELC) titanium powders (the Cl contents  $< 0.002$  wt% are designated ELC [6]), such as  $< 0.001$  wt% Cl (Sumitomo, TILOP-150H and TILOP-45H) [5], however their cost can be extremely high. The other solution is to develop an effective chlorine scavenger such as the addition of  $0.05$  wt%  $Y_2O_3$  into the powder as studied by Low et al [65], however there are no reports in regard to the effect of  $Y_2O_3$  addition on mechanical properties. It is also reported that the application of  $CeSi_2$  and rare earth hydrides can effectively mitigate the chloride adverse effects and raise tensile ductility [72, 73].

It is noted that most studies described above deal with sodium chloride, which is an inherent impurity related to the Hunter process. In contrast, the effect of magnesium chloride – an impurity related to the Kroll process – on the sintering of titanium powders is not well understood. Furthermore, the Kroll process is the mainstream process for production of titanium sponge, and the Hunter process is no longer considered as a large-scale Ti production method because of reduced cost when using Mg rather than Na as the reducing agent [1, 5]. In this regard, a full understanding of how magnesium chlorides affects densification of titanium powder sintering is of significance from both scientific and technological points of view.

The deliquescence of  $MgCl_2$  makes the situation different from, and probably even worse, than the sodium chloride dissociation process. For example it is known that the ability of sea salt to absorb water is mainly due to the presence of  $MgCl_2$  impurity [74, 75]. The presence of this adsorbed water probably makes the dissociation process of  $MgCl_2$  more complex than that of

NaCl. Investigation of chloride impurities on HDH titanium powders is shown in chapter 4 and the effect of chloride impurities on titanium sintering will be reported in chapter 6.

## 2.5 Effect of compaction pressure and methods on sintering

Although uniaxial compaction offers cohesive structures near the final dimensions prior to sintering, possible density inhomogeneity would occur if sintering was carried out without isostatic pressing. Given pressed under uniaxial cold compaction, the density distribution is presented for different stages in Figure 2-5.

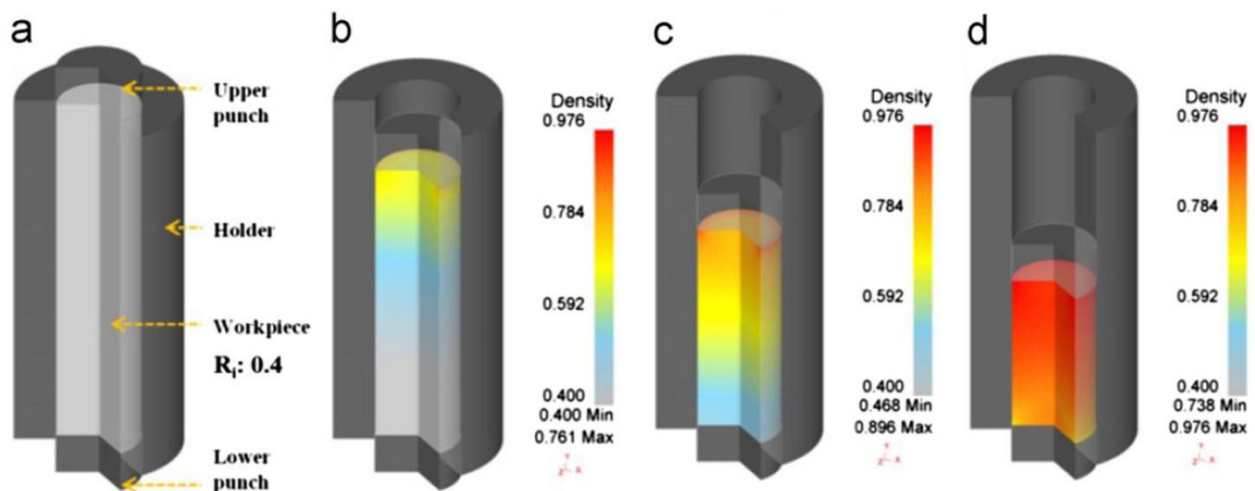


Figure 2-5: Finite elements (FE) simulation of relative density distribution during alumina compaction: (a) initial condition, and a total height reduction of (b) 20%, (c) 40% and (d) 56% [76]

In Figure 2-5, given that the lower punch and holder are rigid and fixed, it can clearly be seen that the density of the top of the green compact is much higher than the bottom part of the green body

because the force is applied through the upper punch. Such density homogeneity in green compacts would affect further the density distribution of sintered specimens and the mechanical properties of sintered specimens. For specific titanium powder compaction, there are several approaches to press titanium powders into a shape such as cold compaction, cold isostatic pressing, hot isostatic pressing and equal channel angular pressing.

### 2.5.1 Cold compaction

Cold compaction is the most economical of all compaction methods [77]. The dependence of sintered densities on cold compaction pressures can be seen in Figure 2-6 for titanium powders.

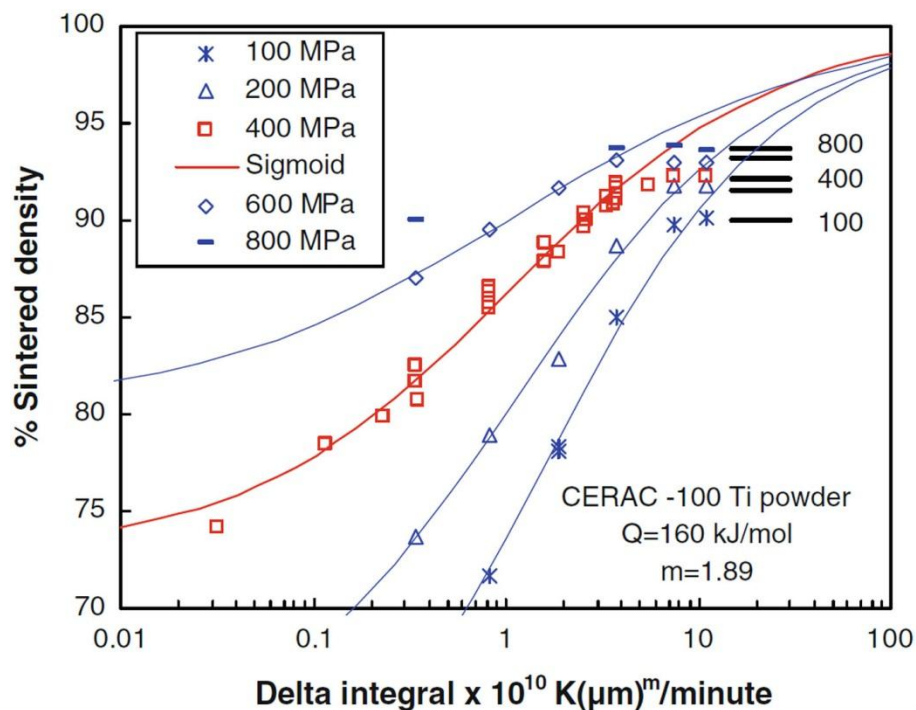


Figure 2-6: Sintered densities of -100 mesh titanium powder after cold compaction at 100 – 800 MPa. The full sigmoidal curve is a least-squares fit to the 400 MPa data except those at high values of the delta integral, where close to the fully dense [78]

When specimens are sintered under the same sintering temperature and holding time, it can be seen that high compaction load is favourable for obtaining larger sintered density for solid-state sintering. However, possible density inhomogeneity is still a problem arising from the inhomogeneous green density. This can be eliminated by using isostatic pressing such as cold isostatic pressing (CIP) and hot isostatic pressing (HIP). In the work described in the following chapters, all sintered specimens are pressed using uniaxial cold compaction coupled with cold isostatic pressing.

### 2.5.2 Isostatic pressing

Isostatic pressing can be divided into cold (CIP) and hot (HIP) depending on whether the process is operated at high temperature or not. This technique is promising due to the capability to realise uniform density distribution although the manufacturing cost is high, especially for HIP which incorporates the application of force at high temperature and controlling of sintering atmosphere [35, 36]. The additional benefit of HIP is the ability to largely remove residual pores in as-sintered specimens and therefore raising the corresponding mechanical property performance [22, 36, 38]. Typical HIP temperatures used for Ti-6Al-4V are in the range of 800-1000 °C with a holding time of 2-4 hours and a general applied pressure of around 100 MPa [37, 79]. The microstructural difference of titanium alloys can be seen in Figure 2-7 for press-and-sinter specimens and HIPed specimens after press-and-sinter.



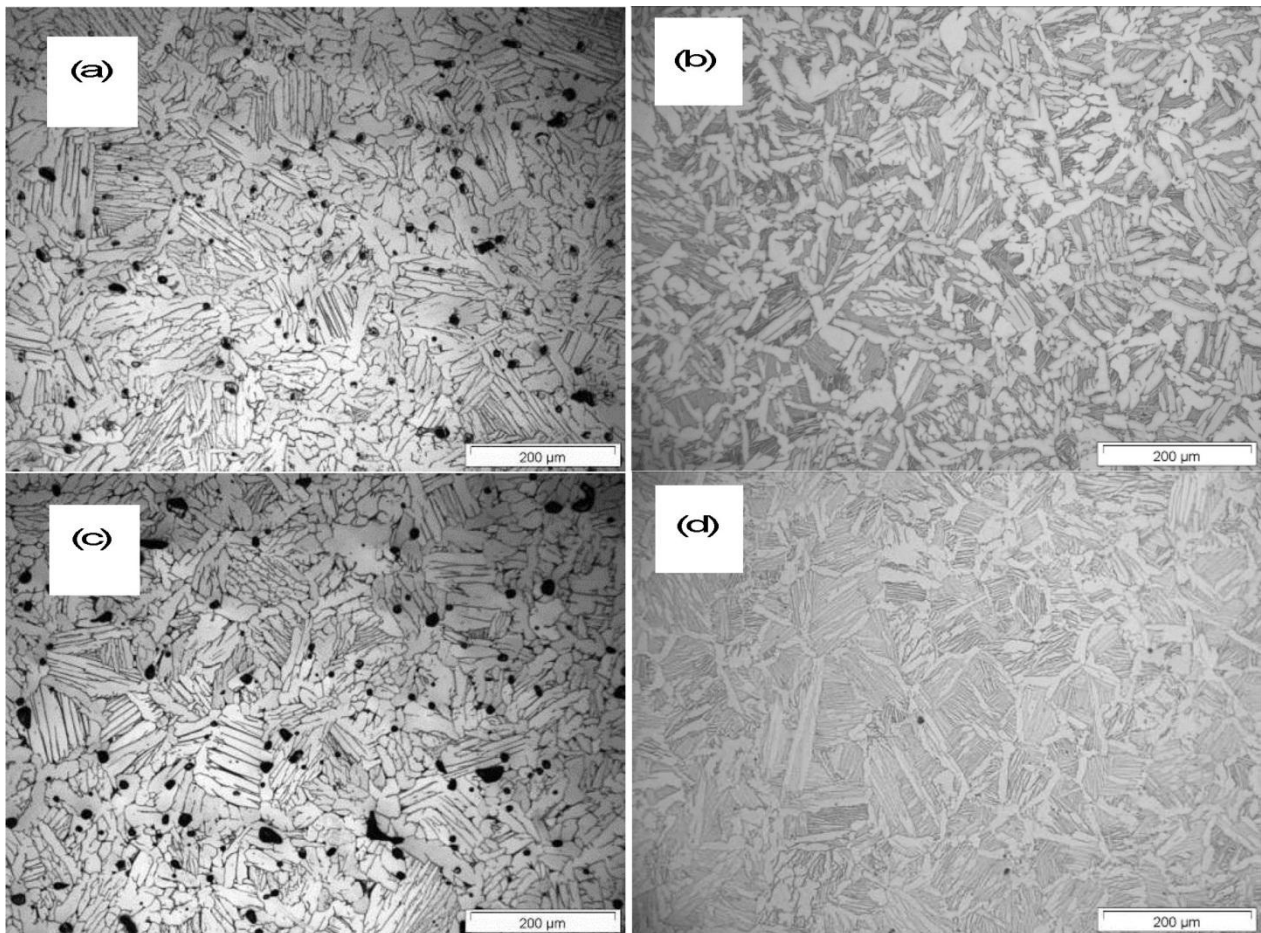


*Figure 2-7: Optical micrographs of (a) pre-alloyed Ti-6Al-4V after press-and-sinter, (b) further HIP at 1000 °C of Ti-6Al-4V, (c) pre-alloyed Ti-3Al-2.5V after press-and-sinter and (d) further HIP at 1000 °C of Ti-3Al-2.5V [79]*

After HIPing at 1000 °C, the apparent difference is the elimination of porosity in comparison with specimens with only press-and-sinter. However, although close to full density can be achieved by the application of HIP, the ductility was low mainly because of impurity introduction such as oxygen and nitrogen [79]. Therefore, strict control of the operating atmosphere is required. In addition to the difficulty to control the atmosphere in HIP, the cost is also very high compared with CIP. CIP employed in the experimental is because of the achievement of density homogeneity.

### 2.5.3 Equal channel angular pressing (ECAP)

Equal channel angular pressing (ECAP) incorporating a back pressure at temperatures typically  $\leq 400$  °C) has been applied to consolidate titanium and titanium alloy powders, with the capability of producing ultrafine-grained or nano-sized microstructures and providing the potential for unique mechanical and physical properties [27, 80, 81]. A typical ECAP unit is shown in Figure 2-8 (a) along with a schematic of the ECAP process setup (Figure 2-8 (b)).

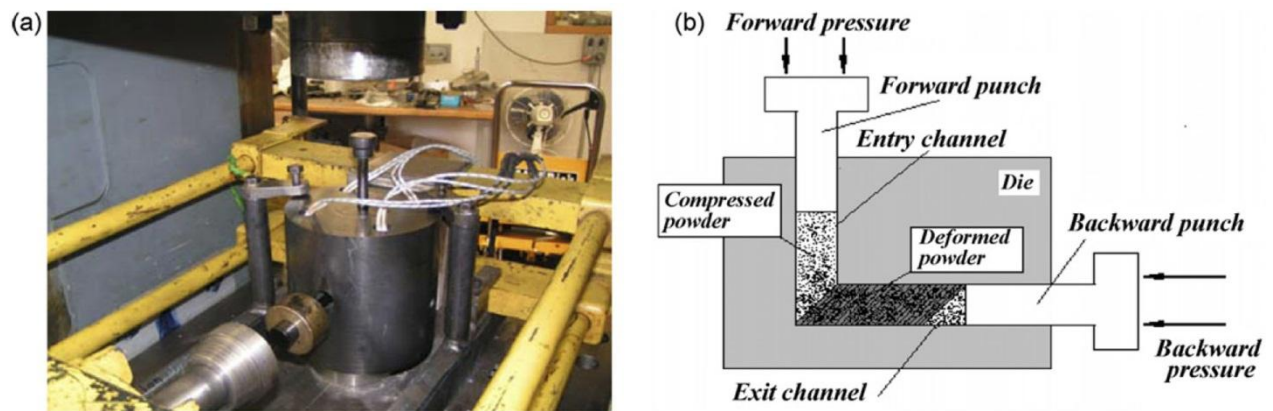
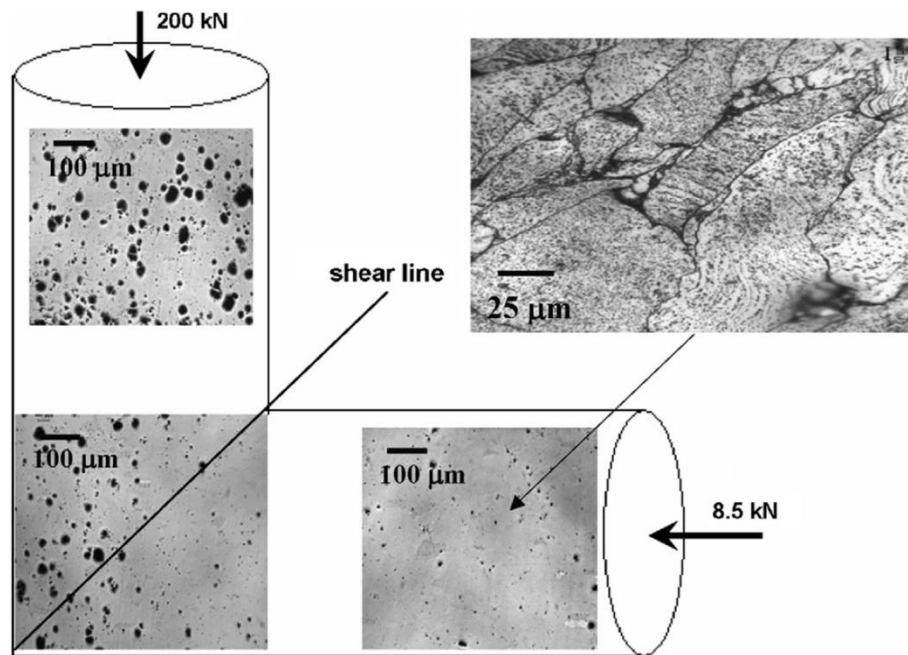


Figure 2-8: Equal channel angular pressing (ECAP) of powder: (a) unit for elevated-temperature ECAP with back pressure; (b) schematic of the process [81]

ECAP with back pressure was carried out in a specially-designed unit seen in Figure 2-8 (a) integrating a controllable temperature system, with an operation range of 20-450 °C, and the pressure is able to be adjusted in a horizontal hydraulic cylinder in the range of 20-500 MPa. There is a 90 degree angle between the vertical entry channel and the horizontal exit channel. The powder is poured into the entry channel and a back-pressure punch was positioned deep within the exit channel during pouring. The temperature and pressure can be regulated with specific

devices. Using this method, compacts with fine microstructures can be obtained with reduced porosity as seen in Figure 2-9.



*Figure 2-9: Influence of shear on pore size and distribution and realignment of large and fragmented particles after ECAP with 263 MPa of back pressure at room temperature [81]*

The amount and size of pores decreased in specimens after extrusion presented in Figure 2-9 in comparison with specimens without extrusion and specimens at the turning corner and strong deformation was revealed by the macrostructure observation in the specimens after extrusion. The compacts after ECAP are considered to be suitable for preforms of forging without performing sintering because of high density (~98 %) achieved [27, 81].

## 2.6 Development of low-cost titanium alloys

The additive elements into titanium alloys are classified as alpha-stabilizers, beta-stabilizers and neutral elements in accordance with their effect on the beta-transition temperature [3]. Among the  $\alpha$ -stabilizers, which can extend the  $\alpha$  phase field to a higher temperature and develop a two-phase  $\alpha+\beta$  field, aluminum is regarded as the most important and the widely-utilized element [3]. Ti-6Al-4V, a typical  $\alpha+\beta$  alloy including both aluminum as an  $\alpha$ -stabilizer and vanadium as a  $\beta$ -stabilizer, has been utilized widely because of good combined mechanical properties. Among PM sintering of Ti-6Al-4V, blended elemental sintering of Ti-6Al-4V is attracting more interests due to its lower cost compared with sintering of pre-alloyed Ti-6Al-4V powders [82, 83]. However, vanadium is an expensive element and toxic if considered for biomedical application [84], and it is necessary to develop novel alloys where the vanadium is replaced by other  $\beta$ -stabilizing elements. Iron is treated as one low-cost  $\beta$ -stabilizing element, and Ti-Fe is the only eutectoid system which does not undergo eutectoid transformation even at slow furnace cooling rates [7]. Silicon (Si) is another cheap element. It is reported that silicon is much lighter than titanium and the creep and oxidation properties of titanium alloys can be improved by the addition of silicon [7]. In this section, the effect of the addition of these two elements will be discussed on titanium sintering.

### 2.6.1 Addition of iron

Iron is abundant on Earth, and ranks the fourth in Earth's crust [85]. It is also the most widely-used low-cost metal in the formation of steel for engineering purposes. Current titanium powder metallurgy research has been largely devoted to cost reduction in titanium components by both developing cost-effective powder manufacturing and developing low-cost titanium alloys [49]. In the development of low-cost titanium alloys, Iron as a  $\beta$ -Ti stabilizer has also been considered for use in titanium alloys as a result of its low cost and exceptional alloy properties [86-90].

From a historical view, one important finding in regard to the use of iron in titanium alloys was a newly developed  $\beta$ -rich  $\alpha+\beta$  titanium alloy SP-700 (nominal component: Ti-4.5wt%Al-3wt%V-2wt%Mo-2wt%Fe) by NKK a Japanese company in 1989, which had better ductility and mechanical properties and longer fatigue life in comparison with Ti-6Al-4V [91-93]. Ti-xFe alloys also attracted high attention around 2000's with a research focus on the diffusion process and densification due to the low cost of iron [89, 94-96]. In a recently published paper, iron was considered to replace the expensive vanadium for casting Ti-6Al-4V alloys, more specifically, using arc melting method [87]. The mechanical properties are listed in Table 2-4 in contrast with Ti-6Al-4V.

*Table 2-4: Mechanical properties of low-cost titanium alloys in comparison with Ti-6Al-4V alloys[87]*

Mechanical properties	Ti-6Al-4V	Ti-3Al-2.5Fe	Ti-6.4Al-1.2Fe	Ti-5Al-2.5Fe
Reduction in Area (%)	37	38	40	34
UTS (MPa)	985	1115	1000	1040
Yield Strength (MPa)	950	1025	895	990
Elongation (%)	14	15	19	15

As shown in Table 2-4, the low-cost Ti-Al-Fe alloys have similar static mechanical properties as as-cast Ti-6Al-4V alloy. Since the cost of vanadium is expensive, the replacement is very meaningful to titanium industrial R&D. Although these results were from casting technology rather than powder metallurgy, the guiding principles may still be applicable. PM-Ti needs detailed research data base and science guidance to the usage of low-cost TiFe based titanium alloys.

From the viewpoint of microstructural design, a significant feature of iron additions is that Ti-Fe is the only eutectoid system compared with other low-cost titanium alloys such as Ti-Cu, Ti-Si etc. which does not actually undergo eutectoid transformation even under a slow cooling rate [7, 97]. This microstructural evolution can be schematically seen in Figure 2-10.

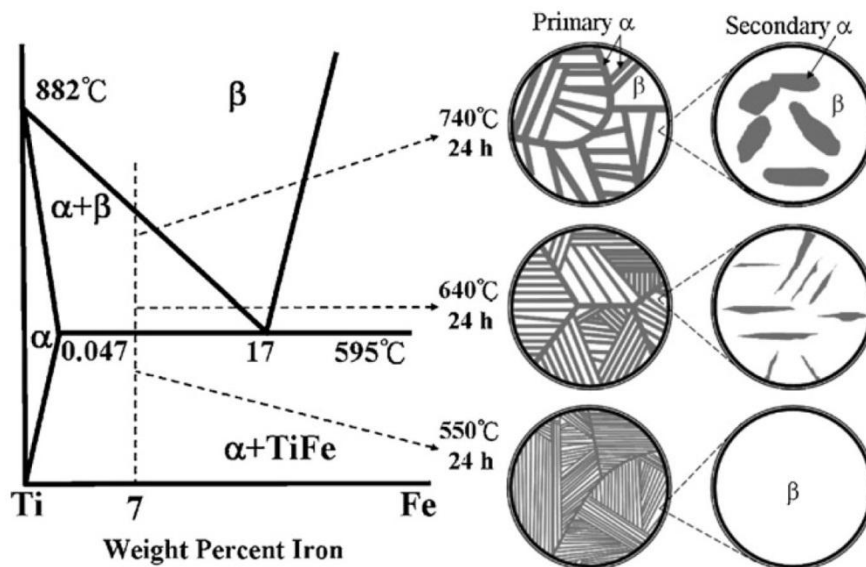


Figure 2-10: The schematic of the phases present in sintered Ti-7Fe under different cooling processes: furnace cooling (1150 °C - 740 °C/640 °C/550 °C) + holding for 24 hours (740 °C/640 °C/550 °C) + fan cooling (740 °C/640 °C/550 °C - 60 °C) [97]

From Figure 2-10, when specimens were held at 740 °C, coarse lamellae were present with a large amount of beta phase and small amount of secondary alpha phase. For samples held at lower temperatures at 640 °C and 550 °C, the amount of primary alpha phase increased while decreasing the amount of beta phase. It is notable that the brittle eutectoid phase (TiFe) was not present and avoided under all three cooling processes. The secondary alpha phase was studied by TEM shown in Figure 2-11.

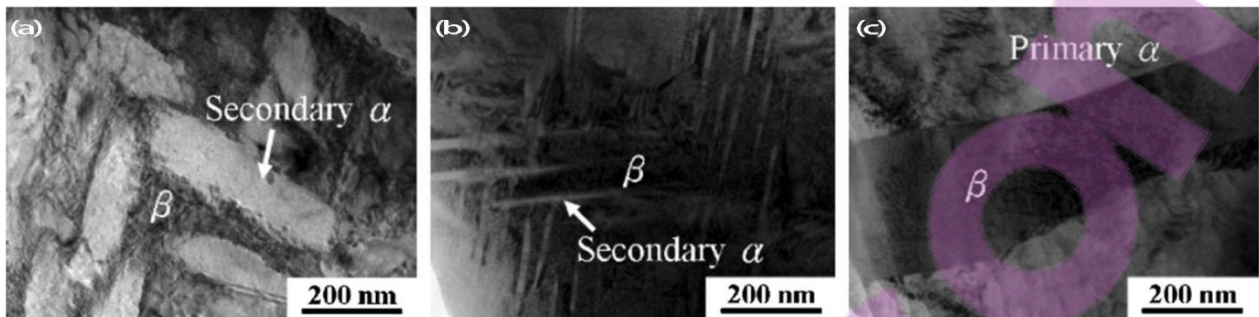
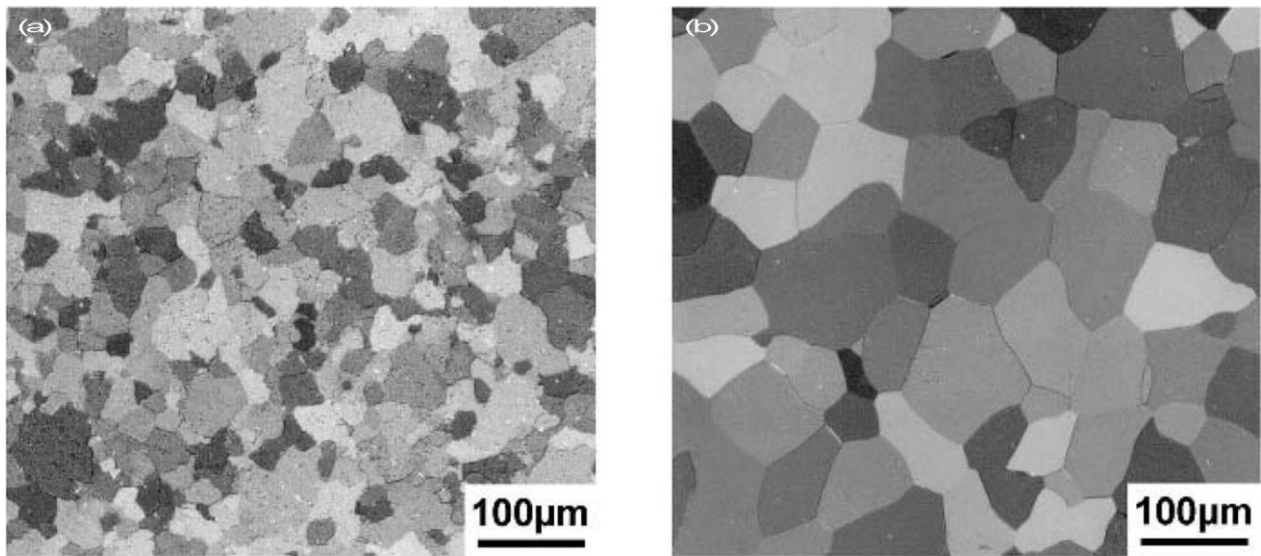


Figure 2-11: TEM images of sintered Ti-7Fe under different cooling processes: furnace cooling (1150 °C - 740 °C/640 °C/550 °C) + holding for 24 hours ( a: 740 °C, b: 640 °C, c: 550 °C) + fan cooling (740 °C/640 °C/550 °C – 60 °C) [97]

The size of the secondary alpha phase formed in beta phase decreased when changing the holding temperature from 740 °C to 640 °C and finally disappeared in specimens held at 550 °C in Figure 2-11. Again, there was no TiFe phase observed even at such high magnification. However, grain coarsening was found when just 1 wt% more iron was added into the alloying composition of Ti-10V-2Fe-3Al [98]. This is in agreement with the observation that pure titanium with 0.3 wt% Fe had a noticeable grain growth after an annealing heat treatment of 1 hour at 700 °C demonstrated in Figure 2-12 [1].



*Figure 2-12: Effect of iron content on the microstructure of C.P. Ti under polarized light with different iron content: (a) 0.15 wt% Fe; (b) 0.3 wt% Fe [1]*

The noticeable grain growth shown in Figure 2-12 would have detrimental effects on mechanical properties which is able to be understood from the well-known Hall-Petch relationship. Therefore, although the densification and tensile strength was enhanced by the addition of iron for low-cost Ti-xFe-0.5/1Si in the range from 3 wt% to 6 wt %, poor ductility was caused by grain growth with increasing the iron content [99].

### 2.6.2 Addition of silicon

Silicon with a density of  $2.33 \text{ g/cm}^3$  is about half the weight of titanium ( $4.506 \text{ g/cm}^3$ ) and is also inexpensive [100]. A small addition of silicon into titanium-based alloys can aid their creep resistance and oxidation [3, 7]. Silicon is also an effective sintering aid, for example, only 1 wt% Si increased the sintered density of Ti-3Ni from 91.8 % to 96.4 % sintered at the same temperature of  $1300 \text{ }^\circ\text{C}$  [100]. However, although densification can be improved dramatically, mechanical properties of titanium-based alloys are sensitive to the amount of silicon addition. It



has been reported that a small addition of silicon ( $\leq 1$  wt%) has the capability to improve the as-sintered tensile properties of Ti-3Fe alloy due to fine titanium silicide ( $\text{Ti}_5\text{Si}_3$ ) dispersed in both the alpha and beta phases [99]. The precipitates in alpha titanium are shown in Figure 2-13.

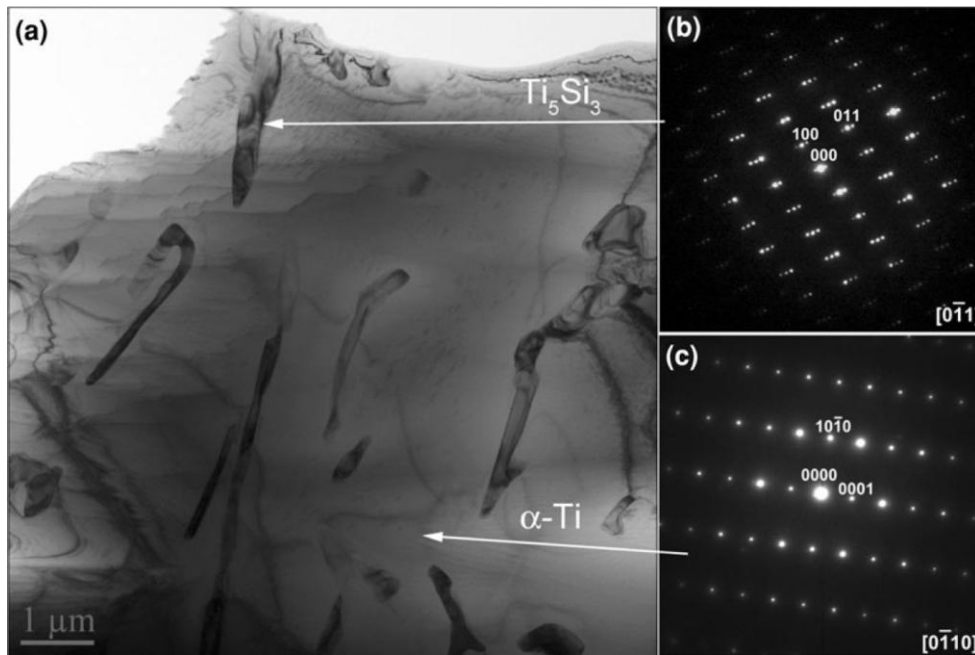


Figure 2-13: TEM analysis of the fine precipitates in the alpha phase: (a) a bright-field image of sintered Ti-3Fe-xSi ( $x \leq 1$ ), (b) and (c) SAED patterns taken from the marked areas in (a) [99]

From Figure 2-13, it can be understood that the improved mechanical properties arise from the precipitation hardening of fine eutectoid products  $\text{Ti}_5\text{Si}_3$ . The improvement of mechanical properties also appears in the alloying system of Ti-Ni with the addition of silicon seen in Figure 2-14.

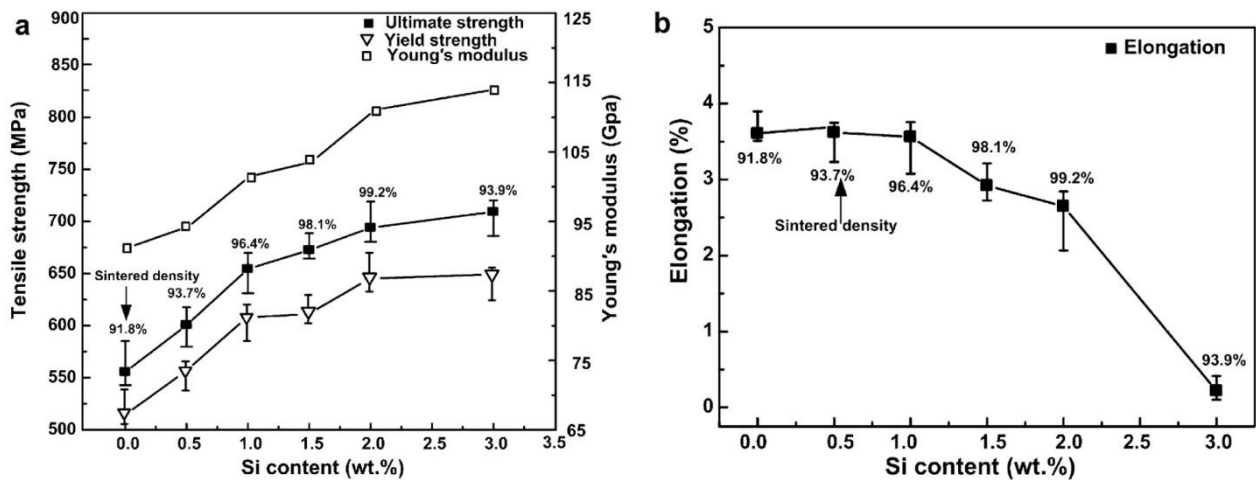


Figure 2-14: Tensile strengths and elongation of Ti-3Ni-xSi sintered at 1300 °C with a holding time of 120 min in vacuum [100]

It can be seen that sintered densities increase with the amount of Si addition from 91.8 % (with 0 wt% Si) to 99.2 % (with 2 wt% Si), and drop to 93.9 % when increasing the Si addition to 3 wt%. Ultimate tensile strength, yield strength and Young's modulus increase with the addition of silicon for Ti-3Ni-xSi. However, the ductility keeps similar at around 3.6 % when the addition content is  $\leq 1$  wt%, then drops dramatically to almost zero for specimens with 3 wt% Si addition. The reason is considered as grain boundary embattlement shown in Figure 2-15.

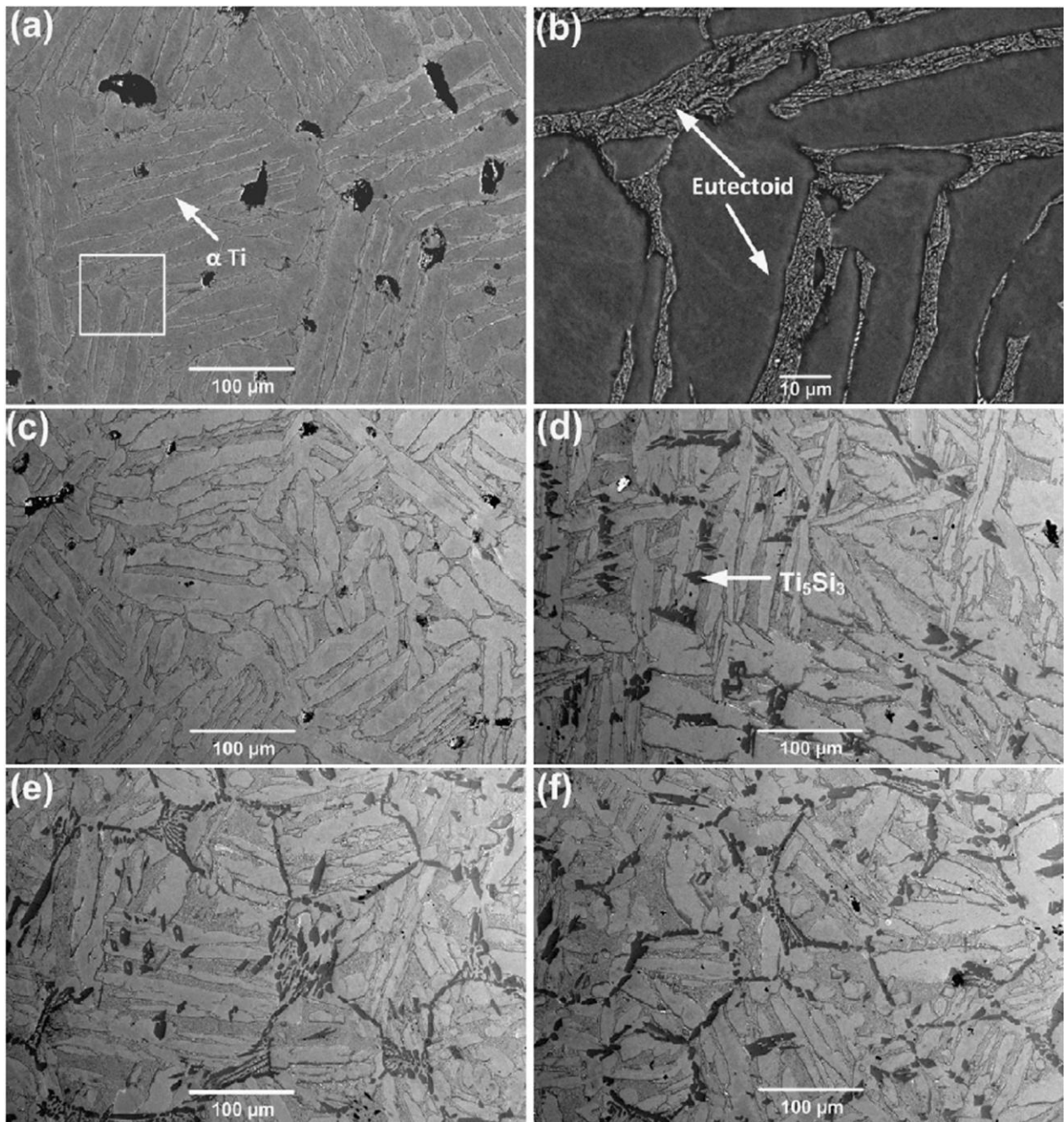


Figure 2-15: Optical microstructures of Ti-3Ni-xSi sintered at 1300 °C with a holding time of 120 min in vacuum (a) 0 wt% Si, (b) magnification of the marked area in (a), (c) 1 wt% Si, (d) 1.5 wt% Si, (e) 2 wt% Si, and (f) 3 wt% Si [100]

When increasing the addition content  $\geq 1.5$  wt%,  $Ti_5Si_3$  was formed by eutectoid reaction and observed along grain boundaries as seen in Figure 2-15 (d, e and f). This would lead to grain

boundary embrittlement and predominantly intergranular fracture [100] and thereby decreasing the ductility. Therefore, although silicon is beneficial to sintering densification, care is required in terms of the amount of additions into titanium-based alloying systems when the target is to pursue high tensile properties.

## **2.7 Review of novel sintering methods**

Since cost reduction is always the primary driving force for titanium R&D, there are several ways Ti researchers and engineers are making efforts on mainly including development of low-cost low-impurity titanium powders [5] and novel sintering methods. There are many advantages to applying novel sintering approaches. Microwave-assisted sintering of titanium has capability to reduce sintering cycle times resulting from fast heating rates of 30-40 °C min<sup>-1</sup> compared with conventional rates of around 5-10 °C min<sup>-1</sup> [101-103]. Additive manufacturing technology, also known as 3-D printing, has the potential to realise low-cost manufacturing in comparison with traditional pathways [104]. Spark plasma sintering of titanium is promising mainly because of its ultra-fast sintering rate and low sintering temperature thereby depressing detrimental grain coarsening [105, 106].

### **2.7.1 Microwave-assisted sintering**

Microwave sintering, as a novel sintering method, provides a potential for rapid heating rates and thereafter increasing productivity and energy savings during sintering [102, 107-110]. Some metal powders such as iron are already known to be able to couple with microwaves and can be heated up as quickly as ~100 °C min<sup>-1</sup> under varied sintering atmospheres [109, 111, 112]. It is also found that microwave sintering can offer larger shrinkage than conventional sintering [111]. Zhou et al. studied the heating rate on microwave sintering of W-Ni-Fe alloys and indicated that there existed an optimum heating rate when pursuing the good combination of microstructure and

mechanical properties [112]. The research work on titanium is quite limited using microwave sintering because pure microwave radiation seems to be ineffective with heating titanium powders [113] possibly resulted from the instinct paramagnetic property of titanium, a property not coupled with microwave heating [39, 102]. The use of microwave susceptors such as SiC can significantly improve the sinterability [108, 114]. An interesting phenomenon was observed for microwave-assisted sintering of c.p. titanium using titanium hydride powders to highlight the difference between microwave sintering and conventional sintering seen in Figure 2-16.

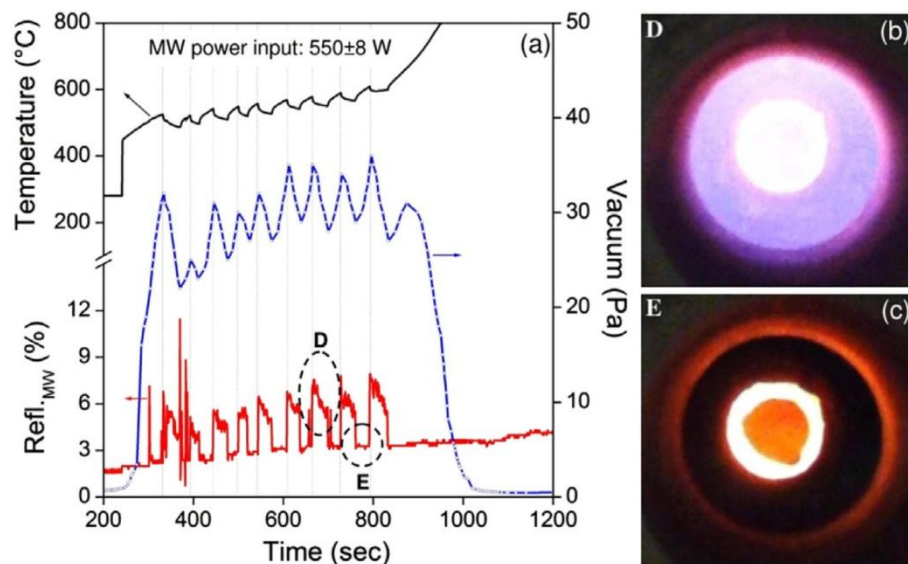


Figure 2-16: Variations in temperature, vacuum and microwave powder reflection ratio during temperature fluctuations. (b) and (c) are images of specimens when electric arcs are discharging (D) and extinguishing (E) marked in (a). TiH<sub>2</sub> powders were applied here.[103]

Apparent discharging and extinguishing of electric arcs shown in Figure 2-16 (b and c) were observed for sintering of titanium hydride in the microwave furnace. This is because of the formation of a microwave-induced hydrogen plasma [103]. The plasma can reflect microwaves as long as the MW frequency is less than the plasma frequency and therefore the plasma

temperature would be less than the sample temperature [115, 116]. This is in accordance with the observation shown in Figure 2-16 (a). Because of the absence of microwave, the plasma is typically not seen in conventional sintering of titanium. Titanium specimens sintered by microwave also have the capability to give desired mechanical properties seen in Figure 2-17.

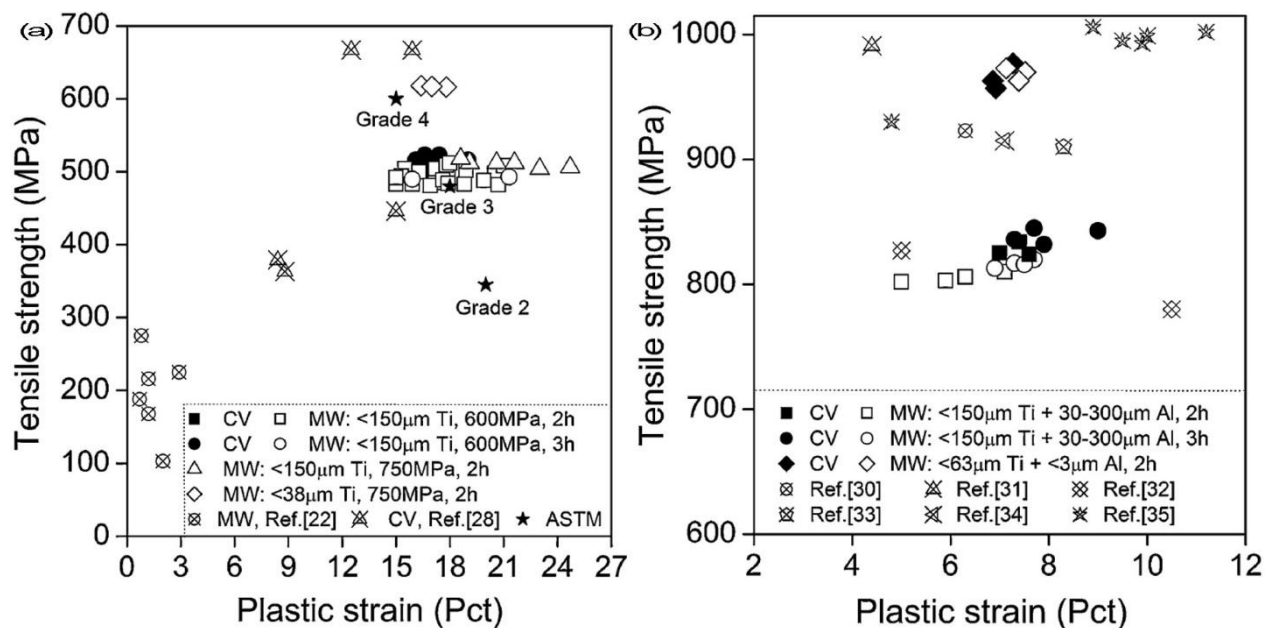
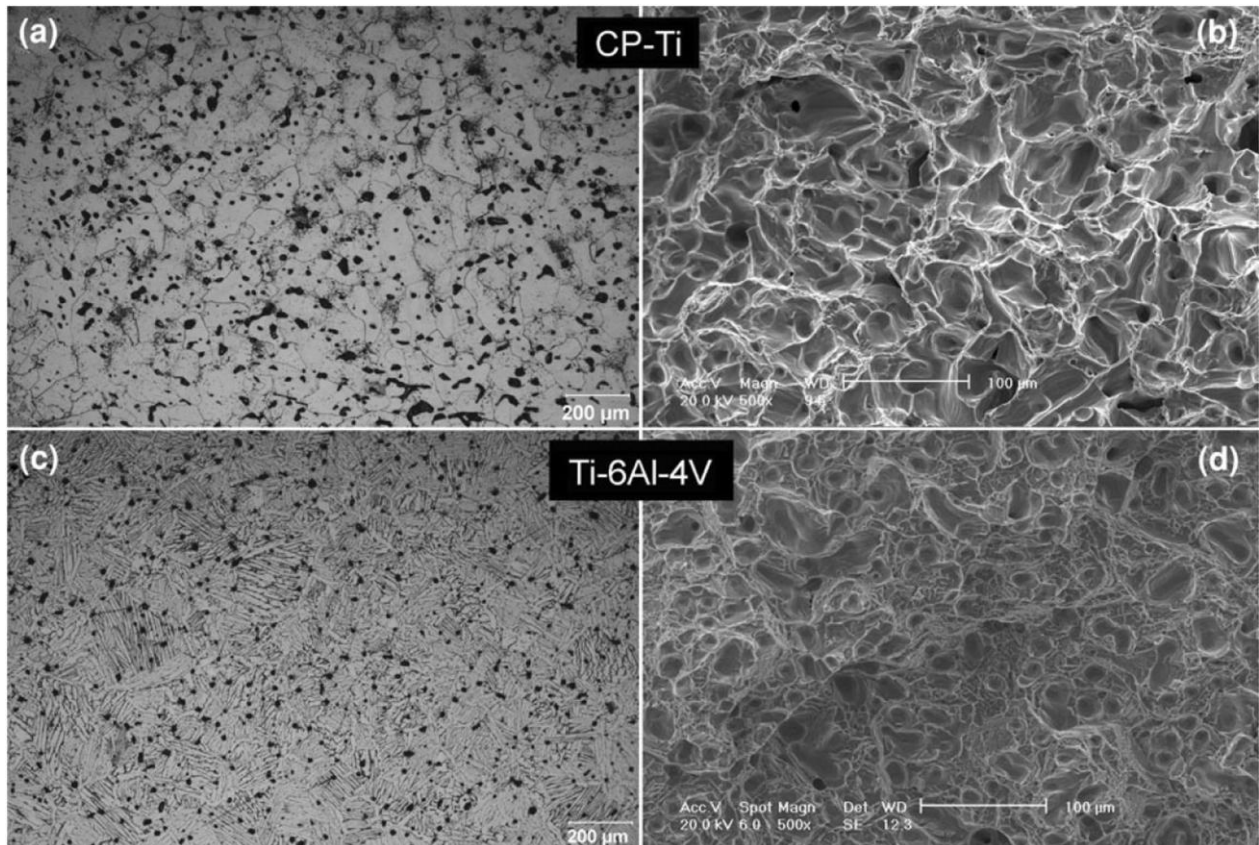


Figure 2-17: Tensile mechanical properties of specimens sintered by microwave-assisted (MW) and conventionally vacuum (CV) under different conditions. (a) CP-Ti; (b) Ti-6Al-4V, compacted from blends of elemental Ti and Al powders and Al-V master alloy powder (particle size <150  $\mu$ m) at 600 MPa [39]

There are no obvious difference observed in Figure 2-17 in regard to tensile mechanical properties between conventional vacuum sintering and microwave-assisted sintering of C.P. titanium and Ti-6Al-4V. All microwave-sintered titanium specimens exhibit higher tensile strengths than ASTM grade 2 Ti and give similar or larger elongation than ASTM grade 4 Ti

presented in Figure 2-17 (a). Typical fractographs are illustrated in Figure 2-18 for C.P. titanium and Ti-6Al-4V,



*Figure 2-18: Optical micrographs and corresponding fractographs of microwave-sintered C.P. titanium ( $< 150 \mu\text{m}$ ) and Ti-6Al-4V ( $< 63 \mu\text{m}$  Ti,  $75\text{-}150 \mu\text{m}$  Al-V,  $3 \mu\text{m}$  Al). Specimens were pressed at 600 MPa and sintered at 1300 C with a soaking of 2 hours [39]*

After sintering at 1300 °C with a holding time of 2 hours, ductile fracture surfaces with dimples were observed in both C.P. titanium and Ti-6Al-4V. This is compatible with high tensile ductility presented in Figure 2-17. In addition, most pores shown in Figure 2-18 (a and c) are spherical

which indicate the sintering has entered into the final stage and it would be difficult to remove pores just via sintering.

### 2.7.2 Additive manufacturing (3D printing)

Additive manufacturing is also known as direct digital manufacturing or 3D-printing. 3D-printed technology incorporating laser sintering is now offering opportunities to cut the cost dramatically and can realize complicated shapes designed by CAD [104]. The process can be divided into laser-based and electron beam-based sintering depending on the type of powder source. One schematic of a selective laser sintering process can be seen in Figure 2-19.

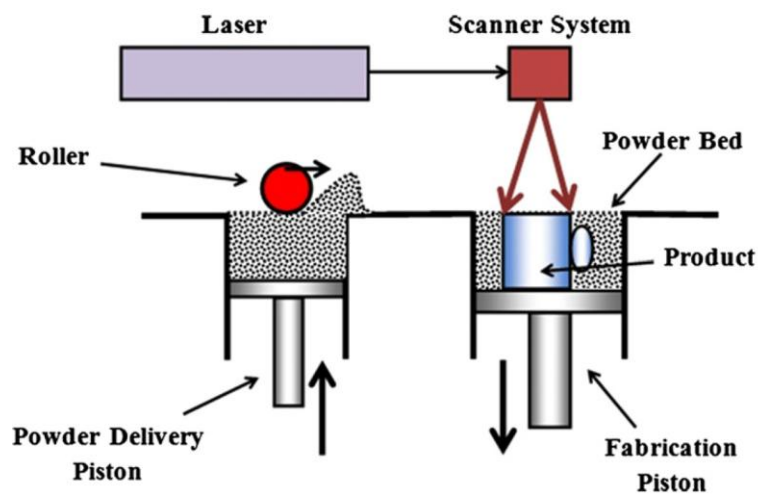


Figure 2-19: Illustration of the selective laser sintering process [117]

In Figure 2-19, powder layers generally in 0.1 mm thickness are generated by a rotating roller and the entire process is carried out in a closed chamber filled with inert gas to minimize oxidation [117]. A focused carbon dioxide laser is employed on those powder layers to fuse and form



sintered parts layer by layer [117]. Industries such as automobile (titanium car), biomedical area (titanium implants) and entertainment (sports equipment) can benefit heavily from the progress of 3D-printed titanium technology. Since traditional Ti manufacturing produces 80% scrap or higher, 3D printing of titanium has the ability to reduce the material wastage by 90% and offer access to the availability of complicated shapes [104, 118]. This technology can be divided into two parts: model design and laser sintering or other sintering technologies. The desired shape is designed by CAD assisted and final consolidation work is conducted by laser sintering using fine titanium powders at a certain temperature. Powders are added layer by layer and solidified in the model shape designed previously. In order to pursue desired Ti products, the optimization of laser sintering variables and levels is required to be investigated. In addition, the pick-up of interstitial elements, such as oxygen and carbon, during laser sintering reduces the mechanical properties and also makes 3D-printed titanium products still far from available commercialisation.

### 2.7.3 Spark plasma sintering

Both external pressure and electric field are applied simultaneously to enhance the densification of titanium powders in spark plasma sintering (SPS). Low sintering temperature and short sintering cycle time are attractive to spark plasma sintering of titanium [105, 106]. A typical schematic of SPS experimental setup is shown in Figure 2-20.

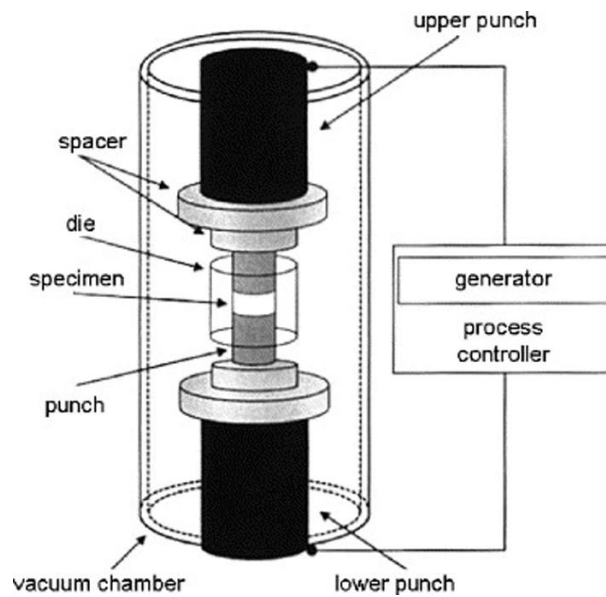


Figure 2-20: Schematic of spark plasma discharge setup [119]

SPS can be carried out at low temperatures, such as 800 °C, compared with traditional sintering temperature under vacuum. The heating rate is also typically fast for example 100 °C/min. High compaction pressure was also applied during sintering to accelerate densification.

## 2.8 Problems and challenges in titanium sintering

According to the above literature review, it can be seen that titanium and titanium alloy powders are already available to be consolidated using various sintering technologies and corresponding acceptable mechanical properties have been obtained. However, there are still problems and challenges to be addressed for titanium sintering.

First, as to the raw materials for titanium sintering – titanium powders, although Kroll processed HDH titanium powders are low-cost and widely utilized, there is little work investigating the inherent magnesium chloride impurities arising from Kroll production process since such

chlorides are different from sodium chloride originating from Hunter process which have been studied intensively in the past literature.

Several novel titanium sintering approaches have been reported in the literature including microwave-assisted sintering, SPS and additive manufacturing. It is interesting to develop more novel sintering technologies such as sintering a graphite furnace since carbon potential may react with oxygen gas and lower or eliminate the oxygen content in the furnace atmosphere. However, there is no such work reported previously working on the effect of the carbon potential in the furnace on microstructural evolution and mechanical properties. In addition, the effect of magnesium chlorides described above and their effects on titanium sintering is also necessary to be assessed in such furnace.

As mentioned above, many novel titanium powder manufacturing methods have been developed. One recently developed method has been reported to produce ultrafine titanium powders. However, sintering work using this kind of powder is still absent. In addition, as described in Section 2.6, it is necessary to develop low-cost titanium alloys. Such understanding of the development of low-cost titanium alloys is also studied in this work using ultrafine titanium powders and low-cost alloying element such as iron.

### 3. EXPERIMENTAL METHODS

This chapter provides a general description of the experimental methodology employed in this project, and includes details on the experimental materials, sintering process and characterization methods. More detailed and specific experimental design can be seen in each individual chapter.

#### 3.1 Experimental materials

PM Ti can use two different kinds of feedstock materials: one is pre-alloyed powder sintering (PA) and the other is blended elemental powder sintering (BE) [33]. Taking sintering of Ti-6Al-4V for example, pre-alloyed powder sintering means sintering with pre-alloyed Ti-6Al-4V powders which are obtained from high-cost production methods such as PREP or GA methods described in Table 2-2. BE sintering of Ti-6Al-4V indicates sintering is carried out using elemental titanium powders blended with Al-V master powders or elemental aluminium and vanadium powders. BE approach is more economic than pre-alloyed method because BE utilizes most cost-effective powder sources.

The experimental materials utilised most in this project include commercially pure titanium powders (-200mesh, <75  $\mu\text{m}$ ) and pre-alloyed Ti-6Al-4V powders (-200mesh, <75  $\mu\text{m}$ ), supplied by Xi'an Lilin Ltd, China. According to the information provided by the supplier, the titanium powders were produced from Kroll sponge titanium fines, and the dehydrogenation process was conducted in a vacuum furnace at 630 °C with a soaking time of 96 hours.

Recently a novel ultrafine HDH Ti powder production method was developed with a median particle size < 10  $\mu\text{m}$  [120]. However, there are no available sintering trials using such powder.

With such small particle size, it is almost impossible to avoid interstitial element contamination, particularly the oxygen, due to the high chemical activity of Ti and large surface to volume ratio. Therefore, it makes it interesting to investigate the interaction effect of ultrafine particle size and high impurity content on sintering. The starting ultrafine titanium powder (O: 0.82 wt%, C: 0.058 wt%, H: 0.414 wt%, N: 0.575 wt%) for these experiments was produced from Ti sponge fines which were hydrogenated at 700 °C with a holding time of 2 hours followed by 5-hour ball milling [120]. In this way, ultrafine titanium hydride was produced with a median particle size < 3 μm. An inhibitor (NaCl) is introduced for the coating of titanium hydride powder, which is further dehydrogenated at 630 °C for 2 hours. The ultrafine HDH titanium powders are water-leached by deionized water in order to remove the inhibitor. More detailed description of the ultrafine Ti production process can be seen in the literature [120, 121]. Meanwhile, it has to be noted that the possible high densification may not just come from fine particle size but also arise from the effects of interstitial elements such as oxygen being a fast diffuser in Ti [122].

A commercially available 60Al-40V master alloy powder (-120mesh; O: 0.18 wt%, C: 0.029 wt%, H: 0.0005 wt%, N: 0.16 wt%) and iron powder (-300mesh; O: 0.67 wt%, C: 0.041 wt%, H: 0.0022 wt%, N: 0.262 wt%) supplied by Beijing Youxinglian Nonferrous Metals Co. Ltd, China.

### **3.2 Compaction and sintering**

Powders were compacted into shapes with uniaxial hydraulic press at pressures ranging from 300 to 500 MPa followed by cold isostatic pressing (CIP) at either 200 MPa or 600 MPa. The pressed compacts were sintered in a high-temperature graphite furnace. The illustration is presented in Figure 3-1 for titanium sintering.

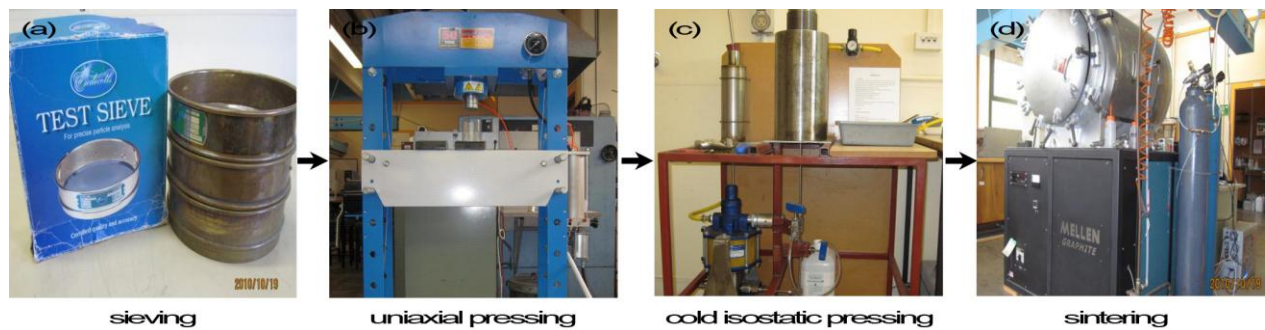


Figure 3-1: Pressureless/pressure-assisted sintering experiment process flow chart (CIP is optional)

The graphite furnace employed in this work (Mellen, USA) has three sets of graphite heating elements and uses graphite liners for insulation. The hot zone is 20 cm × 20 cm × 20 cm. The compacts were placed on an alumina/boron nitride tray at the central of the hot zone. A schematic diagram of the furnace can be seen in Figure 3-2.

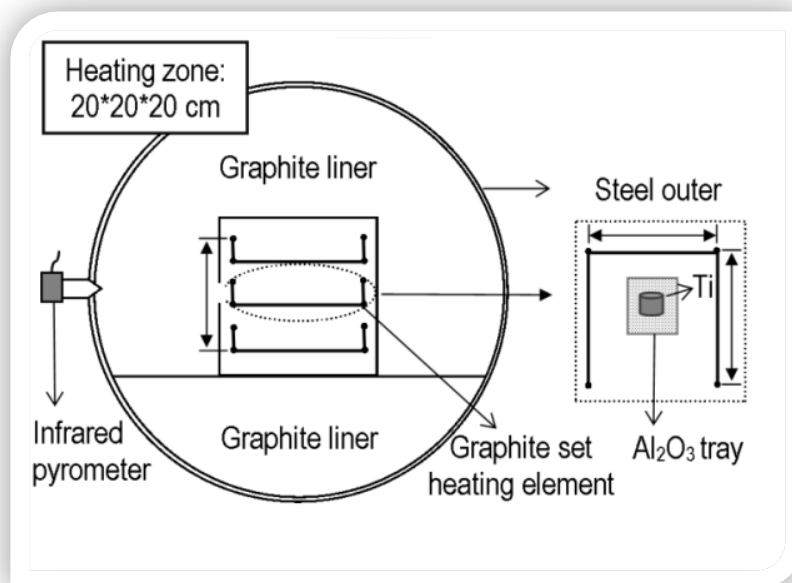


Figure 3-2: Schematic diagram of high-temperature graphite furnace

Typically compacts were pressed at a compaction pressure of 200-500 MPa followed by sintering from 1100 °C to 1400 °C under atmosphere or vacuum. A typical sintering schedule is presented in Figure 3-3.

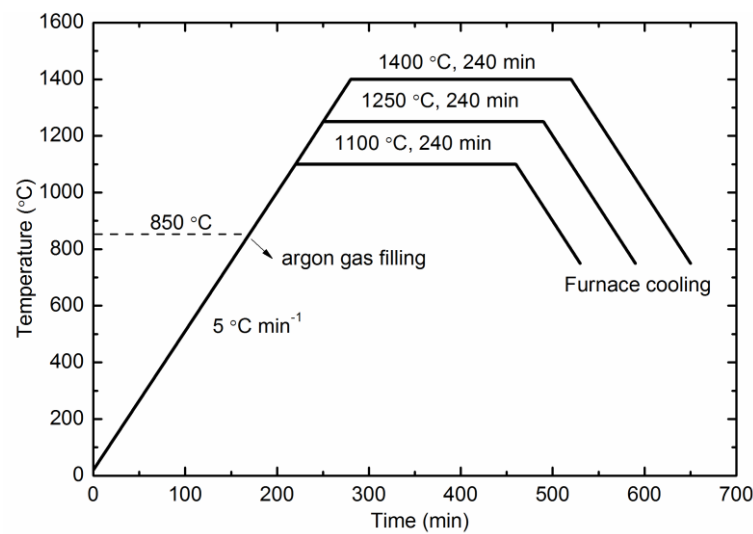


Figure 3-3: Illustration of heating curve for titanium sintering

After the specimens were loaded, the furnace was evacuated to a vacuum level of 0.1-0.01 Pa and heated with a heating rate of 5 °C min<sup>-1</sup>. When the temperature reached 850 °C, argon gas was back filled to the furnace and a pressure of 1.1 atm ( $1.1143 \times 10^5$  Pa) was maintained until the end of atmosphere sintering. A positive net furnace pressure is designed to avoid the inwards air flow from the ambient. For vacuum sintering in the graphite furnace, the low vacuum level was maintained until the end of sintering.

### 3.3 Density measurement and phase determination

The sintered density was measured according to Archimedes method described in ASTM B962-08 standard. In brief, samples were evacuated in water and then the mass was measured three times; once with the sample submerged in water, once out of water and once dried. The density was calculated according to following formula:

$$\rho_s = m_A \rho_w / (m_B - m_C) \quad (3-1)$$

where  $\rho_s$  is the sintered density ( $\text{g}\cdot\text{cm}^{-3}$ ),  $m_A$  is the mass of dried sintered part in air (g),  $\rho_w$  is the density of deionized water ( $\text{g}\cdot\text{cm}^{-3}$ ),  $m_B$  is the mass of sintered part out of water after submerging (g) and  $m_C$  is the mass of sintered part submerged in water (g).

X-ray diffraction (XRD) analysis to determine phase constituents of as-received powders, sintered surfaces and polished cross-sections was carried out on a D2 PHASER (Bruker) equipped with Cu X-ray source. X-ray patterns were collected over a scan range from  $2\theta$   $20^\circ$  -  $80^\circ$  with a step size of  $0.02^\circ$ . The specific phase was analysed using JCPDS cards with licenced software.

### 3.4 Metallography preparation

In order to reveal the cross-sectional microstructures, specimens were sectioned longitudinally through the vertical central axis followed by mounting in a cold setting epoxy resin and ground with silicon carbide (SiC) papers progressively from 220, to 2000 grit. The samples were polished with  $6\ \mu\text{m}$ ,  $3\ \mu\text{m}$  and  $1\ \mu\text{m}$  diamond solutions. Fine polishing was conducted with OP-S,



a colloidal silica suspension with 10% hydrogen peroxide ( $\text{H}_2\text{O}_2$ ), where the size of the colloidal silica is ~40 nm. Some specimens were further etched with Kroll's reagent (2 ml HF, 4ml  $\text{HNO}_3$ , 100 ml  $\text{H}_2\text{O}$ ). Cross sections of sintered samples were examined with optical microscopy (OM, Olympus BX60M). The average grain size was measured and calculated according to the linear intercept method described in the ASTM standard E112-12.

### **3.5 Microstructural observation and semi-quantitative compositional analysis**

The microstructural morphology observations including as-sintered surface, cross-sections and fracture surfaces were conducted on an environmental scanning electron microscope (ESEM) (Quanta 200F, FEI) using both back-scattered and secondary electron modes. In general, the beam voltage is in the range of 10-20 kV and the working distance is between 10mm and 11 mm. Semi-quantitative compositional analysis was carried out by energy dispersive spectrometry (EDS). Three types of scanning mode were adopted: spot scanning, line scanning and mapping. Both elemental X-ray mapping and X-ray line scans were carried out using standardless quantification techniques. An accelerating voltage of 20 kV was employed.

### **3.6 Quantitative chemical composition analysis**

Quantification of the interstitial element contents in as-received powders such as HDH titanium - 200mesh powders and sintered titanium specimens. Carbon was measured according to ASTM standard E1941-10 using a carbon-sulfur analyzer (CS-444, LECO Co., Michigan, US). Oxygen, nitrogen and hydrogen were tested utilizing a LECO oxygen-nitrogen-hydrogen analyzer (TCH-600) complying with ASTM standard E1447-09 for hydrogen and ASTM standard E1409-08 for oxygen and nitrogen.

### 3.7 Surface chemistry analysis

The surface chemistry of titanium powders and sintered specimens was assessed by X-ray photoelectron spectroscopy (XPS: AXIS Ultra DLD, Kratos) using monochromatized  $\text{AlK}\alpha$  radiation (1486.69 eV) and conducted in a high vacuum chamber with a base pressure maintained at around  $3.8 \times 10^{-6}$  Pa. XPS is a quantitative spectroscopic technology which can measure chemical state, elemental composition and electronic state of elements. A magnifying video camera was used to locate a paint flake in the approximate analysis area. Lens and iris settings of the XPS were selected to give an analysis area of  $400 \mu\text{m}$  square. Once a paint flake had been located, the lens and iris settings of the instrument were changed to generate selected areas for analysis. These analysis areas were  $300 \mu\text{m} \times 500 \mu\text{m}$  (for survey scans) and  $110 \mu\text{m}$  diameter (for narrow scans or individual elements) centered on the flake already identified in imaging mode.

A charge neutralization system was utilized and any sample charging that did occur was accounted for by shifting all the peaks with respect to the carbon 1s peak (285 eV). Survey scans were conducted from 1350 eV to 0 eV with a step size of 1 eV, a dwell time of 180 milliseconds for 5 sweeps, and a detector pass energy of 160 eV in order to determine what elements were present. Wide scans were quantified using a Shirley background. Narrow scans were performed on the carbon 1s peak, centered on 285 eV and used as an internal standard for charge referencing. The regions of Ti 2p, Cl 2p, O 1s and Mg 1s are also collected for analysis. The step size for the narrow scans was 0.1 eV, dwell time was around 300 milliseconds, and pass energy of the detector was set to 40 eV. Narrow scans were deconvoluted using a Shirley background.

#### 4. INVESTIGATION OF CHLORIDE IMPURITIES IN KROLL-PROCESSED HYDROGENATED-DEHYDROGENATED TITANIUM POWDERS

Since Kroll-processed HDH titanium powder is the most commonly utilised powder for titanium sintering, and formed the basis of the powder utilised throughout this work, an investigation to identify the chlorides impurities in the powder was carried out. Jigsaw-like agglomerates containing submicroscopic particles were observed on titanium particles and micro-compositional analysis suggested the presence of magnesium and chlorine. Further detailed surface chemical analysis carried out by X-ray photoelectron spectroscopy and corresponding curve fitting work revealed that the magnesium and chlorine mainly existed as  $\text{Mg}(\text{OH})\text{Cl}$  and titanium chloride respectively. A mechanism is provided to explain the presence of these chlorides in the Ti powder. The chlorides are considered to arise from the decomposition of hydrated magnesium chloride during the hydrogenation-dehydrogenation process, and this mechanism is supported by thermal analysis of a pure hydrated magnesium chloride. This analysis suggests that the  $\text{Mg}(\text{OH})\text{Cl}$  can further decompose into hydrogen chloride gas and magnesium oxide at high temperature. The implications of the formation of these gaseous species on the sintering of Ti powders are discussed.

##### 4.1 Introduction

In the production of titanium sponge powders, the Kroll process is the mainstream process utilising molten magnesium reducing titanium tetrachloride [1], but is being modified by recently-developed processes [43-45], such as TiRO<sup>TM</sup> [46, 47] owing to continuous production capability and low cost. Ti sponge fines are hydrogenated, ground and then dehydrogenated in the production of HDH powders. However, in this process chloride is an inevitable impurity in HDH-

produced titanium powders originating from the sponge production process in either the Kroll [1, 48, 49] or modified processes [43, 44, 46]. The existence of chloride impurities in titanium powders adversely affects titanium sintering from varied aspects such as fatigue behaviour [2, 6, 68-71] as described in Section 2.4.4. Current works [1, 45, 65] indicate vacuum distillation is the main approach to remove the residual chloride impurities in titanium sponges coupled with an advantage of in-situ removal in the reactor vessel, and about 80 % of this effort is to remove 1-2 wt%  $MgCl_2$  deep in the Ti sponges [5]. Literature shows that the chlorine impurity is typically 0.004-0.188 wt% chlorine in sponge Ti and <0.085 wt% in HDH titanium powders [6]. The generally accepted average chlorine content is 0.12-0.15 wt% for Ti sponges [30] and HDH Ti powders made from such Ti sponge products could contain up to 0.08 wt% of chlorine [2]. Since the residual chloride can play an important role in titanium sintering, attempts have been made to incorporate an effective chlorine scavenger such as the addition of 500 ppm of yttrium oxide ( $Y_2O_3$ ) [65] and 0.6 wt% yttrium hydride ( $YH_2$ ) [123] into titanium powders.

However, there is almost no past research study to the author's knowledge working on the investigation of detailed chloride identification in Kroll-processed titanium powder, which is believed to be of significance to further understand the effect of chloride on titanium sintering and the chloride scavenger development. Physical adsorption of water-vapour can always happen during the production and storage of titanium powders, which can emit mainly  $H_2O$  during heating the powder up to a few hundred degrees Celsius [48, 124]. Since the magnesium chloride can incorporate water molecules into hydrated magnesium chloride [48, 74, 75, 125], this hygroscopic property makes the situation different from, and probably even worse than, the dissociation process of sodium chloride impurities arising from the Hunter process which employs sodium to reduce titanium tetrachloride [67, 126]. The thermal decomposition kinetics of hydrated magnesium chloride is complicated in the temperature range up to 1000 °C [127-131], which is also in the temperature range of both vacuum distillation (700-850 °C) [1], and

hydrogenation and dehydrogenation (600-700 °C) [80, 132] of HDH titanium production. It is worth noting that for vacuum distillation, although high temperatures are beneficial for the evaporation of chloride, the process cannot be operated at too high a temperature in order to prevent particle agglomeration and this is considered one reason why it is difficult to remove all chloride impurities. Therefore, this work attempts to identify chloride impurities in HDH Kroll-processed titanium powders and suggest the evolution of these chlorides at high temperature accordingly.

## 4.2 Experimental

The particle size distribution was analysed by a particle size analyser (Mastersizer 2000, Malvern). The impurity contents including oxygen, nitrogen, hydrogen and carbon in the as-received powders were measured using a LECO oxygen-nitrogen-hydrogen analyser (TCH-600) and carbon-sulfur analyser (CS-444) as described in Section 3.6. The observation of microstructural morphologies and the identification of phase constituents were carried as described in Section 3.5.

The surface chemistry of as-received titanium powders was assessed by X-ray photoelectron spectroscopy (XPS: AXIS Ultra DLD, Kratos) using monochromatized  $AlK\alpha$  radiation (1486.69 eV) and conducted in a high vacuum chamber with a base pressure maintained at around  $3.8 \times 10^{-6}$  Pa. The detection lower limit for all elements except H and He is ~0.05-0.1 %. Wide scan and high resolution spectra for C1s, Mg1s, Cl2p, Ti2p and O1s were recorded. The obtained spectra were studied using CasaXPS software utilising Shirley background, and the electron binding energies (BE) were calibrated according to the C1s peak at 284.60 eV. The doublet separation energies of Ti2p were considered in accordance to the literature [133, 134] as 6.1 eV and 5.70 eV

for titanium chloride and titanium oxide respectively, and the doublet separation energy of Cl<sub>2</sub>p was assigned as 1.5 eV.

With a view to understanding and identifying the chloride species present within the commercially pure Ti powder, thermogravimetric analysis (TGA) was conducted using a Shimadzu TGA-50. Since the amount of chlorides in titanium powders is low, it is difficult to obtain repeatable thermal behaviour data of those chlorides in commercially pure titanium powders and therefore the analysis was carried out for pure hydrated magnesium chlorides (-325mesh, Sigma-Aldrich) up to a temperature of 900 °C at a heating rate of 10 °C min<sup>-1</sup> under 80 ml/min flowing argon gas protection.

### 4.3 Results and discussion

The as-measured impurity content and ASTM Grade 4 specification of c.p. Ti is listed in Table 4-1.

*Table 4-1: Impurity contents (O, C, N, H) in C.P. Ti for ASTM Grade 4 specification and as-measured titanium powder[135]*

C.P. Titanium	O (wt%)	C (wt%)	N (wt%)	H (wt%)
ASTM (Grade 4)	0.4	0.1	0.05	0.015
As-measured	0.406	0.047	0.007	0.002

It indicates that the oxygen content of the powders was comparable with the Grade 4 specification and the hydrogen, nitrogen and carbon contents were all lower than the specification. This means the as-received titanium is qualified to be assigned under ASTM Grade 4. The XRD pattern of as-received titanium powders indicates that it has a typical alpha titanium structure as

depicted in Figure 4-1(a), and the powder has a mean particle size of 50  $\mu\text{m}$  (Figure 4-1b) in accordance with the nominal powder particle size less than 75  $\mu\text{m}$ .

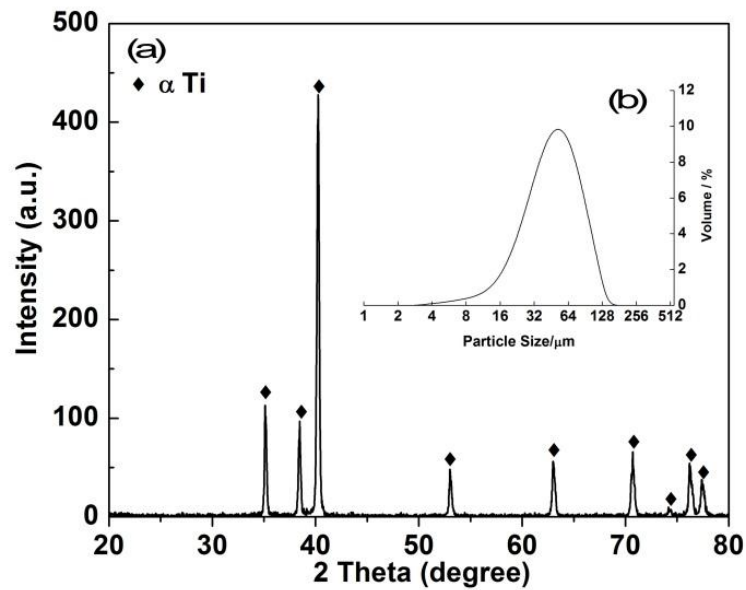


Figure 4-1: As-received HDH Ti -200 mesh powder: (a) XRD phase determination; (b) particle size distribution[135]

There is no obvious evidence showing the appearance of magnesium-related or chlorine-related peaks demonstrated in Figure 4-1, although this is not unexpected since the amount of residual chloride in HDH-processed titanium is low. However, further micro-morphology observation suggested the presence of chloride impurities in the HDH titanium powder as shown in Figure 4-2.

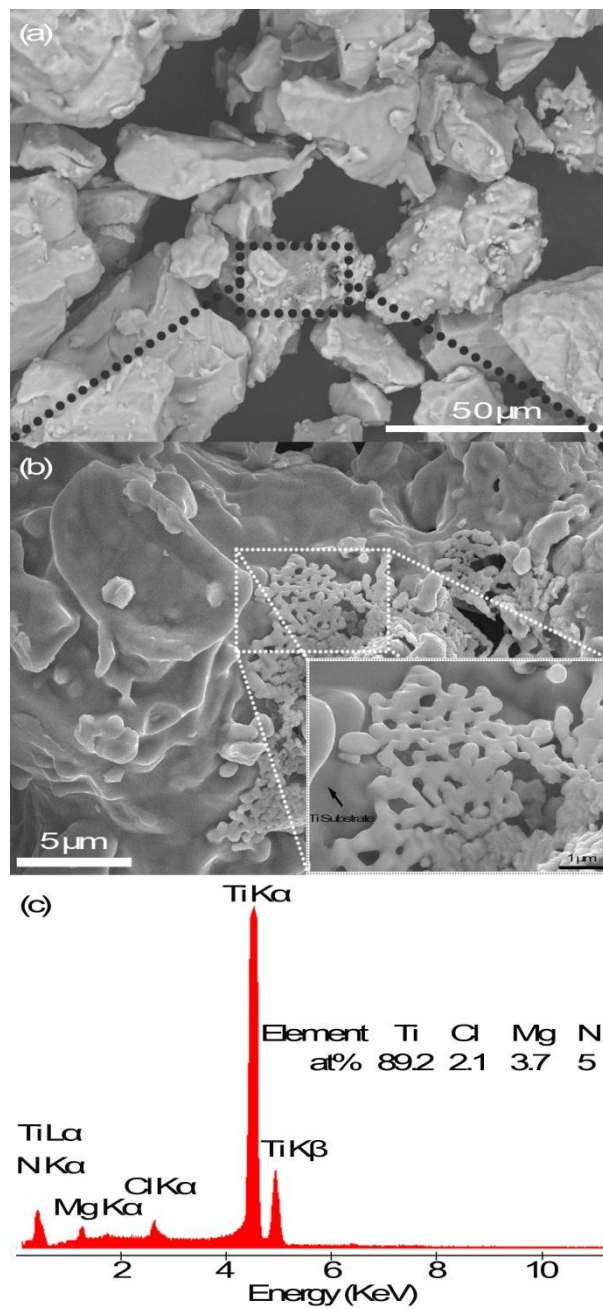


Figure 4-2: Jigsaw-like particles on the surface of as-received HDH titanium powders: a) back-scattered electron image; b) high-magnification secondary electron image of selected area on the surface of one Ti particle; c) EDS compositional analysis[135]

The back-scattered electron images indicated the presence on the surface of the titanium particles of secondary particles with an angular or blocky morphology as shown in Figure 4-2(a), and



high-magnification secondary electron images (Figure 4-2b) exposed clearly the morphology of jigsaw-like agglomerates containing submicroscopic particles on the particle surface. Compositional analysis of the agglomerates suggests that these particles contain magnesium and chlorine (Figure 4-2c). The magnesium/chlorine atomic ratio determined by EDS (3.7:2.1) is far away from the nominal ratio 1:2 of  $\text{MgCl}_2$ , which indicates it could be one kind of chlorine-deficient magnesium chloride. The observation is in accordance with the idea presented in the literature [48] that the impurities including magnesium and chlorine were located mainly on the surface of titanium particles. This makes wet chemistry such as acid leaching available to remove the chloride impurities, however, this process is no longer used extensively because it involves complicated hydration reaction between water and magnesium chlorides [1]. In order to clarify the specific magnesium chloride, surface chemical analysis was carried out on as-received titanium powders, and the survey scan and narrow scans of each element of interest can be seen in Figure 4-3.

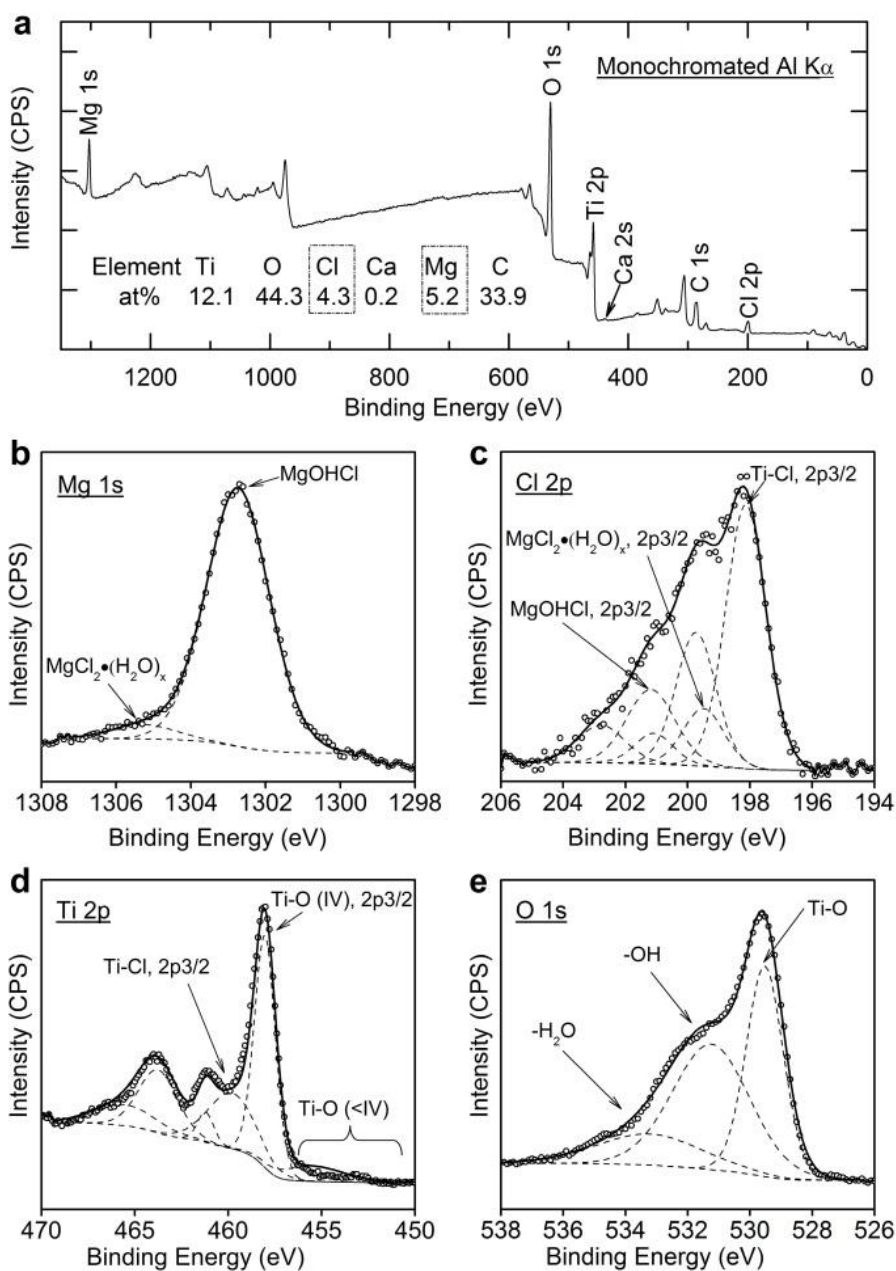


Figure 4-3: Surface chemistry of as-received titanium HDH powders: a) survey scan; b) Mg 1s; c) Cl 2p; d) Ti 2p; e) O 1s [135]

The survey analysis (Figure 4-3a) validated the existence of magnesium and chlorine on the surface of as-received titanium powders. After peak fitting of the Mg 1s region shown in Figure 4-3(b), there was a small peak observed with a BE= 1304.6 eV which is considered to be hydrated magnesium chloride in accordance with the literature [136]. The main Mg 1s peak was positioned

at a binding energy of 1302.7 eV, which is characteristic of both  $\text{Mg(OH)}_2$  [137] and  $\text{Mg(OH)Cl}$  [138] (a reaction intermediate product from the decomposition of hydrated magnesium chloride). Since the small peak was associated with the hydrated magnesium chloride, it is suggested that the main peak is  $\text{Mg(OH)Cl}$  as opposed to  $\text{Mg(OH)}_2$  since it can be the reaction intermediate from the decomposition of hydrated magnesium chloride, and is also supported by the chlorine spectrum shown in Figure 4-3(c). These two substances are identified and validated in the  $\text{Cl}2p$  narrow scan spectrum demonstrated in Figure 4-3(c). The  $\text{Cl}2p_{3/2}$  components at 201.1 eV and 199.5 eV are assigned as chlorine arising from  $\text{Mg(OH)Cl}$  and hydrated magnesium chloride respectively [138]. Additional peaks in the  $\text{Cl}2p_{3/2}$  spectra are ascribed to titanium chloride with a characteristic binding energy of 198.2 eV [137]. The  $\text{Ti}2p$  scan region indicated the presence of both titanium chloride and titanium oxide as depicted in Figure 4-3(d). The component with a binding energy of 459.8 eV is assigned as titanium chloride [139], whereas the component located at 458.0 eV can be assigned as  $\text{TiO}_2$  [140]. The spectra detected at low-binding energy range are ascribed to low-valence titanium such as titanium metal, titanium monoxide etc [48]. although the titanium dioxide thin layer is dominant on the surface of titanium particles arising from the reaction between titanium metal and the atmosphere. The  $\text{O}1s$  spectrum is fitted with three different peaks as demonstrated in Figure 4-3(e). The component with a peak at  $\text{BE}=529.6$  eV is representative of  $\text{TiO}_2$  [134] and the components at 531.2 eV and 533.2 eV are considered as hydroxyl groups [137] such as  $\text{Mg(OH)Cl}$  and the hydrated matter such as hydrated magnesium chloride [48] respectively.

A suggested mechanism for the formation of the  $\text{Mg(OH)Cl}$  and hydrated magnesium chlorides identified from XPS is presented in Figure 4-4.

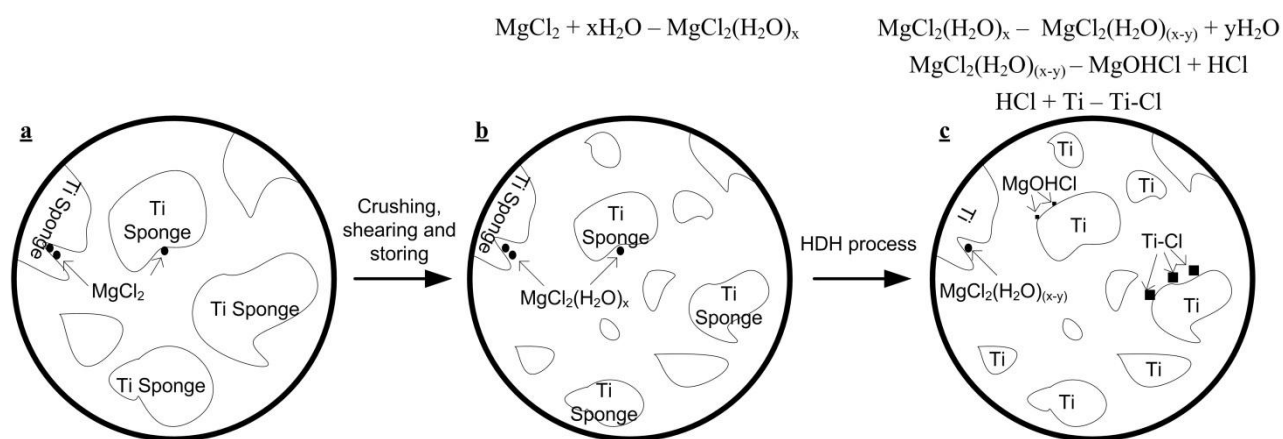


Figure 4-4: Schematic diagram of the originating process of chloride impurities in HDH titanium powders [135]

The literature indicates that it is impossible to remove all of the magnesium chloride deep in titanium sponges [30, 126], as depicted in Figure 4-4(a). Since the size of as-produced sponges is too large to be utilised, they require further crushing and shearing operations to reduce the particle size, and which are normally conducted in air [1]. The magnesium chloride in the titanium powders would be exposed to air and is expected to absorb water molecules due to its high hygroscopic property even under proper storage conditions such as in argon gas [48] resulting in the formation of hydrated magnesium chloride as illustrated in Figure 4-4(b). In order to obtain fine-sized commercially-pure titanium powders, the hydrogenation process of titanium sponges is operated at a temperature of 600-700 °C followed by dehydrogenation at similar temperatures [80, 132]. At such temperatures, it is possible for the hydrated magnesium chloride to begin to lose water molecules and form the reaction intermediate product – Mg(OH)Cl and release hydrogen chloride gas [128, 130, 141-143]. This gaseous HCl can further react with titanium and form titanium chloride which was detected by XPS shown in Figure 4-3, and is indicated schematically in Figure 4-4(c).

The presence of the  $\text{Mg}(\text{OH})\text{Cl}$  identified by surface chemical analysis in HDH Kroll-processed titanium powders, is supported by the assessment of the thermal behaviour of the pure hydrated magnesium chloride powders. The results of this analysis are presented in Figure 4-5, and show three distinct regions of mass loss on increasing the temperature from room temperature to 900 °C.

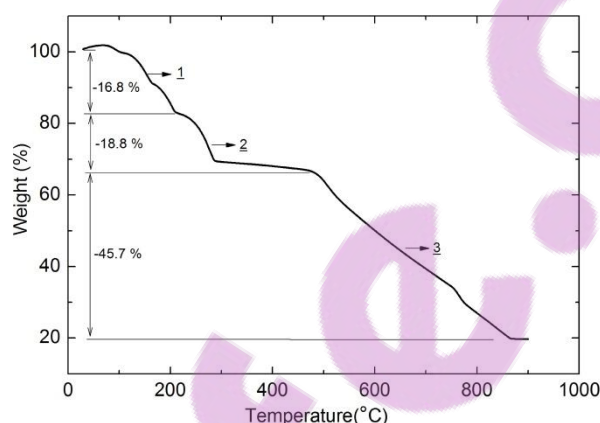


Figure 4-5: Thermogravimetric analysis (TGA) of hydrated magnesium chloride powders [135]

In the first stage of heating, the mass decreased by 16.8 % on heating from room temperature to 210 °C. This represents the loss of water molecules from the hydrated magnesium chloride  $\text{MgCl}_2(\text{H}_2\text{O})_x$  until there is only a single water molecule remaining in the hydrate ( $\text{MgCl}_2 \cdot \text{H}_2\text{O}$ ) [142]. There was a second weight loss of 18.8 % on continued heating to around 490 °C which is associated with decomposition of the monohydrate resulting in the formation of hydrogen chloride gas as well as the intermediate product ( $\text{Mg}(\text{OH})\text{Cl}$ ) [128, 130]. After calculation, if the number of water molecule  $x = 2\sim 3$ , it is feasible to give above weight loss at each stage. The final stage of weight loss, on heating to 900 °C is related to the decomposition of  $\text{Mg}(\text{OH})\text{Cl}$ . The literature [127] indicates  $\text{Mg}(\text{OH})\text{Cl}$  can directly decompose into  $\text{MgO}$  and  $\text{HCl}$  without

undergoing any intermediate step and the decomposition process is a first-order process. This thermal behaviour is represented schematically in Figure 4-6.

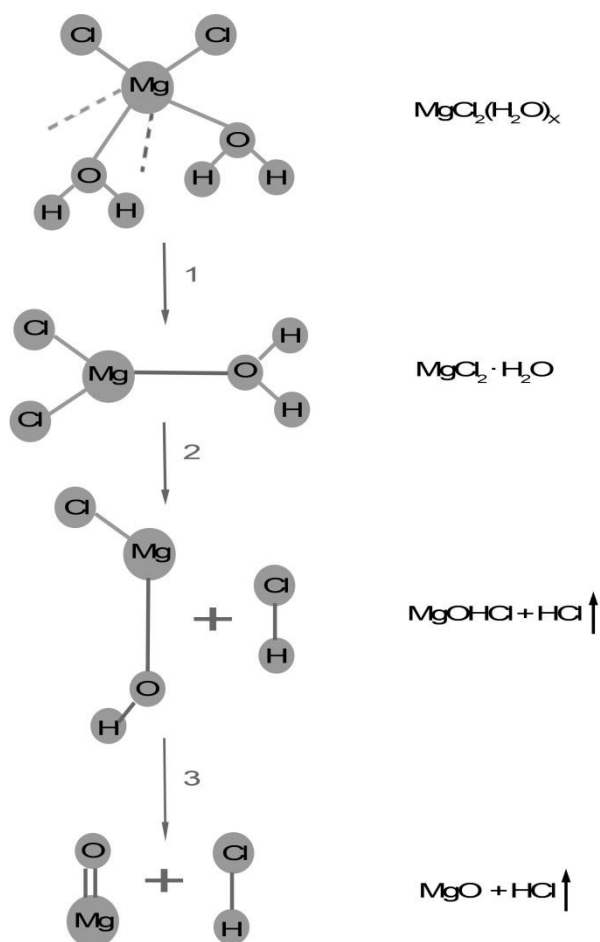


Figure 4-6: Dehydration mechanism of hydrated magnesium chlorides [135]

This thermal analysis can help to explain the presence of Mg(OH)Cl indicated from the XPS results since the HDH process is typically carried out at temperatures in the range of 600-700 °C [80, 132], and at these temperatures the Mg(OH)Cl may not have all completely decomposed as seen in Figure 4-5. Perhaps of more importance however are the implications for the sintering of these powders, which is carried out at higher temperatures typically of 1100-1400 °C [6]. The decomposition of both the monohydrate into Mg(OH)Cl and the subsequent decomposition of

Mg(OH)Cl into MgO both result in the release of HCl gas which can react with titanium to form titanium chloride, as seen in the Ti2p XPS spectrum. These titanium chlorides are also gaseous and the presence of these gaseous species can be detrimental to densification during the sintering process.

#### 4.4 Conclusions

Jigsaw-like magnesium chloride impurities in HDH Kroll-processed titanium powders were located on the surface of titanium particles and identified mainly in the form of Mg(OH)Cl and titanium chlorides by surface chemical analysis after the hydrogenation-dehydrogenation process. These chlorides are considered to arise from the decomposition of hydrated magnesium chlorides formed during sponge titanium processing, and are supported by a study of the thermal decomposition of pure hydrated magnesium chlorides which also demonstrates Mg(OH)Cl can further decompose into gaseous hydrogen chloride and magnesium oxide. The released hydrogen chloride gas and gaseous titanium chlorides may affect the sintering densification adversely. In the following chapters, chapter 5 describes titanium sintering in a graphite furnace backfilled with argon gas, followed by the discussion in regard to the effect of chloride impurities on titanium sintering shown in chapter 6.

## **5. EFFECT OF CONTAMINANTS ON MICROSTRUCTURAL EVOLUTION AND MECHANICAL PROPERTIES OF COMMERCIAL PURE TITANIUM SINTERED IN A GRAPHITE FURNACE BACKFILLED WITH ARGON ATMOSPHERE**

The previous chapter investigated the chloride impurities in HDH titanium powders, and this chapter deals with other contaminants that arise during the process of titanium sintering. Isothermal atmosphere sintering of commercially pure hydrogenated-dehydrogenated titanium powders was carried out in a graphite furnace backfilled with argon gas at various temperatures and holding times and the effects of possible contaminants (C, O, N) were studied on sintered titanium specimens. A contaminated scale was formed on the surface identified as titanium oxycarbonitride (Ti(CNO)) while cross sections were composed of only single phase alpha titanium. Microstructural observations showed that the surfaces were particle-like without any apparent densification while typical sintering phenomenon was observed in the sample interiors with increasing sintering temperature and holding time. Tensile slices were manufactured from different positions within a large-sized cylinder after the removal of the contaminated scale with a relative sintered density of 95.8 % and the corresponding tensile mechanical properties were strongly dependent on the distance of the position from the surface mainly because of the impurity gradient. An average tensile elongation of 5 % - 7 % was obtained with the highest value being 10.2%. The average ultimate tensile strength of slices increased with increasing the distance from the surface from 259.3 MPa (S3) to around 570 MPa (S4 and S5) followed by decreasing with distance increment to 470.9 MPa (S6) and 389.2 MPa (S7). The corresponding fracture mechanism changed from brittle intergranular fracture (S3), to cleavage fracture (S4) and final ductile fracture with dimples (S5 – S7).



## 5.1 Introduction

The mechanical properties of as-sintered titanium are highly sensitive to the interstitial impurity content [144, 145], where for example, the ductility of press-and-sintered c.p. titanium with an oxygen content of 3000 ppm (elongation: 11%) is less than 1/3 of specimens with oxygen content of 700 ppm (elongation: 37.1%) even though both relative sintered densities are the same at 98% [2, 5].

Since titanium has a high affinity for nitrogen, oxygen, hydrogen and carbon, atmosphere sintering is typically conducted in an inert atmosphere such as argon [9, 146]. It is reported that Kroll in 1937 conducted the first sintering trials of 14 Ti binary alloys in argon atmosphere [5]. Subsequent work in the late 1940s and early 1950s saw some other examples of the sintering of titanium mill products [5, 147]. Recently researchers also sintered porous Ti in argon atmosphere [148]. However, purification of the inert atmosphere is still required [147] before entering into the hot zone because even small amounts of reactive gases (nitrogen, oxygen and hydrogen) are detrimental and makes sintered specimens brittle. To address this issue, Arensburger et al. developed a purification setup by incorporating argon flowing through pre-heated titanium sponges (900 – 1000 °C) [146]. An alternative solution is to reduce the oxygen partial pressure in the argon gas further by utilizing reaction with graphite materials in the furnace such as KYK Oxynon furnace [149-151]. As a result, extremely low oxygen pressure can be generated by the reaction between oxygen and carbon, which is considered to be able to reduce oxides such as titanium oxide ( $\text{TiO}_2$ ) into metal [149]. This interesting result indicates that the oxygen content in titanium specimens sintered under argon in Oxynon furnace could be lower than those sintered under vacuum while the ductility is lower for specimens sintered in argon atmosphere than sintered under vacuum [150]. This is possibly because of the adverse effects of other impurities and/or sintered density difference.

Therefore, a detailed report on the microstructural evolution and property characterization of titanium samples produced by atmosphere sintering in a graphite furnace, and how they depend on impurity distribution, is still required. HDH titanium powders produced from titanium sponges fabricated by the Kroll process are favourable for sintering from an economical viewpoint [7, 17, 42]. Although industrially Ti alloys are more widely used than commercially pure Ti, in PM titanium sintering the atmosphere can be expected to play a large role because of the reactive nature of the powder, and this can be complicated by alloying species. This work thus focuses on understanding the effects of possible contaminants on the sintering and properties of C.P. Ti during sintering in a reducing atmosphere produced through a combination of inert gas and graphite construction.

## **5.2 Experimental**

### **5.2.1 Materials, compaction and sintering**

HDH C.P. titanium powder (-200 mesh, <75  $\mu\text{m}$ ) was employed in this study. The powder morphology, particle size distribution, interstitial impurity contents and historical production process have been reported in chapter 3. The powders were pressed uniaxially under a compaction pressure of  $400 \pm 50$  MPa into cylindrical disc samples 12 mm in diameter and 5 to 8 mm thick. The compacts were then sintered at three different temperatures (1100, 1250 and 1400  $^{\circ}\text{C}$ ) and three different holding times (4, 6 and 8 hours). A larger disc shaped specimen with diameter of 32 mm and height of around 40 mm was uniaxially pressed at a pressure of 200 MPa followed by cold isostatic pressing (CIP) under a pressure of 600 MPa to minimize the density inhomogeneity for large-sized specimens, and sintered at a temperature of 1250  $^{\circ}\text{C}$  with a soaking time of 4 hours. Tensile specimens were machined from different positions of this large cylinder.

The compacts were placed on a boron nitride plate at the centre of the hot zone in the graphite furnace shown in chapter 3. After the specimens were loaded, the furnace was evacuated to a vacuum level of 0.1 to 0.01 Pa and heated to 850 °C with a heating rate of 5 °C min<sup>-1</sup> with a target to remove possible volatiles before gas backfilling. In order to avoid possible gas leaking at high temperature, at this stage argon gas (purity 99.99%) was back filled to the furnace and a pressure of 1.1 atm ( $1.1143 \times 10^5$  Pa) was maintained until the end of sintering. The positive net furnace pressure is designed to avoid the inwards air flow from the ambient atmosphere.

### 5.2.2 Characterization

The sintered density was measured according to Archimedes method (ASTM B962-08 standard) with deionized water. Microstructural observations were carried out using an environmental scanning electron microscope (ESEM) (Quanta 200F, FEI). Semi-quantitative compositional analysis was conducted using energy dispersive spectrometry (EDS). Optical microscopy coupled with polarized light optics (Olympus) was utilized to examine the polished cross-sections of sintered samples. Phase constituents were determined by X-ray diffraction (XRD) analysis using a D2 PHASER (Bruker AXS, Germany) equipped with Cu X-ray source. The patterns were collected over a  $2\theta$  range of 20-80° with a step size of 0.02°. The measurement of interstitial contents including carbon, hydrogen, oxygen and nitrogen in as-received powders and sintered specimens is described in chapter 3.

### 5.2.3 Mechanical testing

Tensile slices were manufactured from the as-sintered large cylinder with a diameter of ~27 mm and height of ~30mm after removal of the contaminated scale as shown in Figure 5-1.

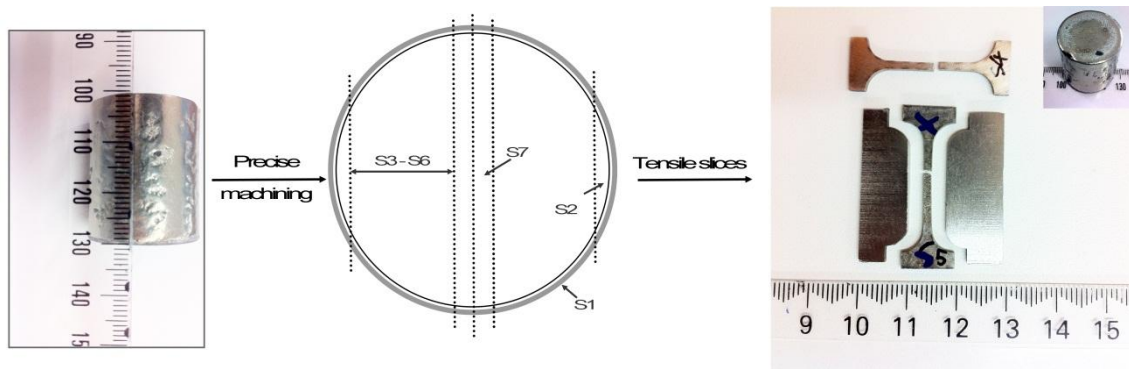


Figure 5-1: Schematic preparation of slices taken from the as-sintered cylinder

As schematically shown in Figure 5-1, the layer designated as S1 represents the contaminated scale with a thickness of 0.3 – 0.5 mm. This scale contained cracks and was only loosely adherent and could be easily removed to expose the interior bulk titanium. The thickness of S2 was ~1.5 mm, which was too thin and therefore not suitable for tensile testing. The thickness of other slices (S3-S7) was 2 mm, and tensile samples were machined from these slices (~2 mm × 2 mm cross-section, 10 mm gauge length). Tensile tests were performed on an Instron mechanical tester (Model: 3367, Instron Co., Norwood, MA) with a crosshead speed of 0.1 mm min<sup>-1</sup> (initial strain rate: 1.67 × 10<sup>-4</sup> s<sup>-1</sup>). The precise displacement was determined using an extensometer with a gauge length of 8 mm (model: 2630-120, Instron Co., Norwood, MA). Two tensile specimens were prepared for each point.

## 5.3 Results

### 5.3.1 Density measurement

The sintered densities and corresponding densification levels are illustrated in Figure 5-2 for specimens sintered at varied temperatures (1100 °C, 1250 °C and 1400 °C) and holding times (4

hours, 6 hours and 8 hours). It should be noted that these measured densities include the contaminated outer surface which was shown to be porous (Figure 5-3 and Figure 5-5) and are therefore lower than the actual density of the interior of the samples.

Densification level  $\varphi$  is typically defined as

$$\varphi = (\rho_s - \rho_g) / (\rho_{th} - \rho_g) \quad (5-1)$$

where  $\rho_s$  is sintered density,  $\rho_g$  green density and  $\rho_{th}$  theoretical density. The densification level offers an evaluation method for the level of porosity elimination of green compacts by sintering.

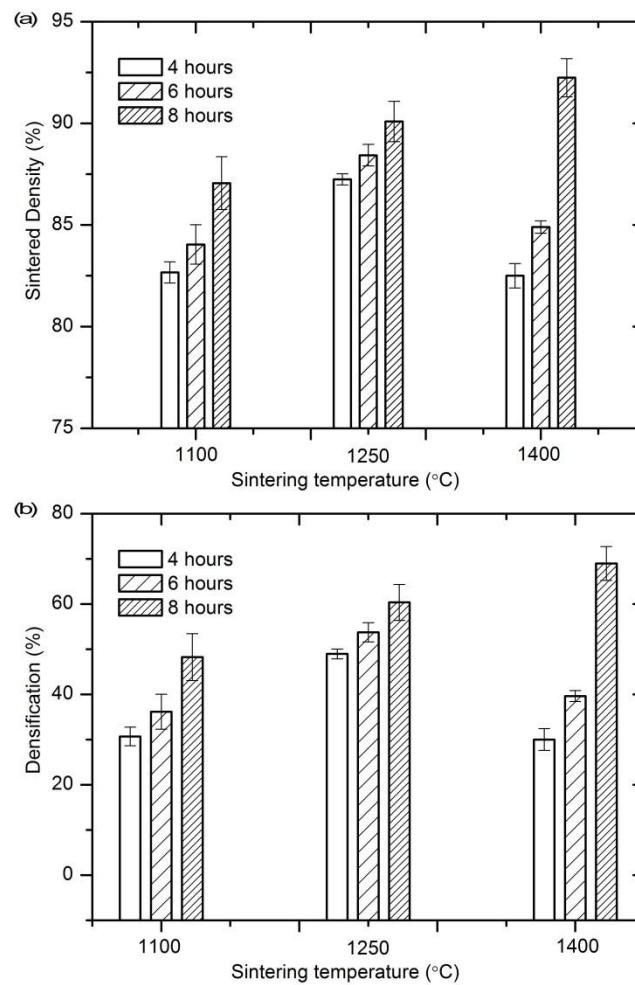


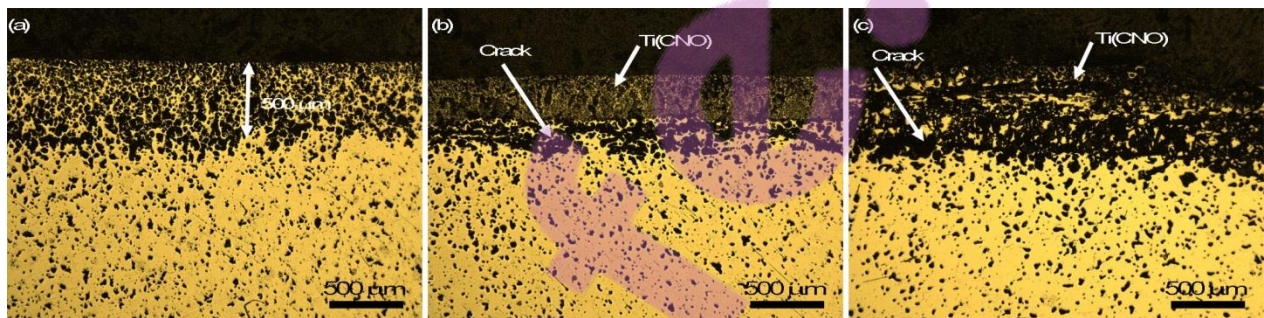
Figure 5-2: Relative sintered densities (a) and densification levels (b) under various sintering conditions

Figure 5-2(a) shows the sintered densities as a function of sintering temperatures and holding times. In general, all sintered densities are low in the range of 82.5 % - 92.5 % theoretical. This is mainly due to the formation of the porous surface scale and cracks between the surface and the interior as seen in Figure 5-3. In Figure 5-2(b), although the porosity in compacts was decreased gradually with increasing holding time for all three sintering temperatures, the elimination level of porosity was still low. For example, almost all densification levels of specimens sintered with a holding time 4 and 6 hours at all temperatures were between around 30 - 50 %. If the surface

scales were removed before density measurement, the corresponding sintered densities are expected to be higher than specimens containing contaminated scales shown in Figure 5-2.

### 5.3.2 Metallography of the bulk sintered samples

Metallographic observations of the cross sections of samples sintered at varied temperatures for 4 hours are shown in Figure 5-3.



*Figure 5-3: Macrographs of cross-sections of sintered specimens at different sintering conditions: a) 1100 °C, 4 hours and b) 1250 °C, 4 hours and c) 1400 °C, 4 hours*

It is clearly shown that a contamination scale was formed at different temperatures during sintering and interestingly, the thickness of the scale (300 - 500 μm) did not appear to increase with sintering temperatures. The scale is suggested as being Ti(CNO) as described in earlier work [152] and discussed below. At a sintering temperature of 1100 °C the interface between the contamination layer and the substrate titanium is clear but the bonding was still intact. On the other hand, at higher sintering temperature (1250 °C and 1400 °C), cracks were observed at the interface and this makes it easy to peel off the contamination scale, as mentioned previously.

Crossed polarized light microscopy was employed to investigate the grain size and pore size and morphologies as shown in Figure 5-4.

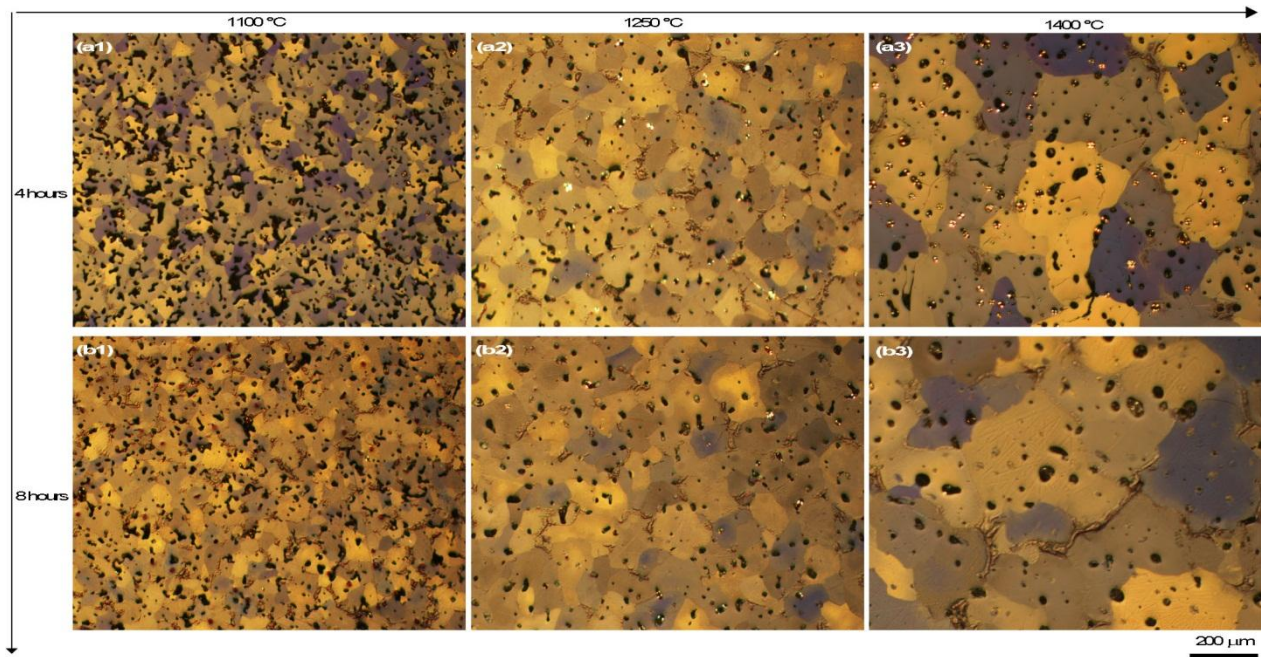


*Figure 5-4: Macrographs of cross sections of sintered specimens at various sintering conditions using crossed polarized light*

Typical sintering phenomena are highlighted in Figure 5-4 in regard to pore size, pore shape and grain size. Pores observed in the interior of the sample sintered at 1100 °C with a holding time of 4 hours were irregular and open with an average size of 50-100 μm formed by particle rearrangement and initial neck formation. The shape of these pores indicates that under these conditions the samples were still in the early stages of densification [14]. Although irregular pores were still observed in the cross section, the number and the size decreased for specimens sintered at the same temperature with a longer holding time of 8 hours. Pore spheroidizing occurred at the high temperatures of 1250 °C and 1400 °C, and spherical and isolated pores were



observed. At a temperature of 1250 °C most of the pores were observed to be located either along grain boundaries or sit at the triple junctions, however, when the sintering temperature increased by 150 °C to the highest 1400 °C some of these pores became trapped within grains due to the large grain growth at high temperature. The size of pores at 1250 °C was typically 20-40 microns with a 4-hour holding. In comparison some pores were enlarged to around 50  $\mu\text{m}$  for specimens sintered at higher temperature (1400 °C). When the holding time was increased to 8 hours, those small pores vanished and therefore the number of pores decreased for both 1250 °C and 1400 °C. This is in agreement with the mechanisms of sintering kinetics that the linear shrinkage rate is proportional with holding time [13]. However, once the pores are closed and the gas pressure inside is equal to that outside then increasing time further would have little effect.

It is also observed that there was a dramatic grain growth, with grain size increasing from around 50  $\mu\text{m}$  at 1100 °C, to 90  $\mu\text{m}$  about at 1250 °C and around 200  $\mu\text{m}$  at 1400 °C with a constant soaking time of 4 hours. There was less remarkable grain growth at any temperature when doubling the soaking time to 8 hours, which indicates that grain growth is highly sensitive to the sintering temperature but not so dependent on the holding time.

### 5.3.3 Close-up observation of surface contaminants

Microstructural observations, and semi-quantitative analysis, of as-sintered specimens' surfaces are presented in comparison with as-received titanium powders demonstrated in Figure 5-5.

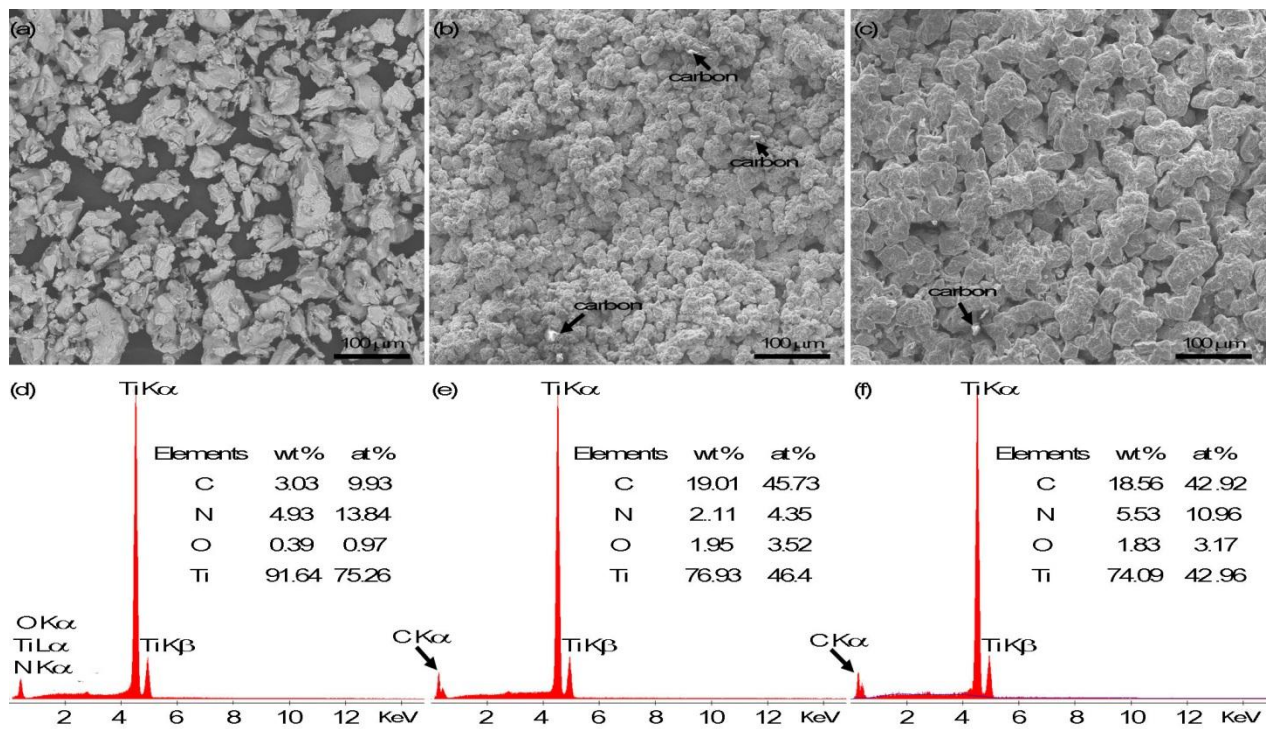


Figure 5-5: Surface morphologies and semi-quantitative EDS analysis of as-received Ti powder (a, d), sintered specimen surface at 1250 °C with a 4-hour holding (b, e) and sintered specimen surface at 1400 °C with a 4-hour soaking (c, f)

There was no obvious densification of the surface of as-sintered specimens presented in Figure 5-5(b) and Figure 5-5(c) although the bonding and neck formation between particles can be identified. In addition, the size of particles on the surface of as-sintered specimens was similar to that of the as-received titanium powders shown in Figure 5-5(a). Shiny particles, identified as carbon, were also detected on the surface of as-sintered specimens, which indicates that the surface could be carbon-rich. This is validated by the spectral analysis conducted using EDS. The results illustrate that the presence of carbon peaks in Figure 5-5(e) and Figure 5-5(f) but not seen in the spectra of as-received Ti powder presented in Figure 5-5(d). Semi-quantitative results demonstrated that the content (at %) of carbon can account for almost 50% of the surface of as-

sintered specimens. EDS testing indicates that the existence of mainly carbon and titanium with small amounts of oxygen and nitrogen on the surface of sintered specimens.

#### 5.3.4 Phase characterization of the surface and the interior

It has been noted that there is noticeable microstructural distinction between the surface and the interior of the samples as shown in Figure 5-3 and reinforced by Figure 5-4 and Figure 5-5. Although the cross sections revealed reasonably dense samples (Figure 5-4), the surface was particle-like without any evident densification even when the sintering temperature was high (1250 °C and 1400 °C Figure 5-5). These results highlight the difference between the surface and the interior of specimens sintered in the graphite furnace filled with argon gas. Corresponding characterization of the constituent phases was carried out by XRD and the results are presented in Figure 5-6.

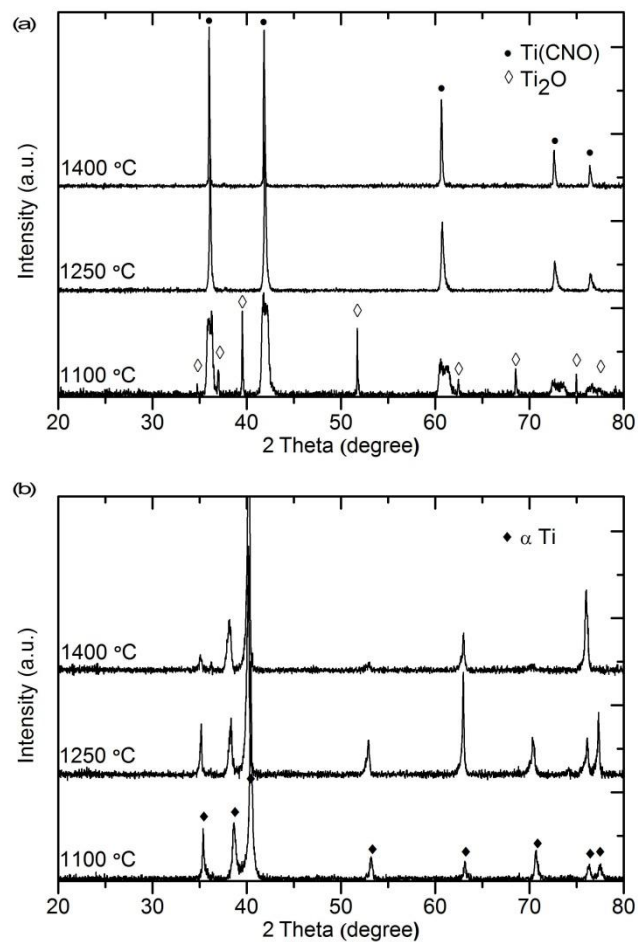


Figure 5-6: XRD patterns of the surface (a) and cross-sections (b) of sintered Ti specimens with a holding time of 4 hours

In all of the sintered samples, the surfaces were contaminated and the main phase of the contaminant layer was identified as titanium oxycarbonitride  $\text{Ti}(\text{C}_{0.53}\text{N}_{0.32}\text{O}_{0.19})$  referred as JCPDS # 50-0681, a solid solution of titanium monoxide, titanium carbide and titanium nitride. For the samples sintered at 1100 °C a minor phase of  $\text{Ti}_2\text{O}$  (JCPDS # 73-1582) was also detected. In contrast, the only phase observed in the interior of samples sintered at all temperatures was alpha titanium indexed as JCPDS # 44-1294.

### 5.3.5 Mechanical properties and fractography

Since it was demonstrated that the surface was contaminated and composed of a different titanium phase to the interior of the samples, the tensile mechanical properties of slices taken from different sections from the surface were assessed by cutting sections from the large cylinder sintered at a temperature of 1250 °C with a 4-hour soaking time, as shown in Figure 5-1. The mechanical properties are illustrated in Table 5-1.

*Table 5-1: Tensile mechanical properties of titanium slices prepared from a large-sized cylinder sintered at 1250 °C with a holding time of 4 hours*

Specimen	Tensile strength (MPa)	0.2% Proof strength (MPa)	Elongation (%)	Young's modulus (GPa)
S3	259.3 ± 25.6	—	0.235 ± 0.024	110.1 ± 0.1
S4	566.1 ± 14.8	497.5 ± 22.5	3.02 ± 1.517	103.5 ± 5.8
S5	576.3 ± 14.7	490 ± 10	6.204 ± 4.019	102.6 ± 1.8
S6	470.9 ± 37.5	387.5 ± 27.5	6.604 ± 1.022	110.5 ± 1.3
S7	389.2 ± 91.2	305 ± 85	5.313 ± 0.086	98 ± 4.7

Since the contaminated scale (S1) was too brittle and the outer slice (S2) was too small to fabricate tensile specimens, there was no such mechanical data available for S1 and S2. The results in Table 5-1 indicate that S3 was still brittle with almost no ductility (0.235% average elongation) although it was a considerable distance (2 mm) from the contaminated surface. Samples taken from further within the interior of the sample showed improved mechanical properties with an average tensile strength of 566.1 MPa and elongation of 3.02 % for tensile slice S4. For deeper slices (S5, S6 and S7), the average elongation were in the range of 5 % - 6 % with the largest elongation of 10.2 % being observed for S5. However, the ultimate tensile strengths and proof strengths decreased with increasing distances from S5 towards the centre of

the sample, from 576.3 MPa and 490 MPa, respectively for S5 to 470.9 MPa and 387.5 MPa for S6 and 389.2 MPa and 305 MPa for S7. This behaviour is discussed further below. In addition, although the strength and elongation were varied between different slices, the Young's moduli of all slices were almost constant at different positions. Representative engineering stress-strain curves of varied slices are depicted in Figure 5-7.

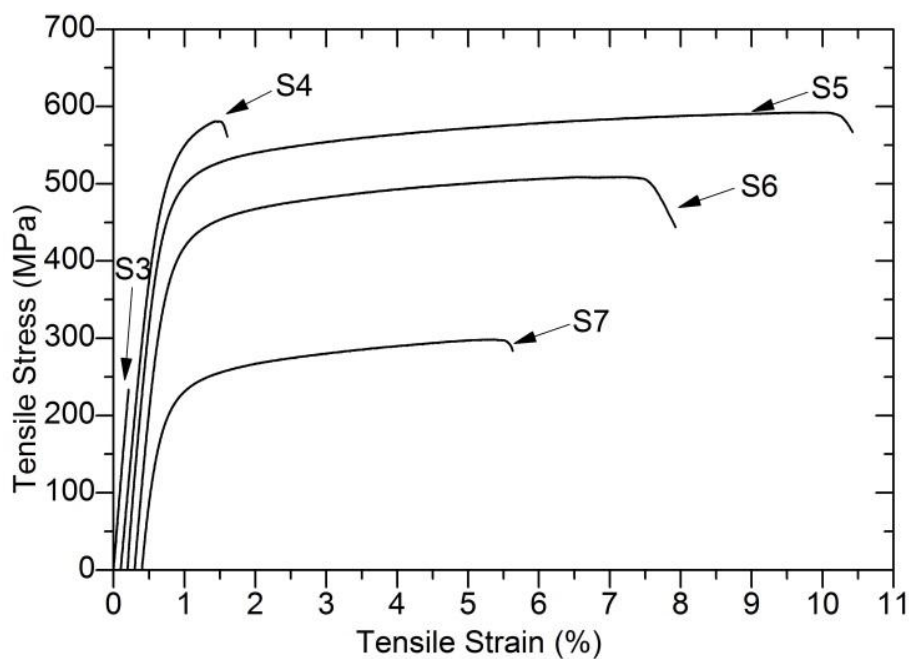


*Figure 5-7: Representative engineering stress-strain curves for slices prepared from different positions*

Corresponding fractographs of tensile slices are illustrated in Figure 5-8.

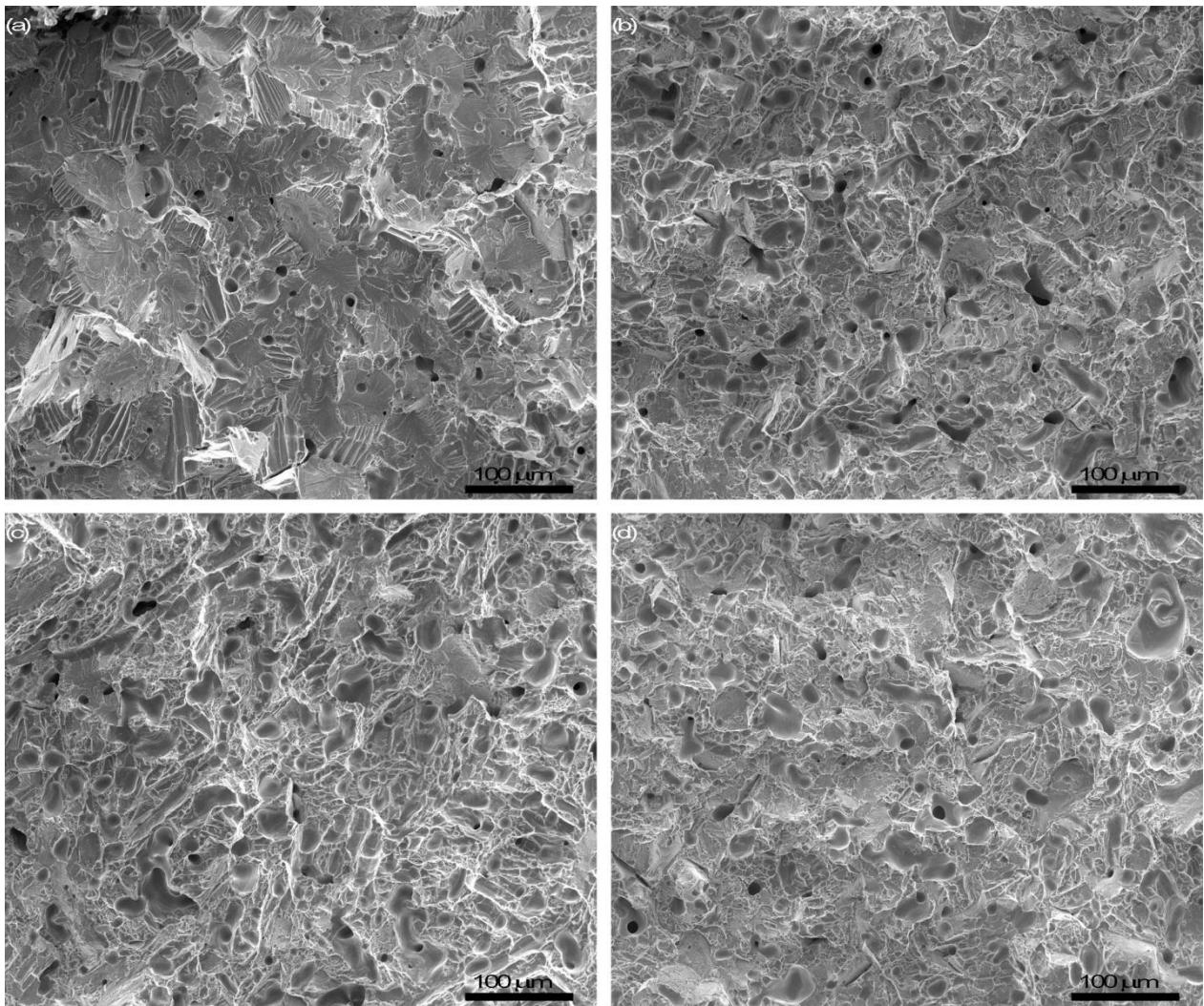


*Figure 5-8: Fracture surfaces of tensile slices from sintered titanium samples: (a) S4, (b) S5, (c) S6, and (d) S7*

Pores were observed in samples from all positions from S4 to S7, which indicates that full densification was not achieved for these specimens. Smooth cleavage facets and tear ridges are presented in Figure 5-8(a) and this fractograph indicates that the main failure mechanism of tensile slice S4 is cleavage fracture. Serpentine dimple walls shown in Figure 5-8(b-d) indicate the significant plastic deformation occurring during testing for S5, S6 and S7 [39].

## 5.4 Discussion

### 5.4.1 Densification

The increase in sintered density by 5 % - 10 % theoretical density with an increase in holding time from 4 to 8 hours shown in Figure 5-2(a) for all three temperatures is due to increased time to allow complete neck formation. This is in accordance with the observation presented in Figure 5-4. For specimens held for the same period of time, the higher temperature generally favours higher density due to faster diffusion, although there was an exception for the specimens sintered at 1400 °C with holding times of 4 and 6 hours which had lower density than samples held for the same time at lower temperatures. Since Figure 5-4 demonstrated low porosities in the interior of specimens sintered at the higher temperature, it is considered that the low measured density is a result of the presence of the crack formed just below the surface at the highest temperature of 1400 °C seen in Figure 5-3(c). The corresponding densification levels were depicted in Figure 5-2(b). Generally the elimination of pores in the green bodies was quite limited after sintering with the highest percentage of about 70 % seen in specimens sintered at the temperature of 1400 °C with a holding time of 8 hours. This again is thought to be due to the formation of the contaminated porous surface and cracks below the surface. Therefore, it is still difficult to quantitatively assess the densification of the interior although Figure 5-4 demonstrated that porosities decreased with sintering temperature and holding time. The results of the sintered density and densification for the large-cylinder specimen after peeling off of the porous contaminated scale are illustrated in Table 5-2.



*Table 5-2: Densities and densification level for large cylinder prepared for tensile testing*

Specimen	Green density (200 MPa Uniaxial, %)	Green density (600 MPa CIP, %)	Sintered density (%)	Densification (%)
Cylinder	55.5	87.0	95.8	69.2

From Table 5-2, it can be seen that cold isostatic pressing at 600 MPa dramatically increased the green density from 55.5 to 87 %. After sintering at a temperature of 1250 °C with a holding time of 4 hours, the density was increased to 95.8 % with a densification level of 69.2 %. This sintered density is much higher than specimens shown in Figure 5-2. The literature indicates that about 95 % relative sintered density of titanium and titanium alloys would be acceptable for non-fatigue applications in regard to the densification and sintered specimens with sintered densities as low as 92 % are suitable for feedstock performs for following hot working [107]. Therefore, with suitable sintering conditions, as observed for the large-cylinder specimen, it is possible to produce sufficient densification for non-fatigue applications after isothermal atmosphere sintering. This is further supported by the tensile mechanical properties with the highest ultimate tensile strength of around 600 MPa and the largest elongation of about 10 % shown in Table 5-1 and Figure 5-7.

The presence of a positive gas atmosphere during sintering may be considered detrimental to densification since it can result in difficulties for pore closure because of gas pressure in the pores. In addition, vacuum sintering could offer an extra advantage to remove volatiles such as hydrogen from titanium compacts, which cannot be realised by sintering in an atmosphere [5]. Thus, it is logical to propose that the densification could be improved further if the sintering is carried out under vacuum. Such work is shown in chapter 7 to study the comparison between vacuum sintering and atmosphere sintering in the graphite furnace.

In the intermediate and final stages of sintering, the grain size ( $G$ ), pore diameter ( $d_p$ ) and fractional porosity ( $\epsilon$ ) are related by [13]:

$$\epsilon = \pi(d_p/G)^2 \quad (5-2)$$

This relationship suggests that that the grain size will increase as either the pores coarsen, for the same level of fractional porosity, or as the amount of porosity decreases for the same size pore. This complies with the observation seen in Figure 5-4 which showed that the grain growth increased with the amount of porosity decreasing for the similar size pores because of the absence of the pore pinning effect against grain growth [14].

#### 5.4.2 Effect of interstitials on microstructure evolution and mechanical properties

The contaminated scale indexed as Ti(CNO), a compound of TiC, TiN and TiO, was formed on the surface at all three temperatures as illustrated in Figure 5-6 and is due to the high affinity of titanium for interstitials such as carbon, oxygen and nitrogen [50]. The main carbon source is from the furnace's graphite heating elements and graphite liner, and the sources of oxygen and nitrogen basically come from the backfilled argon and/or low vacuum level before backfilling argon gas. The only phase observed in the interior of the samples was alpha titanium with no presence of the contamination phase. The phase determination highlighted the difference between the surface and the cross section due to the effect of the interstitial contamination. The interstitial contamination elements were carbon, oxygen and nitrogen on the surface of sintered specimens further determined by semi-quantitative EDS testing as demonstrated in Figure 5-5. The carbon arises from the graphite heating element and insulation within the furnace and both oxygen and nitrogen came from the furnace atmosphere.

In order to further understand the formation of the surface scale resulting from the contamination of interstitials and to explain the formation of the cracks along the interior/surface interface presented in Figure 5-3(b) and Figure 5-3(c), a formation mechanism is schematically shown in Figure 5-9.

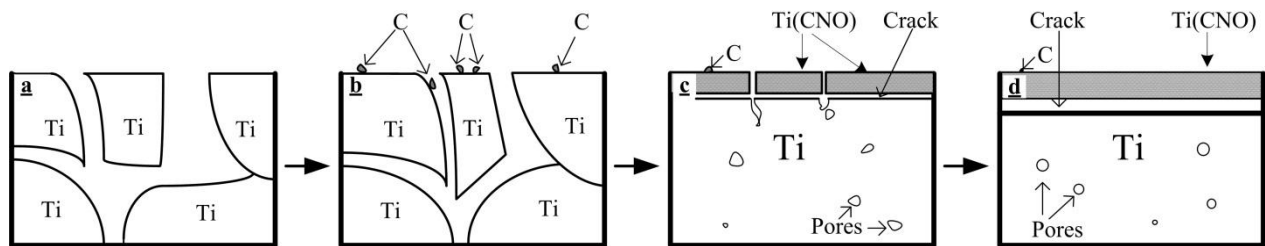


Figure 5-9: Schematic of the formation process of the scale and cracks

The original titanium compacts after pressing are depicted in Figure 5-9(a) where there is still significant porosity in the green body. Upon heating, sintering shrinkage would occur and the carbon pick-up may occur from the interior of the furnace, potentially from the elements or insulation as illustrated in Figure 5-9(b). With increasing the temperature the titanium would react with the carbon at the surface as well as with the oxygen and nitrogen originating from the backfilled argon and form the titanium carbonitride (Ti(CNO)), a compound of TiC, TiN and TiO shown in Figure 5-9(c). Since the sintering densification temperature is highly dependent on the melting point, there is no apparent sintering shrinkage for the contaminated scale when it is in the sintering temperature range of titanium between 1100 °C and 1400 °C applied in this study (the melting points of TiC (3065 °C) and TiN (3290 °C) are much higher than titanium's melting point (1668 °C) [153]. Therefore, the cracking along the interface can be expected to be due to differential shrinkage (Figure 5-9c) When increasing the sintering temperature, the crack would become more evident and wider because more sintering shrinkage would be seen for the interior

schematically seen in Figure 5-9(d). In addition, any unreacted carbon may be left on the surface as presented in both Figure 5-9(c) and Figure 5-9(d).

The formation of the cracks may prevent the interior from interstitial contamination to some extent due to the physical separation between the interior and the contaminated surface thereby being beneficial to the mechanical properties even though it results in an apparently lower overall density. In addition, because such cracks were also present in the large-cylinder specimen, it was easy to peel off the scale. However, it has to be noted that some diffusion of interstitials would still happen in the interior and form titanium based interstitial-rich solid solutions. Quantitative tests of interstitial element contents were conducted on both the as-received titanium powders and from the sintered specimens taken from different positions within the sample as shown in Table 5-3.

*Table 5-3: Interstitial contents of different slices and as-received titanium powders*

Interstitials	C (wt. %)	H (wt. %)	O (wt. %)	N (wt. %)
S1	7.38	0.0084	8.54	0.3
S2	0.086	0.016	0.65	0.034
S3	0.084	0.016	0.60	0.028
S4	0.048	0.016	0.50	0.030
S5	0.038	0.016	0.44	0.030
S6	0.032	0.016	0.40	0.026
S7	0.030	0.016	0.42	0.028
AR powder	0.047	0.002	0.406	0.007
ASTM (grade 4)	0.1	0.015	0.4	0.05

From Table 5-3, it can be seen that the interstitial contents of carbon, oxygen and nitrogen in the outer slice (S1) are much higher than the other slices and the as-received titanium powders. This further validates that the surface had been contaminated especially by carbon and oxygen. The

carbon and oxygen contents decrease with the distance from the surface, whilst the hydrogen and nitrogen contents are essentially constant. The carbon and oxygen contents in the interior of the sample were similar to those of the as-received titanium powders whilst the hydrogen and oxygen were higher. The amounts of all of the interstitial elements were below that specified for ASTM Grade 4 Ti shown in ASTM B348-11.

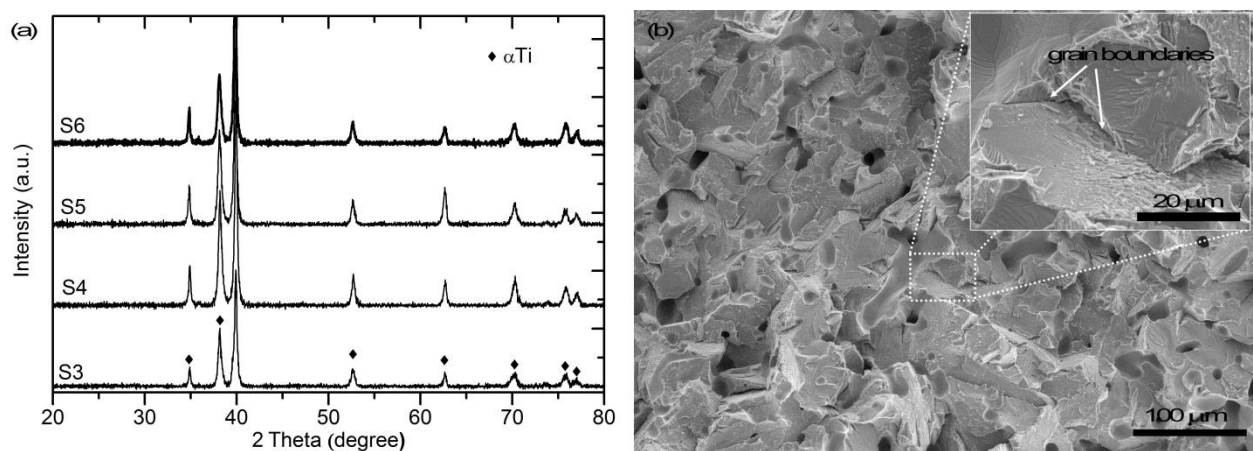


Figure 5-10: Phase constitutes of tensile slices manufactured from different positions of the large cylinder (a); fracture surface of S3 (b)

The mechanical properties of S3, including both ultimate tensile strength and tensile ductility, were extremely low compared to the other samples. Phase analysis of individual slices taken from different positions demonstrated that only alpha titanium phase was detected for all slices (Figure 5-10a). However, the fracture surface of S3 shown in Figure 5-10(b) is different from the other slices shown in Figure 5-8. This Figure shows that the main fracture mechanism of S3 is considered to be brittle intergranular fracture, suggested by the observation of clear grain boundaries pointed out in Figure 5-10(b). Such fracture usually occurs when there is a weak and brittle phase present at the grain boundaries. Although the Ti(CNO) phase was not detected for

this sample it is thought that the interstitial elements may have exceeded the solid solution limit in titanium at room temperature and thus precipitate from the grains and form the secondary phase along grain boundaries. This can be understood from the Ti-C phase diagram shown in chapter 2 which demonstrates the carbon solution limit in titanium matrix is low (0-0.4 wt% in alpha titanium).

For specimens taken from deeper within the sample, the lower interstitial contents are accompanied by a transition in fracture mechanism from brittle intergranular fracture (S3), cleavage fracture (S4) to final ductile fracture with dimples (S5-S7). This probably indicates that, because of their lower concentration, the precipitation of interstitial elements from Ti grains did not occur and the dominant effect of the interstitial elements becomes solid solution strengthening. Therefore, although all specimens showed better mechanical properties than S1, the decrease in strength for specimens taken from the center of the sample (S6 and S7) are thought to be due to the lower interstitial content resulting in less solid solution strengthening, in accordance with the literature [50].

*Table 5-4: Relative sintered densities for slices taken from the large cylinder*

Slices	S3	S4	S5	S6	S7
Sintered densities (%)	$95.7 \pm 0.1$	$95.6 \pm 0.3$	$95.9 \pm 1.0$	$95.3 \pm 0.1$	$95.8 \pm 0.2$

Theoretically for dense titanium the ductility should decrease with increasing the oxygen content due to the restriction of twinning and prismatic slip [63]. For the samples studied here, although this was observed towards the outer surface (S3 and S4) the average ductility of specimens from further within the body of the sample (S5-S7) were similar. Density measurements of the

individual slices given in Table 5-4 show that all specimens had a similar density and there was about 4% porosity in all cases. This similar density, along with the fact that the hydrogen content in particular was similar for all samples, can possibly help explain why the ductility was almost constant.

## 5.5 Conclusions

This work has investigated the sintering of commercially pure titanium powders in a reducing atmosphere utilizing argon gas in a graphite lined furnace. Due to contamination from within the furnace, a Ti(CNO) scale formed on the surface with a thickness of 300 - 500  $\mu\text{m}$ . However, the interiors of sintered specimens were pure single phase alpha titanium and typical sintering phenomena were observed. With increasing sintering temperature, irregular and open pores in the interior of specimens sintered at 1100  $^{\circ}\text{C}$  with an average size of 50-100  $\mu\text{m}$  became isolated and spherical pores with average diameter of 20 – 50  $\mu\text{m}$  were observed in the interiors of samples sintered at 1250  $^{\circ}\text{C}$  and 1400  $^{\circ}\text{C}$ . Grain sizes increased from around 50  $\mu\text{m}$  at 1100  $^{\circ}\text{C}$ , to around 90  $\mu\text{m}$  at 1250  $^{\circ}\text{C}$  and 200  $\mu\text{m}$  at 1400  $^{\circ}\text{C}$  for the specimens sintered with the same 4-hour soaking time.

Tensile mechanical properties of slices manufactured from a larger sintered sample with a relative sintered density of 95.8 % illustrated that the specimens from the interior of the sample had better mechanical properties than those taken from closer to the surface (S3). The average ductility increased with the distance from the surface from 0.23 % (S3), 3 % (S4) to around 6 % (S5 – S7). The average ultimate tensile strength of specimens S4 and S5 were over twice as high as that of the specimen taken from the surface (S3). Whilst still higher than the surface specimen, the strength of specimens taken from the center of the sample decreased from 570 MPa (S4 and

S5), to 471 MPa (S6) and 389 MPa (S7), due to lower interstitial contents. The corresponding fracture mechanism changed from brittle intergranular fracture (S3), to cleavage fracture (S4) and final ductile fracture with dimples (S5 – S7). Due to the adverse effects of a high oxygen content (0.406 wt%) in the as-received Ti powder, the average tensile elongations of sintered Ti slices (S5-S7) was around 6% with the highest at about 10%. However, this work shows that for slices manufactured from within the interior of the sample there was no impurity pick-up during the sintering process in argon in the graphite furnace. It is believed that if using feedstock powders with lower impurity levels, the ductility can achieve desired levels comparable with ASTM standards.



## **6. EFFECT OF RESIDUAL CHLORIDE IMPURITIES ON COMMERCIALY PURE TITANIUM SINTERED IN A GRAPHITE FURNACE**

An investigation of residual chloride impurities was carried out on as-received HDH titanium powders as described in Chapter 4. It was found that jig-saw like magnesium chlorides were present on the surface of titanium particles. However, there is no work to study the chloride impurities on titanium sintering although it has been demonstrated that released hydrogen chloride gas and gaseous titanium chlorides during the decomposition process of hydrated magnesium chlorides may affect titanium sintering process adversely in Chapter 4. In addition, in Chapter 5 the same titanium powders were sintered in an argon atmosphere in a graphite furnace to study the effect of contaminants including carbon from the furnace and oxygen and nitrogen originating from the atmosphere on microstructural evolution and mechanical properties of sintered titanium specimens. However, there is no work to study the effect of chlorides impurities identified in Chapter 4 on titanium argon-atmosphere sintering in the graphite furnace demonstrated in Chapter 5. This chapter would specifically deal with this work.

### **6.1 Introduction**

The detrimental effects of chloride impurities on titanium sintering have been highlighted in Section 2.4.4 and Chapter 4. In order to overcome this problem the Cl content is required to be <0.005 wt% [5]. The vapour pressure of Cl and chlorides can be large during sintering at high temperatures, which inhibits densification [71]. Jackson et al. proposed a mechanism to explain the correlation between porosity and residual sodium chloride [70]. The chlorine vapour that results from the dissociation of sodium chloride reacts with titanium walls and produces high-

vapour-pressure  $\text{TiCl}_2$ ,  $\text{TiCl}_3$ ,  $\text{TiCl}_4$  at high temperature which can substantially inhibit pore closure [70]. In Section 2.4.4, although Fan et al. [67] investigated the effect of chloride in a Ti-6Al-4V and a titanium metal matrix composite and claimed the presence of chlorides causes grain refinement, other work on the effect of chlorides points to an agreement that the chlorides cause the formation of pores [71]. Moreover, the pores caused by dissociation of chloride cannot be removed by simple sintering or following cold/hot working, which would lower the fatigue limit [2, 6, 68-71].

In Section 2.4.4, it was described how there are currently two potential approaches to solve the chlorine-related issue: using extra-low chloride titanium powders[5, 6] associated with high cost, and applying effective chlorine scavengers such as the addition of 0.05 wt%  $\text{Y}_2\text{O}_3$  [65], 0.6 wt% yttrium hydride ( $\text{YH}_2$ ) [123] or  $\leq 0.5$  wt% cerium silicide ( $\text{CeSi}_2$ ) [72] into the powder. It is claimed that the addition of Ce has the capability to realise Cl scavenging and microstructural refinement and raise tensile ductility [72].

Since it is mentioned in Section 2.4.4 that limited works were carried out on the effect of magnesium chlorides originating from the mainstream sponge process — Kroll process and in chapter 4 the deliquescence of  $\text{MgCl}_2$  makes the dissociation situation different from the sodium chloride dissociation process, the aim of this work was to study the effect of the residual hydrated magnesium chloride on titanium powder sintering under an argon atmosphere in a graphite furnace.

## 6.2 Experimental

Both C.P. HDH titanium powder and pre-alloyed HDH Ti-6Al-4V powder were supplied by Xi'an Lilin Ltd, China with particle size less than  $75 \mu\text{m}$  (-200mesh). As was shown in chapter 4,

residual chloride impurities were identified in as-received HDH Kroll-process titanium powders, and pre-alloyed Ti-6Al-4V here is regarded as chlorine free for comparison.

The powders were pressed uniaxially under a compaction pressure of  $400 \pm 50$  MPa into cylindrical disc samples 12 mm in diameter and 5 to 8 mm thick. The compacts were then sintered in atmosphere at three different temperatures (1100, 1250 and 1400 °C) with two different holding times (4 and 6 hours) in the graphite furnace described in Section 3.2.

The microstructural surface morphologies of as-received powders and sintered specimens were characterized using ESEM coupled with the semi-quantitative compositional determination with EDS as described in Section 3.5. The interstitial contents were measured via the determination method described in Section 3.6. The phase constituents and metallographic observation were evaluated as described in Section 3.3 and Section 3.4. Vickers hardness was measured on the cross-section of sintered Ti after fine polishing under a 1 Kg load force with a holding time of 15 seconds.

## 6.3 Results

### 6.3.1 Characterization of as-received Ti and Ti-6Al-4V powders

Figure 6-1 shows scanning electron micrographs of the as-received Ti and Ti-6Al-4V powders, which were typically of irregular and angular particle shape.

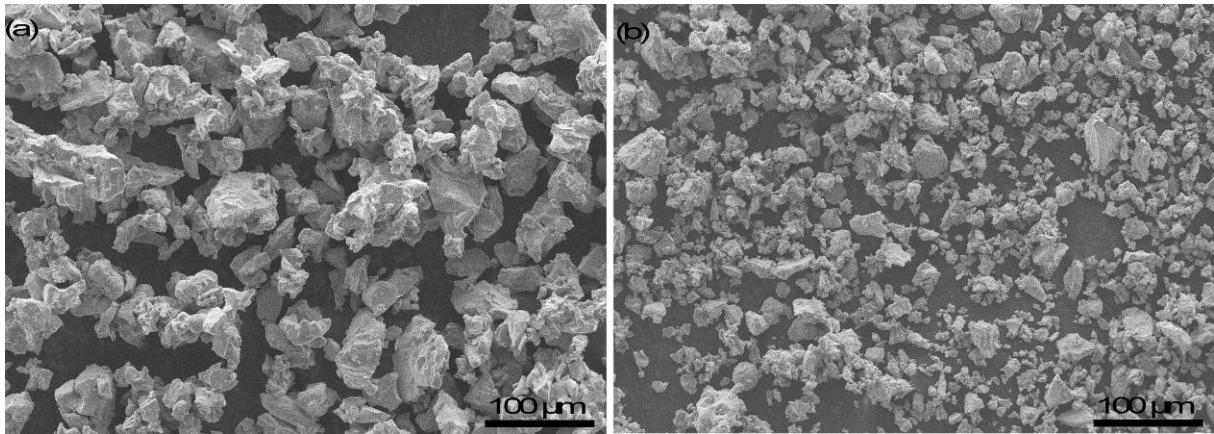


Figure 6-1: Micrographs of -200 mesh (a) Ti powder and (b) Ti-6Al-4V alloy powder [152]

The particle size is also in accordance with nominal size -200mesh ( $\leq 75 \mu\text{m}$ ). The impurity contents are shown in Table 6-1. The usage of pre-alloyed Ti-6Al-4V powders with high impurity contents powders is required by the funding body to study its sintering behaviour.

Table 6-1: C, H, O, N, Mg, Cl contents determined in as-received powders

Impurities	C (wt. %)	H (wt. %)	O (wt. %)	N (wt. %)	Mg (wt%)	Cl (wt%)
Ti	0.047	0.002	0.406	0.0067	0.0036	< 0.05
Ti-6Al-4V	0.27	0.002	0.42	0.17	None (nominal)	

Further phase determination of as-received titanium and Ti-6Al-4V powders is presented in Figure 6-2.

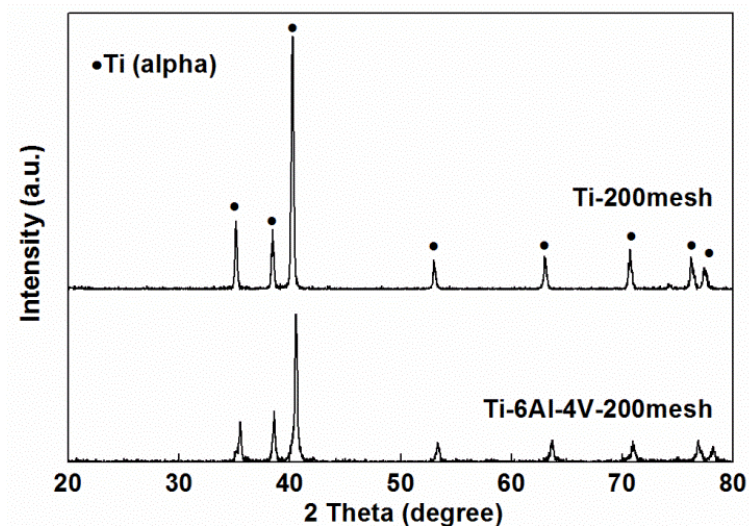


Figure 6-2: XRD patterns of as-received powders

For both c.p. Ti and pre-alloyed Ti-6Al-4V, all peaks in the XRD patterns are ascribed to alpha titanium referred as JCPDS # 44-1294 with no additional phases presented. As with the phase determination presented in Figure 4-1, there was no obvious evidence demonstrating the appearance of magnesium-related or chlorine-related peaks probably because the amount of residual chloride in powders is low.

### 6.3.2 Surface microstructural observations

In comparison with the surface of pre-alloyed Ti-6Al-4V powders sintered in the graphite furnace, interesting phenomenon was observed on the surface of sintered titanium specimens. As was mentioned in Section 5.3, the surface of titanium specimens were contaminated when sintering was carried out in the graphite furnace at the sintering temperature of 1250 °C with a holding time of 4 hours. A close-up SEM observation was made of the contaminated surfaces and the micrographs are shown in Figure 6-3.

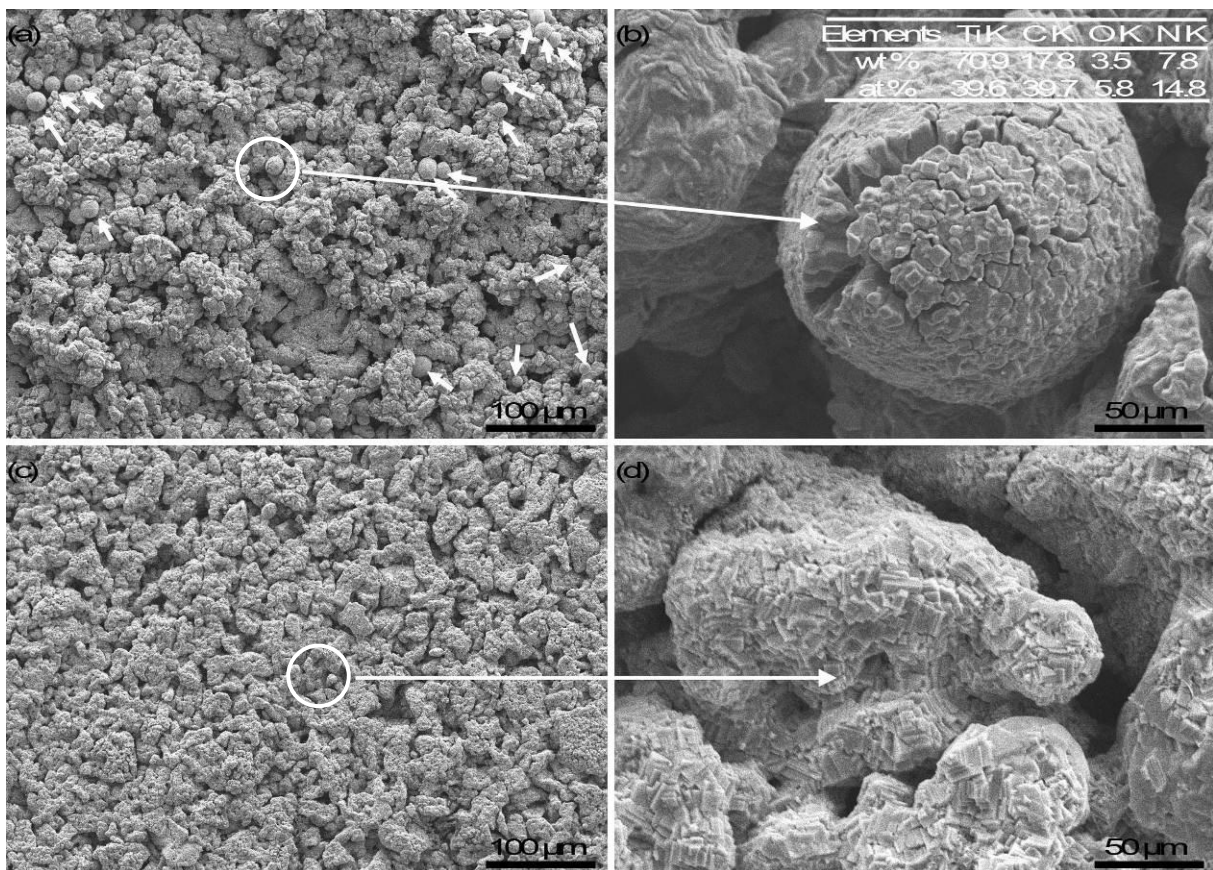
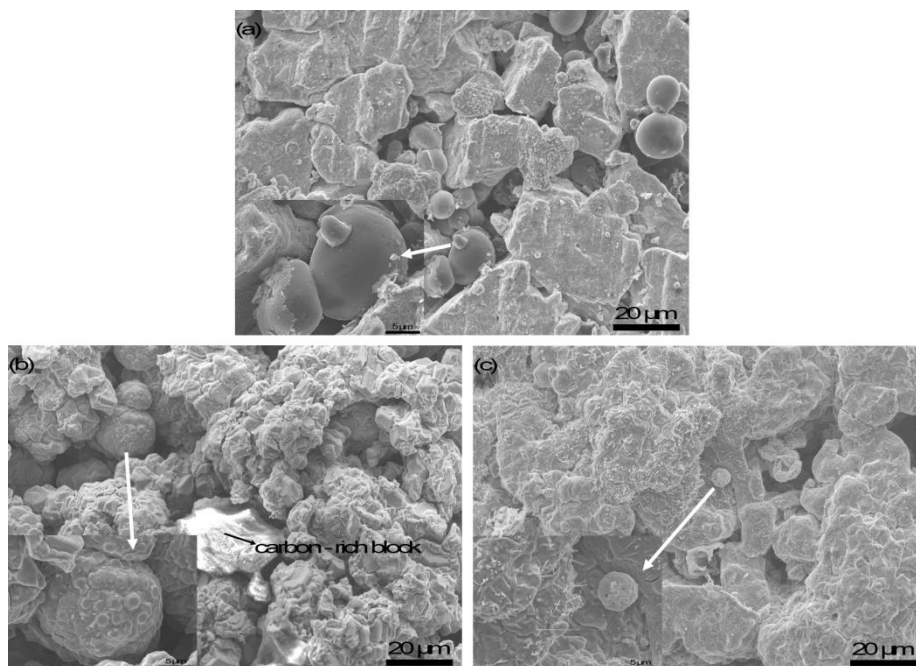


Figure 6-3: Micrographs of the sintered surfaces of Ti (a, b) and Ti-6Al-4V (c and d). Both samples were sintered at a temperature of 1250 °C for 6 hours[152]

Some spheres were found on the surface of sintered c.p. titanium (arrows in Figure 6-3a). Figure 6-3(b) shows such a cracked sphere with a high carbon concentration and small amount of oxygen and nitrogen (EDS results are included in Figure 6-3b). In addition, considering the phase of the surface of as-sintered Ti at the temperature of 1250 °C illustrated in Section 5.3.4, accordingly these spheres are suggested to be Ti(CNO). In contrast, these spherical particles were not found on the sintered surface of the pre-alloyed Ti-6Al-4V powder sample (Figure 6-3c and Figure 6-3d). Considering the main difference between elemental HDH titanium powder and HDH alloy powder, It is considered that the presence of the spheres on the sintered surface of elemental Ti powder compacts is related to the presence of residual chlorine in the starting

powder. The HDH titanium is produced from the Kroll-processed titanium sponges, and these sponges commonly contain chlorine impurities. On the other hand, the HDH Ti-6Al-4V alloy powder is produced by hydrogenating Ti-6Al-4V chips that are generally collected from machining wrought Ti-6Al-4V or similar alloy rods. More spheres were found on the surface of sintered Ti at varied sintered conditions illustrated in Figure 6-4.



*Figure 6-4: Spheres on the surface of sintered Ti at a) 1100 °C, 4 hours; b) 1250 °C, 4 hours; c) 1400 °C, 4 hours*

Figure 6-4 indicates that the spheres can exist on the surface of sintered Ti from low sintering temperature (1100 °C) to high sintering temperature (1400 °C). The size and the number of the spheres were both reduced with increasing temperature. It is perhaps because of Ostwald ripening resulting in smaller particles adhering on the surface of large particles and finally disappearance.

Corresponding semi-quantitative content determination has been carried out using EDS shown in Table 6-2.

*Table 6-2: Semi-quantitative testing contents of spheres on the surface of Ti specimens sintered at varied conditions*

Sintering Conditions	Titanium (at %)	Carbon (at %)	O, N and other Elements
1100 °C, 4 hours	4.99	90.55	Balance
1250 °C, 4 hours	54.44	34.14	Balance
1400 °C, 4 hours	36.95	38.21	Balance

EDS analysis revealed the presence of mainly carbon and titanium with oxygen and nitrogen, suggesting again the formation of titanium oxycarbonitrides. Further observation indicates the presence of hollow spheres on the surface of sintered titanium.

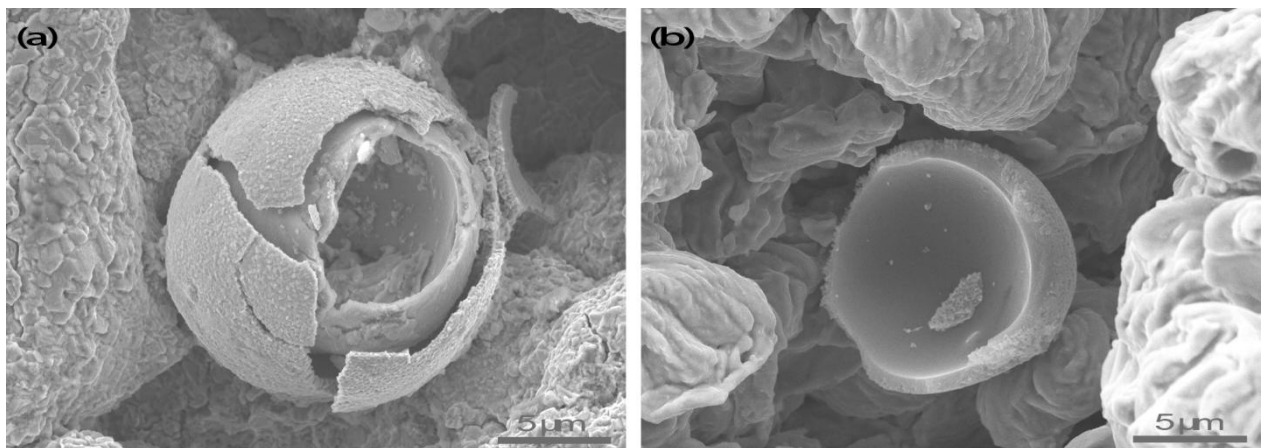


*Figure 6-5: Broken spheres on the surface of Ti specimens sintered at a) 1100 °C, 6 hours; b) 1250 °C, 4 hours*



Interestingly, some broken spheres revealed the inside of the spheres to be hollow as shown in Figure 6-5(a) at a sintering temperature of 1100 °C for 6 hours and in Figure 6-5(b) at a sintering temperature of 1250 °C holding for 4 hours. Further observation demonstrates these hollow spherical particles were also present beneath the surface in Figure 6-6.

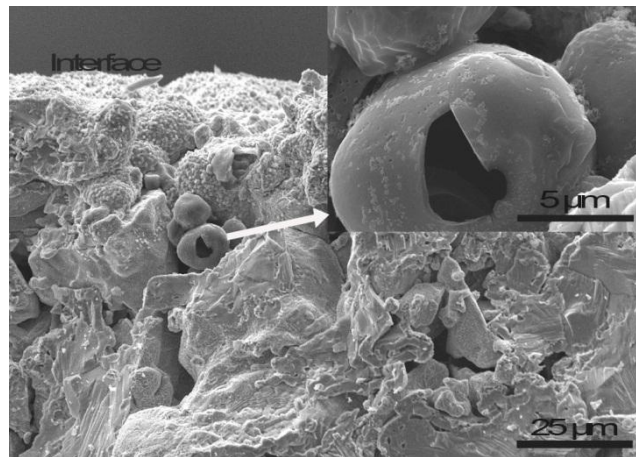


*Figure 6-6: Subsurface micrograph morphology of Ti specimens sintered at 1100 °C holding for 4 hours*

The porous surface and subsurface structure would definitely decrease the overall densification especially the subsurface hollow spheres which makes defects inside the specimens. It is thus predicted that such hollow structures would decrease the mechanical property performance.

### 6.3.3 Metallography and microhardness of the bulk sintered specimens

Metallographic observation of the cross sections of Ti samples sintered for 4 hours at 1100 °C and 1400 °C is shown in Figure 6-7.

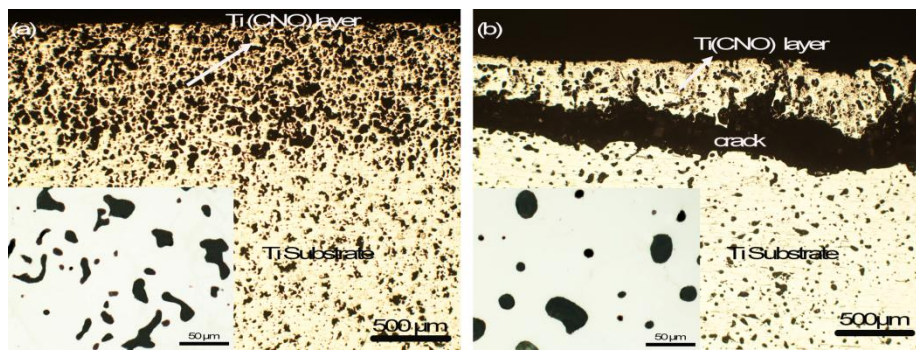


*Figure 6-7: Macrographs of Cross-section of sintered specimens at different sintering conditions:  
a) 1100 °C, 4 hours and b) 1400 °C, 4 hours*

It is clear that in both cases a contamination scale was formed during sintering. At a sintering temperature of 1100 °C the interface between the contamination layer and substrate titanium is clear but the bonding was still intact. Pores observed in the interior of the sample were not spherical and had an average size of about 50  $\mu\text{m}$ , and the shape of these pores indicates it is in the early stages of densification having only particle rearrangement and some neck formation. On the other hand, at a relatively high sintering temperature (1400 °C), the contamination scale was spalled and peeled off. Spherical pores, typically 10-50 microns in size, were observed in this sample at high magnification. It is considered that the evaporation of chloride impurities should be partly responsible for the porous cross-sections.

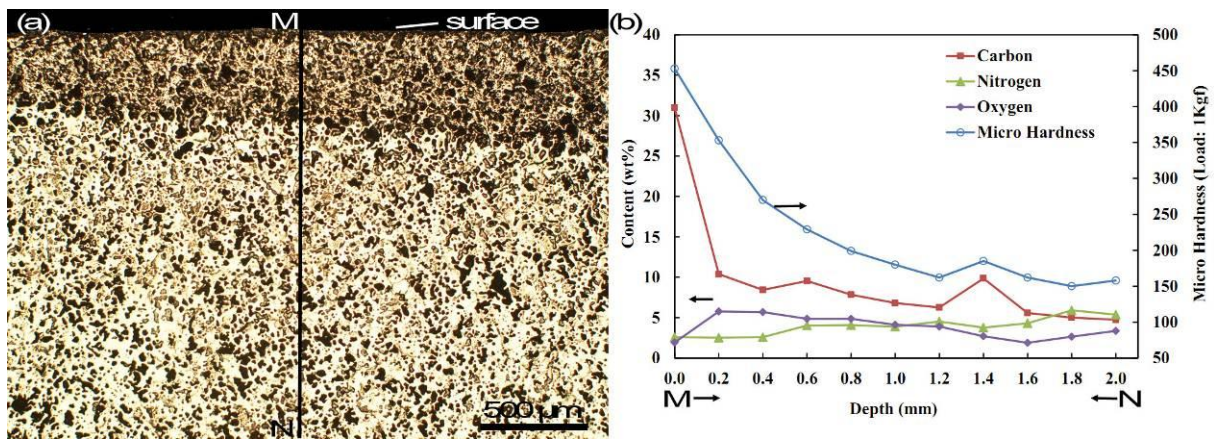


Figure 6-8: Macrograph of cross section (a) and corresponding EDS data and microhardness (b) of the sintered titanium (1100 °C, 6 hours)[152]

Cross sectional macrograph of the sintered titanium at 1100 °C with a holding time of 6 hours is presented in Figure 6-8(a). There was a scale layer 400 - 500 μm thick, different from the interior. Figure 6-8(b) shows the results obtained by energy dispersive spectrometry (EDS) analysis along the line “MN” (in Figure 6-8a ‘M’ indicates the outermost surface while ‘N’ indicates the centre of the sample). Semi-quantitative EDS analysis clearly shows a high carbon concentration of 30 wt% at the sample surface. Vickers hardness measured under a load of 1kgf follows the same trend as the carbon concentration profile. The hardness of 450 Hv at the surface decreases to 150 Hv for the sample interior. The high hardness on the surface is probably due to the formation of compounds and/or solid solution between contaminants and titanium [102, 154]. This is also in accordance with the mechanical property observation demonstrated in chapter 5.

## 6.4 Discussion

Previous reports [67, 70] and chapter 4 show that the decomposed products of residual chloride in the starting powders can further react with the surrounding titanium, producing gaseous titanium

chlorides ( $\text{TiCl}_4$ ,  $\text{TiCl}_3$  or  $\text{TiCl}_2$ ) at high temperature during sintering. Meanwhile, gaseous carbon atoms are likely released from the graphite heating element of the furnace, as a result of high temperature and extremely low carbon potential in the furnace [155] and/or through the complicated reactions [56]. The evaporated carbon atoms react with the gaseous titanium atoms that are derived from the decomposed titanium chloride, along with the residual nitrogen and oxygen, forming titanium oxycarbonitride. These titanium oxycarbonitrides are generally in the form of spherical particles as a result of gas-to-solid condensation. The HDH Ti-6Al-4V powders do not contain chloride impurity, and as a result, the carbon atoms evaporated from the heating elements simply condense on the surface or from the disproportionation reaction of carbon monoxide described in Section 7.4 and to a much lesser extent may diffuse into titanium alloy substrate. However in this case spherical particles are not able to form on the surface of sintered Ti-6Al-4V. The detailed sphere formation mechanism is proposed in Figure 6-9.

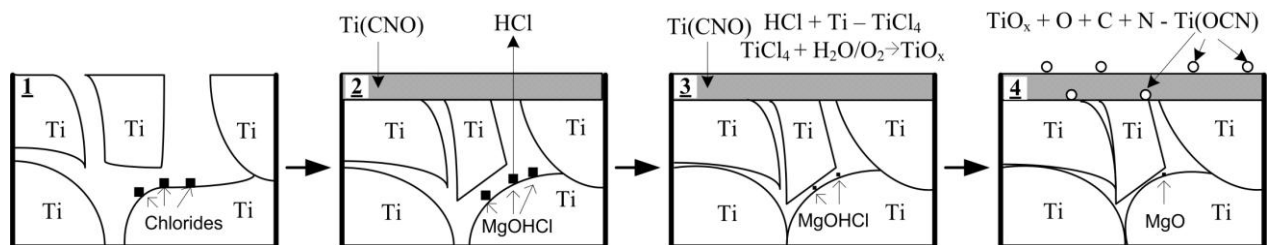


Figure 6-9: Process modelling of the effect of residual chlorides on titanium sintering

It is already known chlorides exist deep in HDH titanium powders which cannot be removed as presented in Figure 6-9(1). These magnesium chlorides would decompose during heating into  $\text{MgOHCl}$  and gaseous  $\text{HCl}$  as shown in Figure 6-9(2). Gaseous  $\text{HCl}$  can react with titanium and form titanium chlorides. This is consistent with the Thermogravimetric analysis carried out on the starting powders and described in Section 4.3. However, titanium chlorides could react with

released gaseous  $H_2O$  molecules [156] and/or with the oxygen [157] and form nano-structured titanium oxides presented in Figure 6-9(3). These formed titanium oxides can further react with the atmosphere (carbon, nitrogen, oxygen) and form the spherical titanium oxycarbonitride in Figure 6-9(4). The formation of spheres is due to the lowest surface free energy state. In the process, it would produce gaseous hydrogen chloride and titanium chloride both detrimental to the final densification. Since the nano-structured oxides would react with gases in the atmosphere, the hollow structure could be formed due to the diffusion speed differential between Ti and interstitial contents (C, N, O) [158-160].

It is logical that the presence of a porous contaminated outer layer would affect the overall sintering densification. The relative sintered densities are presented in Figure 6-10. It is found that under an identical sintering condition, the Ti-6Al-4V samples had a higher sintered density than that of Ti, even though the relative green density of titanium was higher than that of pre-alloyed Ti-6Al-4V. Theoretically the compacts with higher green density might be expected to have higher sintered density and the fact that this was not the case is thought to be related to the effect of the chloride impurities.

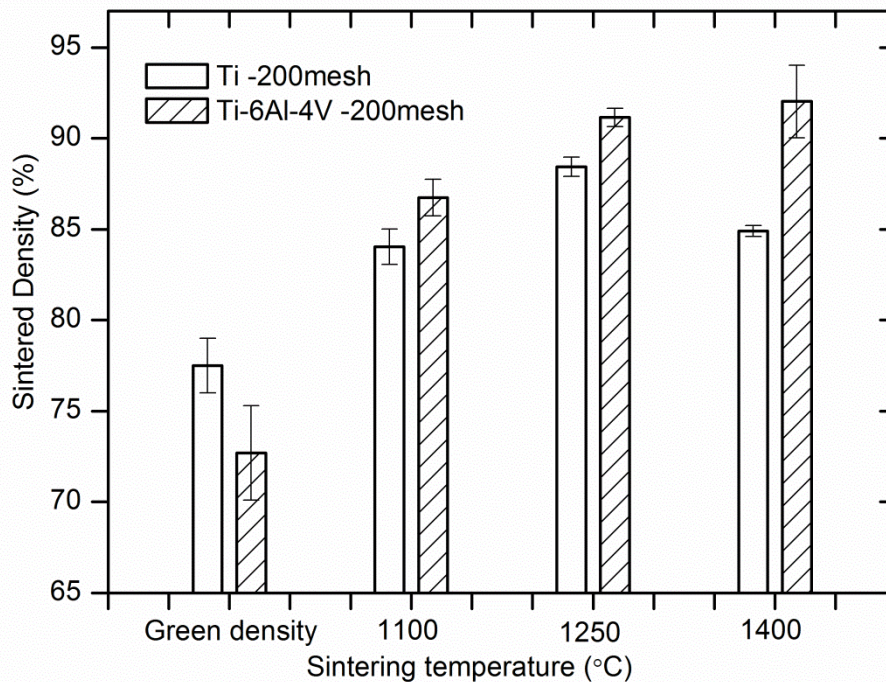


Figure 6-10: Relative density of compacts and sintered specimens under different sintering temperatures for C.P. Ti and pre-alloyed Ti-6Al-4V. All samples were sintered for 6 hours

In addition, the sintered density of pre-alloyed Ti-6Al-4V increased with sintering temperature, but this was not the case for c.p. Ti powder where the sintered density of Ti was found to be reduced when the samples were sintered at a higher temperature of 1400 °C.

## 6.5 Conclusions

When the titanium and/or Ti alloy powder compacts are sintered in a graphite furnace, a fairly thick scale layer is formed, being Ti(CNO). For the case of HDH c.p. titanium powder compacts, spherical hollow particles of Ti(CNO) were observed on the surfaces of sintered Ti samples, but not on the sintered surface of pre-alloyed Ti-6Al-4V which is regarded as chlorine free. The formation of spherical hollow particles is postulated to be caused by the reaction between the gaseous carbon and gaseous titanium atoms decomposed from titanium chlorides. Therefore the presence of

chlorides is detrimental to the final sintering densification because of the formation of these hollow spheres. Microhardness was closely related to the contaminant contents; therefore microhardness may not be a good indicator of sintering densification. It is suggested again that the use of getting agents is essential if sintering is undertaken in a graphite furnace. This work will be presented in chapter 7.

## **7. DEVELOPMENT OF A CLEAN SINTERING ENVIRONMENT IN A GRAPHITE FURNACE**

As demonstrated in chapter 5 and chapter 6, noticeable contamination occurred on the surface of titanium and Ti-6Al-4V compacts sintered in a graphite furnace, and therefore, corresponding mechanical properties are extremely low for those contaminated slices. In order to obtain sintered bodies with improved properties, this chapter describes the results of utilising different contamination-reduction solutions. In addition, the effect of sintering atmosphere is also discussed in this chapter.

### **7.1 Introduction**

As described in previous chapters (chapter 5 and chapter 6), the surface of titanium compacts sintered in argon atmosphere in the graphite furnace was contaminated when exposed directly to the furnace atmosphere. In general, there are three contaminant sources appearing in titanium sintering. One is from the original titanium or alloys powders; with a target to realise desired densification and mechanical properties the powders to be utilised in sintering require low-content contaminants especially interstitials such as oxygen and nitrogen as well as good storage conditions; the second originates from the furnace atmosphere such as contaminants coming from the protective gas and/or low vacuum level; thirdly, the selection of proper racking materials is the last concern considering the high reactivity of titanium. Thus it is necessary, from a technological point of view, to seek suitable solutions to prevent the contamination. Molybdenum (Mo) is considered as a good racking material for titanium sintering due to its low solubility in titanium and its ability to retain strength at sintering temperatures [5], and BN crucibles are regarded as another good choice for racking materials of titanium sintering because of low



reactivity and high melting point [50]. The development of a contaminant getter may hold the key to solve the contamination from the furnace atmosphere [152].

Titanium powders are generally sintered under vacuum rather than in an atmosphere such as argon or helium so as to obtain high densification and superior mechanical properties [5]. Vacuum sintering with a pressure of the order of  $10^{-2}$  Pa or lower [99, 100, 161, 162] can effectively control the active reaction between titanium and interstitial impurities such as oxygen, nitrogen and carbon. Vacuum sintering can also remove detrimental volatiles such as chlorides existing in titanium sponges and help densification [2, 147]. However, vacuum sintering is a batch process and has high capital equipment requirement. Possible continuous mass production is suggested to be realized by atmosphere sintering in a continuous industry furnace so as to decrease the production cost [2, 5]. In order to offer reliable knowledge base for titanium sintering in an atmosphere such as argon, it is necessary to study the effect of sintering atmosphere and compare with sintering in vacuum.

Limberg et al. [9] studied the influence of sintering atmosphere on sintering behaviour of Ti-45Al-5Nb-0.2B-0.2C (at. %) through altering the argon atmosphere pressure (10, 30 and 80 kPa) in comparison with sintering under vacuum ( $10^{-3}$  Pa). The literature indicates that the residual porosity of sintered specimens increased proportionally with applied argon pressure to 1.1% at the maximum pressure (80 kPa) but no other pronounced microstructural difference such as grain size was observed due to the varied sintering atmosphere [9]. It was shown that the pressure of the sintering atmosphere had no obvious effect on tensile properties and all specimens exhibited similar ultimate tensile strength (around 630 MPa) and elongation (0.15-0.19 %) [9].

This chapter describes different contamination-reduction solutions and studies the effect of sintering atmosphere on sintered titanium and Ti-6Al-4V.

## 7.2 Experimental

HDH commercially pure titanium powders and pre-alloyed Ti-6Al-4V were pressed into “dog-bone” morphology with a length of 35 mm under a compaction pressure of 500 MPa. The phase constituents and surface morphologies can be seen in Section 6.3.1 for both Ti and Ti-6Al-4V powders. Vacuum sintering was conducted at a pressure of 0.1-0.01 Pa inside the graphite furnace, and atmosphere sintering was carried out under vacuum to a temperature (850 °C) with a heating rate of 5 °C min<sup>-1</sup>, followed by back filling the furnace with argon gas (purity 99.99%) to a pressure of 1.1 atm. The pressure was maintained until the end of sintering. Compacts were sintered at a temperature of 1250 °C with a holding time of 4 hours. Detailed furnace heating zone design was shown in Figure 3-2. After sintering, these “dog-bones” were further machined to suit the testing standard ISO 2892-1:2009 for mechanical properties. Different contamination reduction solutions can be seen in Figure 7-1 utilised in both atmosphere sintering and vacuum sintering.

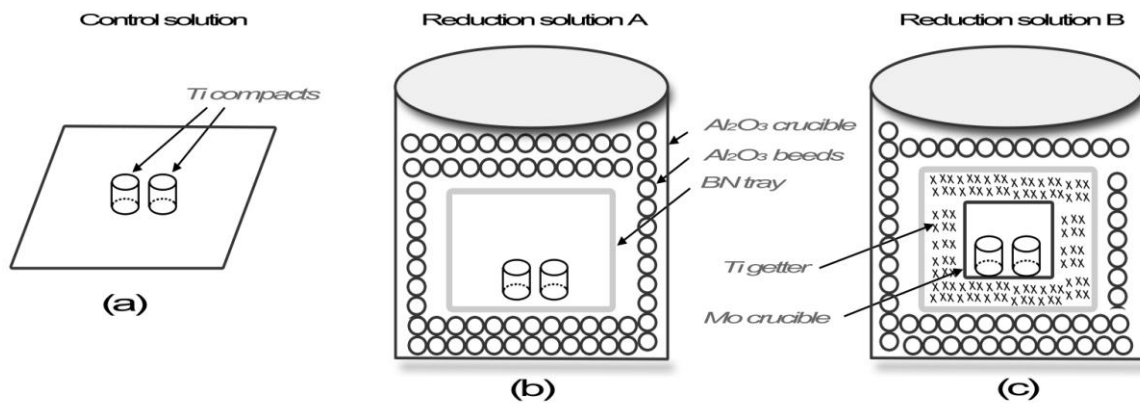
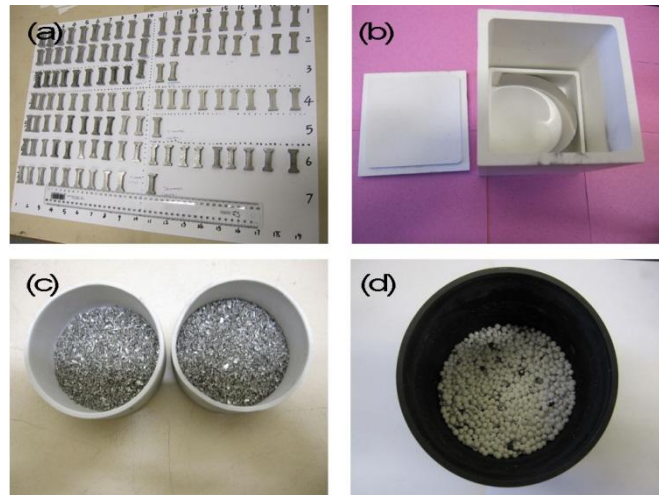


Figure 7-1: Different solutions for titanium sintered in a graphite furnace: a) control solution: exposed directly to the furnace atmosphere on a BN plate; b) solution A: placed in a BN tray wrapped by Al<sub>2</sub>O<sub>3</sub> beads in a large-sized Al<sub>2</sub>O<sub>3</sub> crucible; c) solution B: placed in a Mo crucible wrapped by 1mm-diameter titanium particles served as contamination getter

Figure 7-1(a) demonstrates titanium compacts that were exposed directly to the furnace atmosphere on a BN plate without any protection. Commercially available BN trays were employed (Denki Kagaku Kogyo Co., Ltd., Japan grade BN-1000) in both solution A and solution B. They both are made of high purity BN (>99.5%) with a density of 1.6 g cm<sup>-3</sup>. In Figure 7-1(b) (contamination-reduction solution A), specimens were sintered in the BN tray surrounded with loosely packed alumina beads (dia=2 mm) with the target to physically separate possible carbon contamination originating from the graphite furnace from titanium compacts. No chemical reaction with the beads is expected in the contamination reduction process. The whole setup was placed into a large-sized alumina crucible. Based on solution A, the reduction solution B utilised titanium particles as a contamination getter surrounding the Mo tray where the compacts were placed as seen in Figure 7-1(c). Detailed materials applied in the experimental setup can be seen in Figure 7-2.



*Figure 7-2: Materials applied in the experimental setup: a) compacts; b) BN tray; c) titanium contamination getter; d) Al<sub>2</sub>O<sub>3</sub> beads*

The sintered density was measured according to the Archimedes method described in ASTM B962-08 standard. An environmental scanning electron microscope (ESEM) (Quanta 200F, FEI) was used to observe the microstructural morphology of the sintered specimens.

## **7.3 Results**

### **7.3.1 Density measurement**

The sintered densities and corresponding densification levels are illustrated in Figure 7-3 for Ti and pre-alloyed Ti-6Al-4V compacts sintered at a temperature of 1250 °C in vacuum with a holding time of 4 hours. The calculation of densification level  $\varphi$  can be referred according to Equation 5-1 shown in Section 5.3.1.

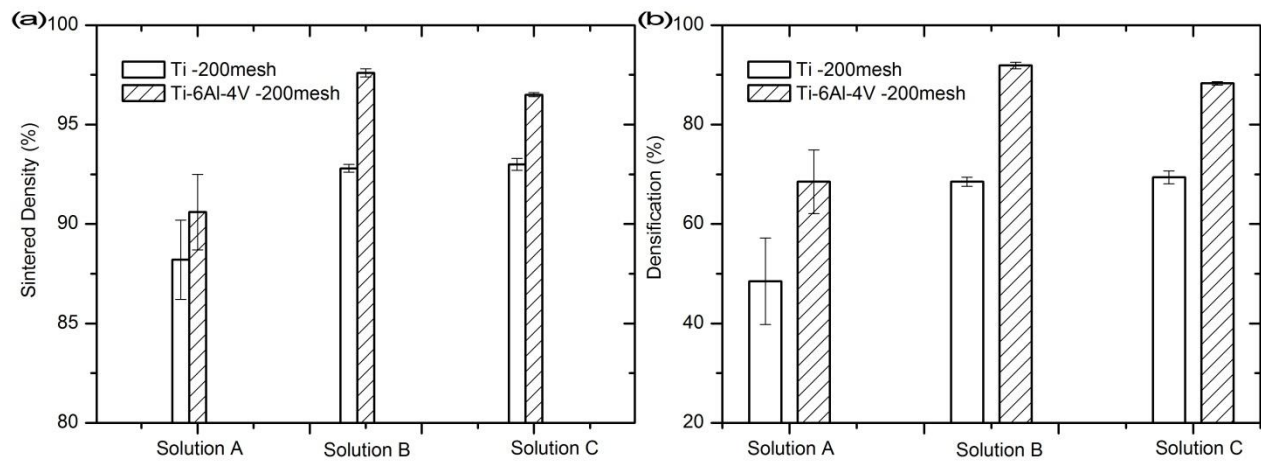


Figure 7-3: (a) sintered densities and (b) densification levels of Ti and Ti-6Al-4V specimens sintered under different protection solutions at the temperature of 1250 °C in vacuum with a holding time of 4 hours

It can be seen that specimens sintered with contamination reduction solution A and B have much higher sintered densities and densification levels than compacts with control solution for both C.P. Ti and pre-alloyed Ti-6Al-4V. In addition, this figure also clearly shows that the density and densification of pre-alloyed Ti-6Al-4V was higher than sintered Ti specimens. This is in accordance with the observation in chapter 6 although the powders were sintered in different sintering atmospheres (vacuum here in comparison with atmosphere sintering in chapter 6). The difference in densification between the C.P. Ti and the Ti-6Al-4V alloy is considered due to the evaporation of chloride impurities in C.P. titanium powders, which was discussed in chapter 4 and chapter 6. The sintered densities of C.P. titanium compacts sintered at different sintering atmospheres are presented in Table 7-1.

*Table 7-1: Relative sintered densities of C.P. Ti compacts sintered at atmosphere and vacuum respectively at the sintering temperature of 1250 °C with a holding time of 4 hours*

	Sintered density under vacuum	Sintered density in atmosphere
Control solution	88.2 ± 2 %	91.4 ± 0.5 %
Reduction solution A	92.8 ± 0.2 %	94.1 ± 0.3 %

As is compatible with the density measurement shown in Figure 7-3, the sintered density of compacts with reduction solution A is about 4.5% higher in vacuum and around 2.7% higher in atmosphere when compared with specimens with control solution. However, interestingly the sintered density of specimens in vacuum was 1.3-3.2% lower than specimens sintered in atmosphere although theoretically specimens in vacuum should give higher sintered density due to the removal of trapped gas in compacts [13, 14].

### 7.3.2 As-sintered surface morphological observation

The surface morphologies of as-sintered samples are shown in Figure 7-4 for sintering in vacuum at a temperature of 1250 °C with a holding time of 4 hours.



*Figure 7-4: As-sintered surface morphologies of Ti specimens sintered under vacuum using different contamination-reduction solutions*

The titanium compacts exposed directly to the furnace atmosphere (control solution) had serious contamination and lost the original as-compacted specimen's shape. In contrast, the as-sintered surfaces of the specimens sintered in two reduction solutions show metallic colour with no obvious surface scale and with good shape retention. The samples sintered with contamination-reduction solution A and solution B had similar densities of 92-93% whilst the density of the samples directly exposed to the furnace atmosphere was only around 88.2%.

These results show that the way in which the samples are contained within the furnace has a significant impact on their final density (and therefore properties), and the densities can be raised with appropriate protection. Further surface microstructure observation and EDS analysis was conducted on Ti specimens sintered with contamination-reduction solution A in vacuum presented in Figure 7-5.

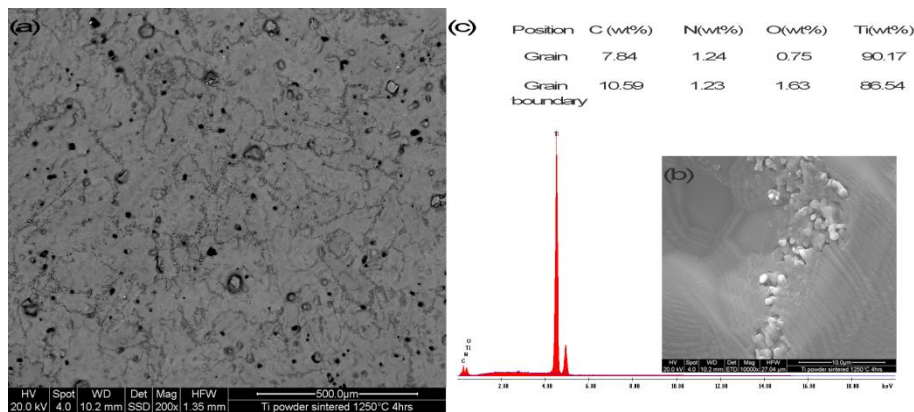


Figure 7-5: as-sintered surface of Ti specimens sintered with contamination-reduction solution A (a) and high magnification picture of grain boundary (b) and corresponding EDS spectrum (c)

In backscattered electron mode (Figure 7-5a) a clear distinction can be made between the grains and the grain boundaries, and the secondary electron image in Figure 7-5b shows that the width of the grain boundary is 1-5  $\mu\text{m}$ . An EDS spectrum from the grain boundary is shown in Figure 7-5c along with semi-quantitative compositional analysis of the grains and grain boundary regions.

The titanium content was high in both positions, which supports the clean as-sintered surface of specimens with contamination-reduction solution A shown in Figure 7-4. The overall content of interstitial elements (carbon, nitrogen and oxygen) was higher in the grain boundary regions (~13.5 wt%) compared to the grain (~10 wt%), mainly attributed to increment of carbon and oxygen content in the boundary region. Among these three interstitials, carbon has the highest content in both positions possibly due to the sintering in the graphite furnace. It has to be noted that the accurate interstitial contents cannot be given by EDS determination. However, the results



suggest that even sintering with contamination-reduction solution A is not sufficient to fully remove the contamination from the graphite furnace.

### 7.3.3 Macrostructural cross-section observation

The observation presented in Figure 7-4 of as-sintered titanium surfaces under different contamination-reduction solutions indicates that the specimens sintered with contamination reduction solution A and B have no clear contaminated scales in comparison with heavily contaminated specimens sintered with control solution. Further macrostructural cross-section studies were carried out and can be seen in Figure 7-6.

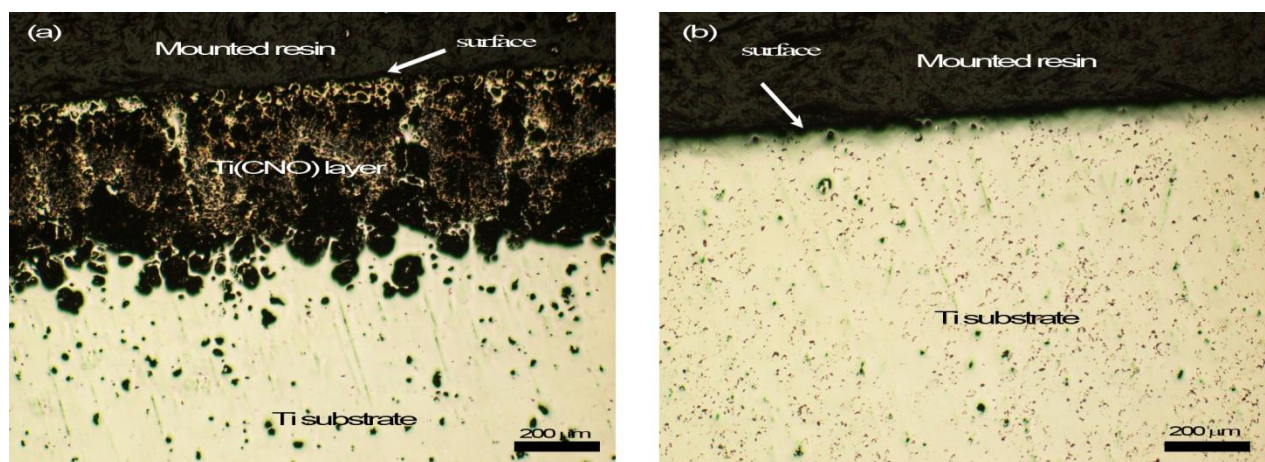


Figure 7-6: Macrostructural cross-section observations of titanium specimens sintered under vacuum with (a) control solution and (b) contamination reduction solution B

A thick contaminated layer existed on the surface of titanium specimens sintered with control solution, which is in accordance with the observation of the surface shown in Figure 7-4. In comparison, there was no contaminated scale on the surface of sintered Ti with contamination-

reduction B. This confirms again that contamination-reduction solution B has the capability to remove the contaminants including carbon, nitrogen and oxygen in the surface.

#### 7.3.4 Mechanical properties and fractural morphology

Since mechanical properties of sintered titanium are highly sensitive to the interstitial contents in as-sintered Ti [17, 163], the tensile properties can be a good indicator for the interstitial contamination. The results are shown in Table 7-2.

*Table 7-2: Tensile mechanical properties at varied contamination-reduction solutions and sintering atmospheres for titanium compacts sintered at the temperature of 1250 °C with a holding time of 4 hours*

Reduction solutions and sintering atmospheres	Tensile strength	0.2% Proof strength	Elongation	Young's modulus
Control solution, atmosphere	276.4 ± 8.55 MPa	—	0.31 ± 0.05 %	92.2 ± 17.8 GPa
Solution A, atmosphere	444.4 ± 56.2 MPa	412.4 ± 72.5 MPa	1.32 ± 0.62 %	96.4 ± 3.6 GPa
Solution A, vacuum	535 ± 66 MPa	305 ± 60 MPa	9.71 ± 0.47 %	95.8 ± 2.2 GPa

As illustrated in Table 7-2, the titanium specimens sintered in atmosphere with contamination-reduction A had higher tensile strength (444.4 MPa vs 276.4 MPa) and larger ductility (1.32 % vs 0.31 %) than specimens sintered with control solution. With the same contamination-reduction solution A, sintering in vacuum was able to give higher tensile mechanical properties especially the ductility (9.31 % vs 1.32 %) compared with compacts sintered in atmosphere. Young's moduli of all sintered titanium specimens were almost constant in the range of 90-100 GPa. Corresponding representative strain-strain curves are presented in Figure 7-7. True stress and

strain data ( $\sigma_T - \varepsilon_T$ ) are calculated from engineering values ( $\sigma - \varepsilon$ ), using the following well-known conversion formulae, valid for uniform deformation:

$$\sigma_T = \sigma(1 + \varepsilon) \quad (7-1)$$

$$\varepsilon_T = \ln(1 + \varepsilon) \quad (7-2)$$

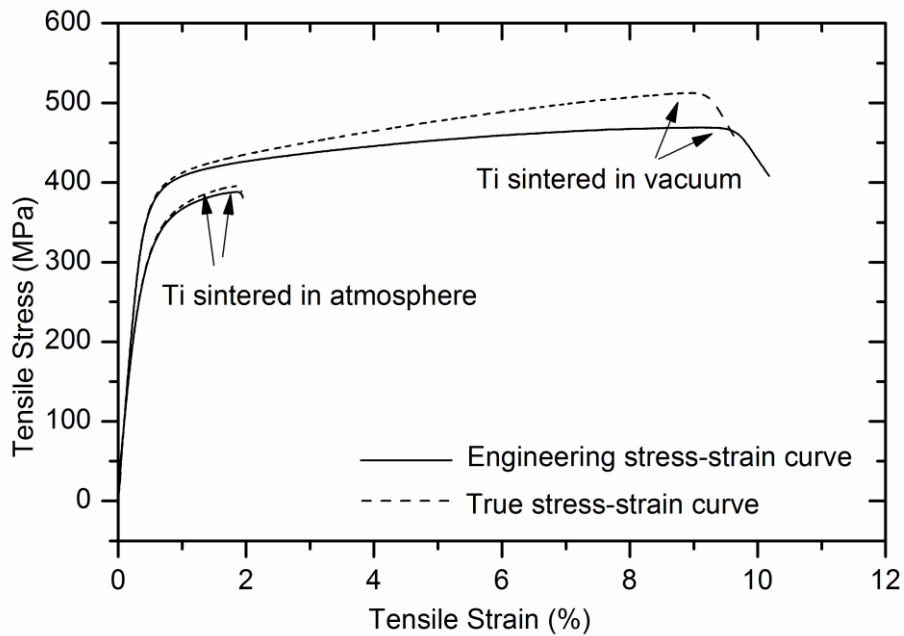
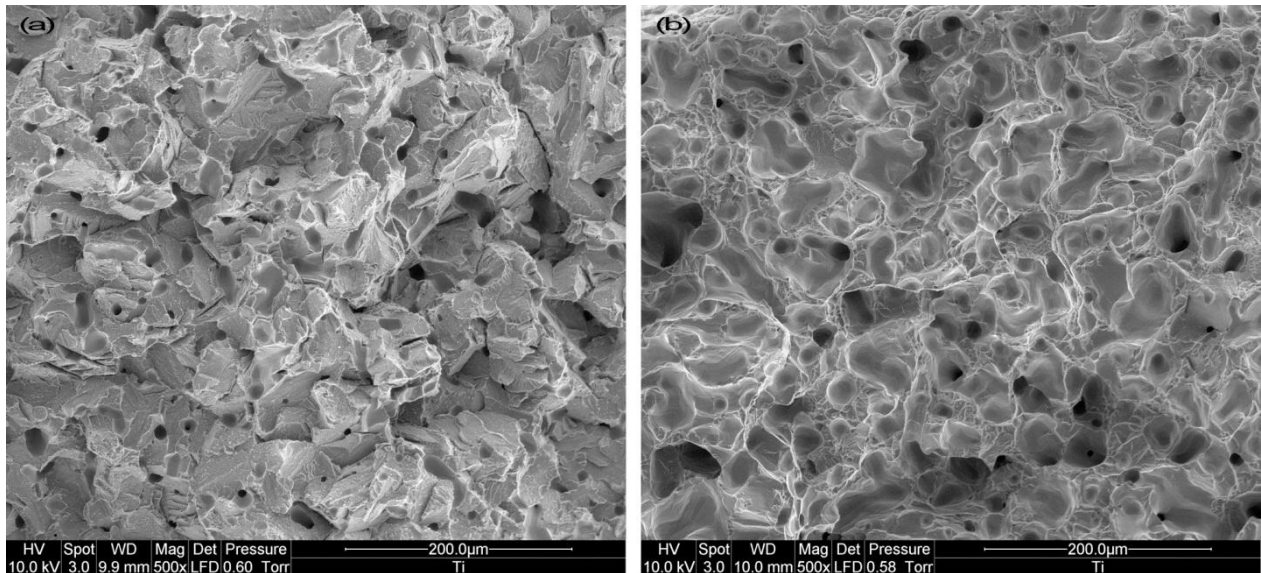


Figure 7-7: Representative engineering and true stress-strain curves for Ti specimens sintered at varied sintering atmospheres with the same contamination-reduction solution A

The tensile strength and ductility of titanium sintered in vacuum was higher than when sintered in argon atmosphere, and obviously the plastic deformation is much larger than elastic deformation for titanium compacts sintered under both vacuum and atmosphere. In addition, the true stress-strain was larger than the engineering stress-strain shown in Figure 7-7. Further the difference of

corresponding fracture surfaces of sintered specimens shown in Figure 7-7 are highlighted in Figure 7-8.



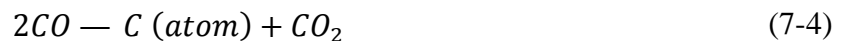
*Figure 7-8: Fractural surfaces at varied sintering atmospheres (a) atmosphere sintering and (b) vacuum sintering for sintered titanium using contamination-reduction solution A at the temperature of 1250 °C with a holding time of 4 hours*

Since the ductility of specimens sintered in vacuum was much higher than those sintered in atmosphere, apparent ductile deformation with dimples were observed on the fracture surface of specimens sintered under vacuum shown in Figure 7-8(b) in comparison with intergranular fracture observed in Figure 7-8(a).

## 7.4 Discussion

### 7.4.1 Origin of carbon source

As mentioned in the literature [56, 57, 164], titanium can be saturated by oxygen and carbon simultaneously and form a titanium carboxide compound surface, an interlayer of titanium solid solutions with carboxide formed at grain boundaries, and an interlayer of titanium solid solutions from the surface to the interior when titanium specimens were placed into graphite under vacuum or argon atmosphere. Importantly, Guryn et al [56] reported that the graphite (C) can react with oxygen and form carbon monoxide which would further decompose into carbon gaseous atoms and carbon dioxide on the surface of titanium substrate. These reactions are summarised into following reactions [56, 165]:



With the samples examples directly exposed to the furnace atmosphere (control solution), the carbon atoms would be able to react with titanium specimens without contact at high temperature in the form of gas and form titanium carbide. This indicates that oxygen gas has the ability to transport carbon to the saturated titanium surface [57]. This may explain why the contents of carbon and oxygen decrease from the surface to the interior as presented in Table 5-3 in chapter 5. This is evidently shown by the phase determination in Section 5.3.4 of as-sintered surface which indicates the phase (titanium oxycarbonitride) is a compound of titanium carbide, titanium monoxide and titanium nitride.

#### 7.4.2 Theoretical calculation of scale thickness based on Fick's second law

The theoretical thickness of this contaminated layer at the sintering temperature can be determined using a simplified model based on Fick's second law. This simplified analysis assumes that although the layer was identified as Ti(CNO) it is modelled as a layer of TiC since specimens were sintered in a graphite furnace with carbon potential and the solubility of carbon in Ti (<0.4 wt%) is lower than oxygen and nitrogen [55] which means it is much easier for carbon in titanium matrix to precipitate titanium carbide than oxygen and nitrogen. The thickness of the layer, assuming it is a single phase of TiC, can then be determined using the minimum and maximum solubility of C in TiC.

The variation with time of the interstitial content concentration is given by Fick's second law:

$$\frac{\partial C}{\partial t} = D_e \frac{\partial^2 C}{\partial x^2} \quad (7-5)$$

where  $C$  is the concentration of the solute atoms in the matrix,  $D_e$  is the diffusion coefficient of the solute atom in the matrix,  $t$  is the diffusion time and  $x$  is the distance in the direction of diffusion.  $D_e$  follows a Arrhenius relationship:

$$D_e = D_0 \exp(-Q/RT) \quad (7-6)$$

where  $D_0$  is the pre-exponential factor,  $Q$  is the activation energy,  $T$  is the absolute temperature and  $R$  is the gas constant ( $8.314 \text{ J mol}^{-1} \text{ K}^{-1}$ ). The diffusion coefficients of carbon in TiC,  $\alpha$ -Ti and pre-alloyed Ti-6Al-4V are available in the literature [166]:

$$D_C(\text{TiC}) = (4.8 \pm 0.3) \times 10^{-5} \times \exp[(-146000 \pm 4000)/RT] \text{ cm}^2\text{s}^{-1} \quad (7-7)$$

$$D_C(\alpha\text{-Ti}) = (6.4 \pm 0.2) \times 10^{-3} \times \exp[(-113000 \pm 3000)/RT] \text{ cm}^2\text{s}^{-1} \quad (7-8)$$

$$D_C(\text{Ti-6Al-4V}) = (18.5 \pm 0.5) \times 10^{-3} \times \exp[(-166000 \pm 2000)/RT] \text{ cm}^2\text{s}^{-1} \quad (7-9)$$

According to the Ti-C phase diagram [55, 167] shown in Figure 7-9, it can be calculated that the maximum carbon concentration in TiC at a temperature of 1250 °C is around 19.3 wt% and the minimum is about 12.5 wt%.

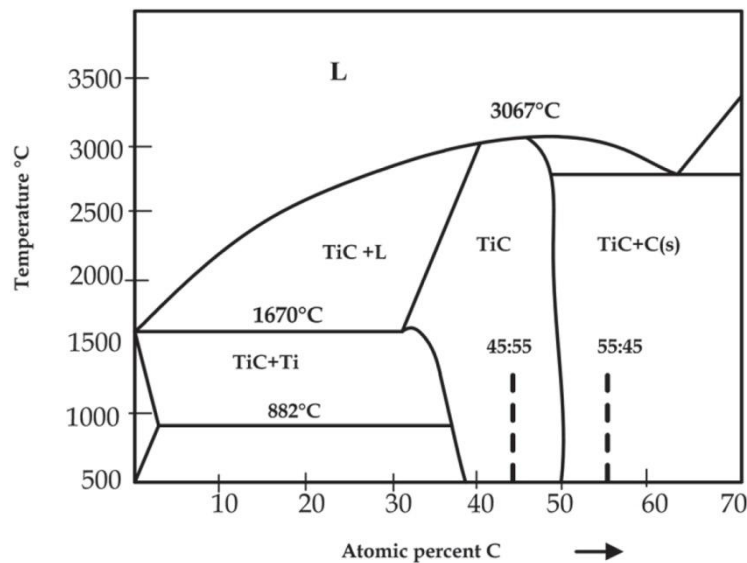


Figure 7-9: Phase diagram of titanium-carbon [167]

The thickness of the contaminated layer can be calculated based on following assumption:

The surface of the sample is saturated in carbon, ie that the composition at its outermost surface corresponds to the maximum solubility of carbon (19.3 wt%) in TiC and remains constant

throughout the holding period. In addition, the contaminated layer can block and/or absorb gaseous carbon atoms from the atmosphere, ie carbon can only diffuse by solid not by gaseous contact. In this case the increase in the thickness of the contaminated layer can be determined during the holding period of the sintering schedule using the solution to Fick's second law for a semi-infinite solid.

Considering boundary conditions for a semi-infinite solid:

$t = 0, C_{(x=0)} = C_s = 19.3 \text{ wt\%}$ , equal to the maximum carbon concentration in pure TiC;

$t > 0,$

$C_{(x=0)} = C_s,$

$C_{(x=\infty)} = C_0 = 0.4 \text{ wt\%}$ , corresponding to the maximum solubility of carbon in alpha titanium,

$C_{(x,t)} = 12.5 \text{ wt\%}$ , corresponding to the minimum carbon content in pure TiC.

$$C_{(x,t)} = C_s - (C_s - C_0) \operatorname{erf} \left( \frac{x}{2\sqrt{Dt}} \right) \quad (7-10)$$

where  $D$  is the diffusion coefficient of carbon in titanium carbide,  $t$  is the diffusion time (4 hours), and  $x$  is the diffusion distance. After replacing these values into Equation 7-10, the maximum thickness of the contaminated layer was calculated as being  $17.7 \mu\text{m}$ , which is much smaller than the thickness of surface contaminated layer  $300\text{-}500 \mu\text{m}$  presented in Figure 7-6.

This analysis was based on the assumption that the layer was a single phase TiC (ie using a minimum C concentration of 12.5%). However, the phase diagram demonstrates that TiC can co-exist with a solid solution of C in Ti from carbon concentrations as low as 0.4%. Taking into



consideration that the contaminated layer may actually contain both pure TiC and the Ti solid solution results in a calculated thickness of around 90  $\mu\text{m}$ . Whilst this is still below the measured thickness, the discrepancy may be explained in a number of ways. The samples are not 100% dense which means the diffusion of the C is probably faster than that described by the diffusion coefficients used in this analysis. Secondly, in the case of the mixed layer, the thickness was determined using the diffusion coefficient of C in TiC and probably underestimates the diffusion distance since the diffusion coefficient of C in Ti is higher. Indeed, recalculating the thickness using the diffusion coefficient of C in Ti showed that the thickness of the layer could be of the order of 3000  $\mu\text{m}$ . Finally, the calculation of thickness was carried out at the sintering temperature of 1250  $^{\circ}\text{C}$ . The phase diagram indicates that the solubility of C in Ti decreases with temperature so the thickness of the contaminated layer measured at room temperature would be expected to be larger schematically in Figure 7.10.

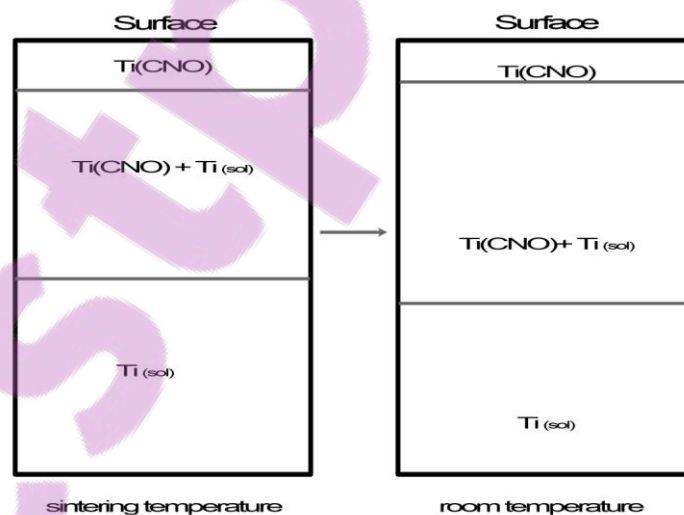


Figure 7-10: Schematic graph of different layers formed at sintering temperature and room temperature

Based on this analysis, then, it is suggested that the contaminated scale may consist of a layer of Ti(CNO) and a thick layer of Ti(CNO) + Ti (sol).

#### 7.4.3 Effect of contamination reduction solutions

The contaminated scale discussed above was only observed when the samples were exposed directly to the furnace environment, and not when the contamination-reduction solution A and B were employed. It is believed that with contamination reduction solution A, the alumina beads and BN crucible either prevent the interstitial elements from contacting the Ti surface and/or reduce the available contact area. This results in the increased sintered density and densification shown in Figure 7-3 and the tensile ductility presented in Table 7-2. Contamination reduction solution B, is believed to provide an additional potential as a contamination getter since the large-sized titanium particles can react with the interstitial contents prior to the contact with titanium compacts. This is evidently shown in Figure 7-6 which demonstrates that apparent contaminated layer was observed on the surface of specimens sintered with control solution but not seen with reduction solution B. For contamination reduction solutions A and B, since there is no contamination to the Al<sub>2</sub>O<sub>3</sub> beads, they can be utilized unlimited. Contamination getter (large-sized Ti particles) is used for the purpose of reducing/removing the surface contamination in contamination reduction solution B. Although slight contamination happened each time to the contamination getter, it can still be used several times. In addition, the large-sized Ti particles are able to be replaced by cheap Ti sponges without losing the gettering function. Therefore, it is a realistic solution to reduce/remove the contamination happened for Ti sintering in argon/vacuum in the graphite furnace.

#### 7.4.4 Role of sintering atmosphere

In general, it is typical to have lower densification in argon sintering than vacuum sintering because of the difficulty in removing the gas from pores during sintering. However, it was shown in Table 7-1 that the sintered density of specimens sintered in argon was higher than specimens sintered in vacuum when specimens were exposed directly to the furnace atmosphere and when they were sintered with contamination reduction solution A, which is considered to be due to higher interstitial contents absorbed from the argon atmosphere than from vacuum. This is also confirmed by the mechanical property measurement, especially the tensile ductility, demonstrated in Table 7-2 and Figure 7-7. Since tensile elongation is highly sensitive to interstitial contents, low ductility was observed for specimens sintered in argon because it is believed to have high interstitial content.

### 7.5 Conclusions

Macrostructural cross-sectional observation demonstrated that there existed a contaminated layer with a thickness of 300-500  $\mu\text{m}$  for sintered specimens exposed directly to the furnace atmosphere at the temperature of 1250  $^{\circ}\text{C}$  with a holding time of 4 hours. Theoretical calculation using the solution to Fick's second law for semi-infinite solids indicates that the maximum thickness of the contaminated layer can only be around 17.7  $\mu\text{m}$  assuming oxygen and nitrogen not affecting the diffusion of carbon, which demonstrates this layer could not possible be a single phase because TiC layer as the diffusion path at those conditions would not allow a film of the observed thickness to develop. It was therefore suggested that the interlayer below Ti(CNO) may be a mixture of Ti(CNO) with a solid solution of C in Ti and calculations showed that, within the range of assumptions made, the thickness of such a film could well be in the range of that measured. For the contamination process, carbon is regarded as in gaseous form reacting with titanium. After applying contamination reduction solutions, the contaminated layers are not seen

on the surface of specimens and the surface of specimens sintered in the graphite furnace show metallic colour with no obvious surface scale and with good shape retention in comparison with control solution. The sintered densities and densification levels for sintered with contamination reduction solution A and B both are higher than with control solution. The tensile ductility of sintered Ti with contamination reduction A is much higher than specimens with control solution. All these indicate contamination reduction solution A and solution B both can effectively control the interstitial contamination during the sintering. In addition, experiments also demonstrated the sintered densities of specimens sintered in argon are higher than specimens sintered in vacuum probably because more interstitials are absorbed in argon atmosphere than in vacuum. The tensile ductility of specimens sintered in vacuum are higher than sintered in atmosphere probably because of more interstitials arising from the atmosphere. Since this chapter deals with specimens with -200mesh powders, as to pursue high densification much fine titanium powders are adopted in next chapter.

## **8. PRESSURELESS SINTERING OF Ti-Al-V-Fe TITANIUM ALLOYS FROM ULTRAFINE HYDROGENATED-DEHYDROGENATED TITANIUM POWDER**

Chapter 7 reported the vacuum sintering work of HDH Ti and pre-alloyed Ti-6Al-4V powders. However, vanadium is an expensive and toxic element as described in the literature presented in chapter 2. It is necessary to develop new titanium alloys to replace vanadium with low-cost elements such as iron. In this chapter, a comprehensive study has been conducted on microstructural evolution and mechanical properties of sintered low-cost Ti-Al-V-Fe titanium alloys utilizing ultrafine HDH titanium powder with a median particle size of 8.84  $\mu\text{m}$ . Two different kinds of pores, defined as micropores (5-15  $\mu\text{m}$ ) and macropores (50-200  $\mu\text{m}$ ), were identified in sintered titanium alloys. Spherical micropores were observed in Ti-6Al-4V sintered with ultrafine Ti at the lowest temperature of 1150  $^{\circ}\text{C}$ . The addition of iron can help reduce microporosity and improve microstructural and compositional homogenization. A theoretical calculation of evaporation based on the Miedema model and Langmuir equation indicates that the evaporation of aluminium could be responsible for the formation of the macropores. Although reasonable densification was achieved at low sintering temperatures (93-96% relative density) the samples had poor mechanical properties due mainly to the presence of the macroporosity, the high inherent oxygen content in the as-received ultrafine powders, inhomogeneous microstructure and possibly poor alloy design. Suggestions are also given at the end of the chapter as to possible methods to reduce/eliminate the poor mechanical performance.

### **8.1 Introduction**

Sintering is by far the most common consolidation method in titanium powder metallurgy. The initial stage of sintering can be empirically modelled in terms of isothermal neck growth as measured by the neck size ratio  $X/D$ [13, 14]:

$$(X/D)^n = Bt/D^m \quad (8-1)$$

where  $D$  is the particle diameter,  $X$  = neck diameter,  $t$  = isothermal sintering time and  $B$  is a collection of material and geometric constants. The values of  $n$ ,  $m$ ,  $B$  depend on the mechanism of mass transport. The above empirical equation indicates that sintering is highly sensitive to the particle size, with a smaller particle size giving rise to more rapid sintering.

The sintering data compiled by Robertson et al. confirms that a finer particle size is beneficial for titanium powder densification [16]. However titanium powders with very fine particle size are not usually available, particularly if a low impurity level is required. A particle size of -100 mesh (< 150  $\mu\text{m}$ ), -200 mesh (< 75  $\mu\text{m}$ ), or -325 mesh (< 45  $\mu\text{m}$ ), is most commonly used [5, 6, 102]. A recent study reports a novel technique to produce ultrafine titanium powder with a mean particle size of < 10  $\mu\text{m}$  [121]. The powder reported has a high impurity content of oxygen (> 0.8 wt%) [121]. It is known that high oxygen content can adversely affect mechanical properties, especially ductility [5, 6, 17], and therefore the aim of this chapter is to investigate the feasibility of using an ultrafine titanium powder to sinter titanium products and investigate the effects of these fine powders on densification and mechanical properties.

Current titanium powder metallurgy research has been largely devoted to cost reduction in titanium components by both developing cost-effective powder manufacturing and developing low-cost titanium alloys [49]. In the development of low-cost titanium alloys, the introduction of iron (Fe) as a  $\beta$ -Ti stabilizer into the alloy composition has been widely explored for powder metallurgical titanium alloys [7, 86, 89, 94, 96-99, 168, 169].

Iron is much cheaper than titanium, and the application of 5% Fe is equivalent to saving the use of 5% Ti [7, 168]. Sinterability of titanium alloys can be enhanced by the addition of iron since the mobility of titanium atoms is accelerated by the rapid diffusion of iron [94, 96, 169]. The fast diffusion of iron in titanium alloy is evidenced by the fact that iron is essentially uniform in a blended elemental Ti-10V-2Fe-3Al alloy when heated at 5 °C/min to 1200 °C [86]. Ti-10V-2Fe-3Al (O ≤ 0.13; N ≤ 0.05; C ≤ 0.05; H ≤ 0.015; all in wt%), assigned formally as TIMETAL<sup>®</sup> 10-2-3, has been realized for aircraft under-carriage applications [86, 98]. Further experiments indicate that the sinterability enhancement which can be seen in titanium alloys with the addition of fine iron powder (mean particle size = 8 μm), is not observed when working with coarse iron powder (mean particle size = 97 μm) [89].

From the viewpoint of microstructural design, a significant feature of iron additions is that Ti-Fe is the only eutectoid system, compared with other low-cost titanium alloys such as Ti-Cu, Ti-Si etc. which does not actually undergo eutectoid transformation even under a slow cooling rate [7, 97]. The brittle eutectoid phase (TiFe) can therefore be avoided. However, grain coarsening was found when just 1 wt% more iron was added into the alloying composition of Ti-10V-2Fe-3Al [98]. This is in agreement with the observation that pure titanium with 0.3 wt% Fe had a noticeable grain growth after an annealing heat treatment of 1 hour at 700 °C [1]. Moreover, although the densification and tensile strength was enhanced by the addition of iron for low-cost Ti-xFe-0.5/1Si in the range from 3 wt% to 6 wt %, poor ductility was caused by grain growth with increasing the iron content [99].

Ti-6Al-4V is known as a “work-horse” α+β titanium alloy, which has high strength and good ductility. However, the β-stabilizing element (vanadium) is not only expensive but also toxic to human beings if used as an implant [84]. For blended elemental sintering of Ti-6Al-4V, better sinterability can be obtained using a master alloy powder (Al-V) than when using elemental

aluminum and vanadium [83]. Therefore, this work mainly aims to investigate the effects of the addition of Fe and understand the behaviour of master powders for blended elemental Ti-6Al-4V and low-cost Ti-Al-V-Fe alloys with the use of ultrafine Ti powders.

## 8.2 Experimental

### 8.2.1 Materials

The ultrafine titanium powder, commercially available 60Al-40V master alloy powder and iron powder supplied by Beijing Youxinglian Nonferrous Metals Co. Ltd, China, were employed to balance the designed alloy composition into  $\text{Ti (0.6Al-0.4V)}_{10-x}\text{Fe}_x$ , where  $x=0, 2, 4$  and  $6$ . ie the Fe content ranged from 0 to 6 wt% as a replacement for the master alloy in a Ti-6Al-4V composition. Table 8-1 tabulates the correspondingly impurity levels, particle morphology and particle size for as-received powders.

*Table 8-1: Impurity levels, particle morphology and particle size for as-received powdes*

	C (wt. %)	H (wt. %)	O (wt. %)	N (wt. %)	Particle morphology and size
Ti	0.058	0.414	0.82	0.575	Irregular, median size: 8.84 $\mu\text{m}$
60Al-40V	0.029	0.0005	0.18	0.16	Irregular, median size: 142.31 $\mu\text{m}$
Fe	0.041	0.0022	0.67	0.262	Irregular, < 53 $\mu\text{m}$

### 8.2.2 Theoretical density measurement

The theoretical densities have been determined from a rule of mixtures based on the proportion and density of each element as described by Yang, et al [100]. Since the proportion and density of individual phases, as is normally used in the rule of mixtures, are unknown. The theoretical density ( $\rho_{th}$ ) is expressed as:



$$\rho_{th} = 100 / \sum_j (m_j / \rho_j) \quad (8-2)$$

where  $m_j$  signifies the nominal weight percentage of component  $j$  and  $\rho_j$  is the theoretical density of each component. The theoretical densities of elements titanium (Ti), aluminium (Al), vanadium (V) and iron (Fe) are 4.50 g/cm<sup>3</sup>, 2.7 g/cm<sup>3</sup>, 6.11 g/cm<sup>3</sup> and 7.87 g/cm<sup>3</sup> respectively [153]. If interstitial diffusion occurs during the alloying process, the crystal parameters may increase to a very limited level and the correspondingly small volume change resulting from the interstitial diffusion can be neglected. However, the weight increase caused by the contamination of interstitial elements may be remarkable if a component, such as titanium, is highly reactive. In this situation, the weight increase should not be excluded from the calculation of theoretical density. Assuming the weight percentage of interstitials in component  $j$  is  $m_{ij}$ , the calculation equation of theoretical densities can be modified as:

$$\rho_{th} = 100 / \sum_{i,j} \{[(1 - m_i) \times m_j] / \rho_j\} \quad (8-3)$$

The interstitial contents including oxygen, nitrogen, hydrogen and carbon in the as-received powders were measured by a LECO oxygen-nitrogen-hydrogen analyser (TCH-600) and carbon-sulfur analyser (CS-444). Therefore, the final theoretical densities of Ti-6Al-4V, Ti-4.8Al-3.2V-2Fe, Ti-3.6Al-2.4V-4Fe, Ti-2.4Al-1.6V-6Fe can be calculated as 4.447 g/cm<sup>3</sup>, 4.511 g/cm<sup>3</sup>, 4.578 g/cm<sup>3</sup> and 4.646 g/cm<sup>3</sup> according to Equation 8-3.

### 8.2.3 Press-and-sinter

Compacts were uniaxially pressed at a constant pressure of 300 MPa into two different cylindrical sizes: 16 mm diameter with 5-6 mm thickness, and 45 mm diameter with 3-4 mm thickness. The green density for all four alloys was  $62.9 \pm 0.5$  %. Compacts with dia=16 mm were used for sintering densification calculations and the dia= 45 mm samples were sintered for tensile testing. Vacuum sintering (vacuum level:  $2 \times 10^{-3}$  Pa) was conducted in a high-temperature Mo-heating-element furnace (Dingli, Changsha, China) at 1150 °C, 1250 °C and 1350 °C separately with a soaking time of 3 hours. The racking material was molybdenum plate. The specific heating profile is demonstrated in Figure 8-1.

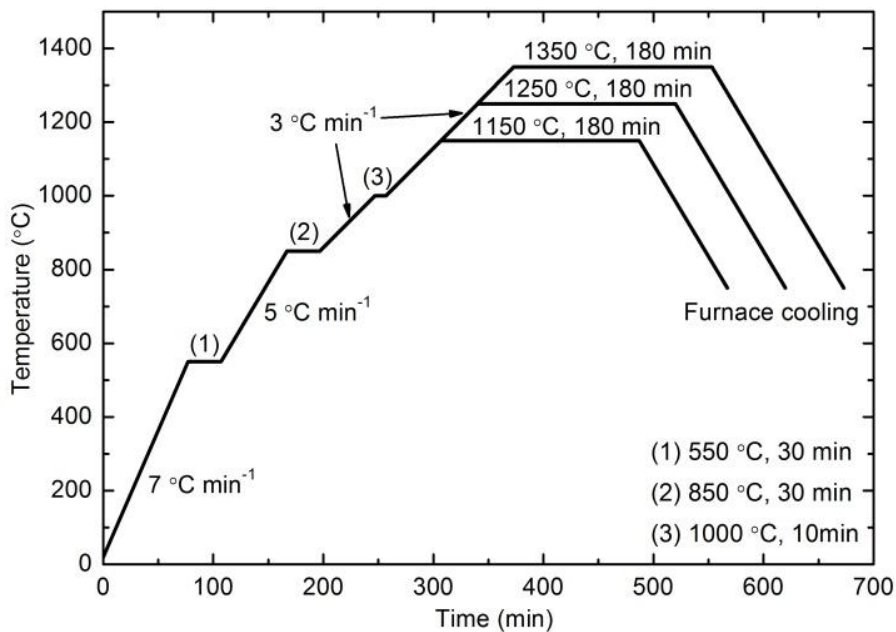


Figure 8-1: Heating schedule for blended elemental sintered titanium alloys

The stepwise heating schedule used in these experiments was designed in an attempt to avoid possible pore formation resulted from the exothermal reaction between elemental powders used

for sintering of Ti-Al-V-Fe alloys. The initial heating rate was set at  $7\text{ }^{\circ}\text{C min}^{-1}$  from room temperature to  $550\text{ }^{\circ}\text{C}$ . A holding time of 30 minutes was introduced at both  $550\text{ }^{\circ}\text{C}$  and  $850\text{ }^{\circ}\text{C}$  and a 10-minute holding time at  $1000\text{ }^{\circ}\text{C}$  were used to prevent the possible pore formation caused by the exothermal reaction between titanium and the master alloy or iron powder, and to allow sufficient time for homogeneous elemental diffusion. A slower heating rate of  $3\text{-}5\text{ }^{\circ}\text{C min}^{-1}$  was employed from  $1000\text{ }^{\circ}\text{C}$  to the final sintering temperature for the same reason. This heating schedule is different to the single step one used in the earlier experiments. In those experiments for the sintering of pure Ti and pre-alloyed Ti-6Al-4V there was no potential for the exothermal reaction or evaporation and therefore the increase in total sintering time using stepwise heating was not deemed necessary. The intention was not to compare the two different schedules, and that will not be addressed in the following discussion.

#### 8.2.4 Characterization and mechanical testing

The particle size distribution was analysed by a particle size analyser (Mastersizer 2000, Malvern). Each data point was averaged from 3-5 specimens. Standard metallographic analysis was carried out as described in Section 3.4. Microstructural morphology observations were conducted on an environmental scanning electron microscope (ESEM) (Quanta 200F, FEI) using both back-scattered and secondary electron modes. Semi-quantitative compositional analysis was carried out by energy dispersive spectrometry (EDS). The sintered density and the phase constituents were determined as shown in Section 3.3.

Tensile specimens were machined from the sintered specimens in compliance with ISO 2892-1:2009 (  $\sim 2.65\text{ mm} \times 2.65\text{ mm}$  cross-section,  $15\text{ mm}$  gauge length and  $20\text{ mm}$  parallel length), and tested on an Instron mechanical tester (Model: 3367, Instron Co., Norwood, MA) with a crosshead speed of  $0.1\text{ mm min}^{-1}$  (initial strain rate:  $1.1 \times 10^{-4}\text{ s}^{-1}$ ). The precise displacement was

determined using an extensometer with a gauge length of 8 mm (model: 2630-120, Instron Co., Norwood, MA). Three tensile specimens were prepared for each point.

## **8.3 Results**

### **8.3.1 Characteristics of as-received powders**

The micrographs of as-received powders are shown in Figure 8-2 including ultrafine titanium, iron and 60Al-40V master powder as well as the particle size distribution of ultrafine titanium and 60Al-40V powders. All three powders show angular morphologies, with Figure 8-2(a) demonstrating that the ultrafine Ti had a much finer particle size than the 60Al-40V (Figure 8-2b) and iron (Figure 8-2c) powders. This is validated by particle size distribution analysis, which illustrates the median particle sizes of ultrafine Ti and master powder were 8.84  $\mu\text{m}$  and 142.31  $\mu\text{m}$ , respectively.

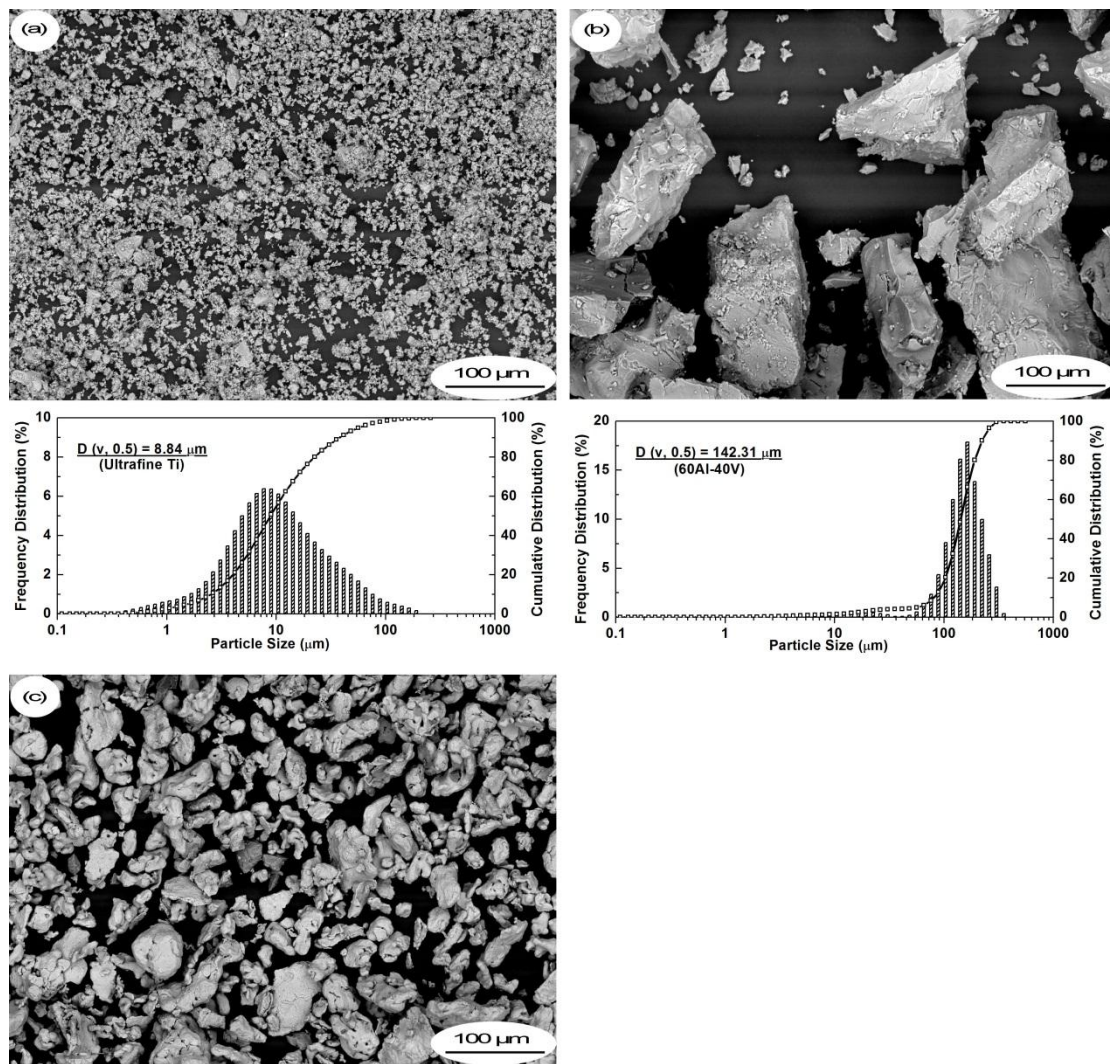


Figure 8-2: SEM images and particle size distribution of ultrafine Ti (a) 60Al-40V master alloy (b) and Fe powders (c)

The diameter of most iron particles was less than 50 μm estimated from Figure 8-2(c), which is accordance with its nominal particle size (-300mesh). XRD patterns of each powder are given in Figure 8-3.

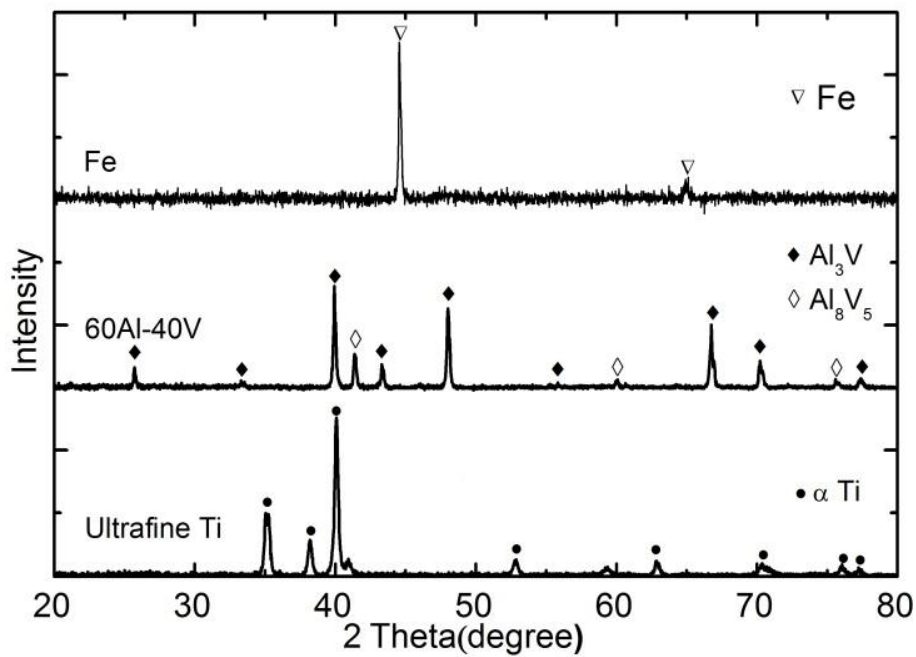


Figure 8-3: XRD patterns of as-received powders

The pattern from the reduced elemental iron powder is indexed as pure iron by JCPDS 87-0721 [170]. The phase of master powder (60Al-40V) is mainly ascribed to Al<sub>3</sub>V (JCPDS 07-0399) with a small amount of Al<sub>8</sub>V<sub>5</sub> (JCPDS 71-0141) [82]. The ultrafine Ti is mainly composed of alpha titanium referenced by JCPDS 44-1294.

### 8.3.2 Densification

The effect of iron content on the relative sintered density and densification level is illustrated in Figure 8-4 for specimens uniaxially pressed at a constant compaction pressure of 300 MPa and sintered at different temperatures.

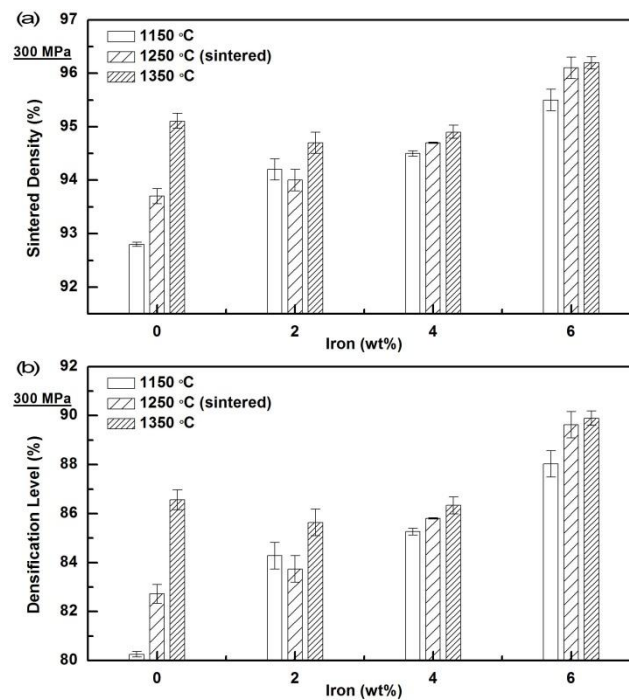


Figure 8-4: Relative sintered density (a) and densification level (b) as a function of iron content for samples sintered at different temperatures

The relative sintered density increased with iron content at sintering temperatures of 1150 °C and 1250 °C (Figure 8-4a). However at a sintering temperature of 1350 °C the relative sintered density of Ti-6Al-4V was comparable to the alloys with low Fe content. Increases in density were observed with sintering temperature and this effect was more pronounced for the Ti-6Al-4V than for the specimens with Fe. The densification level offers an evaluation method for porosity elimination level of green compacts by sintering. Figure 8-4(b) demonstrates that specimens with -6%Fe sintered at 1350 °C have the highest densification level, where ~90% of the porosity of the original green compacts had been eliminated by sintering. The lowest densification level was achieved by the Ti-6Al-4V specimens sintered at a temperature of 1150 °C, where ~20% of the original porosity of the green compacts remained after sintering.

### 8.3.3 Microstructure observation and compositional analysis

Microstructural images taken from cross-sections of the specimens sintered at various temperatures and compositions are shown in Figure 8-5, and confirm the density measurements.

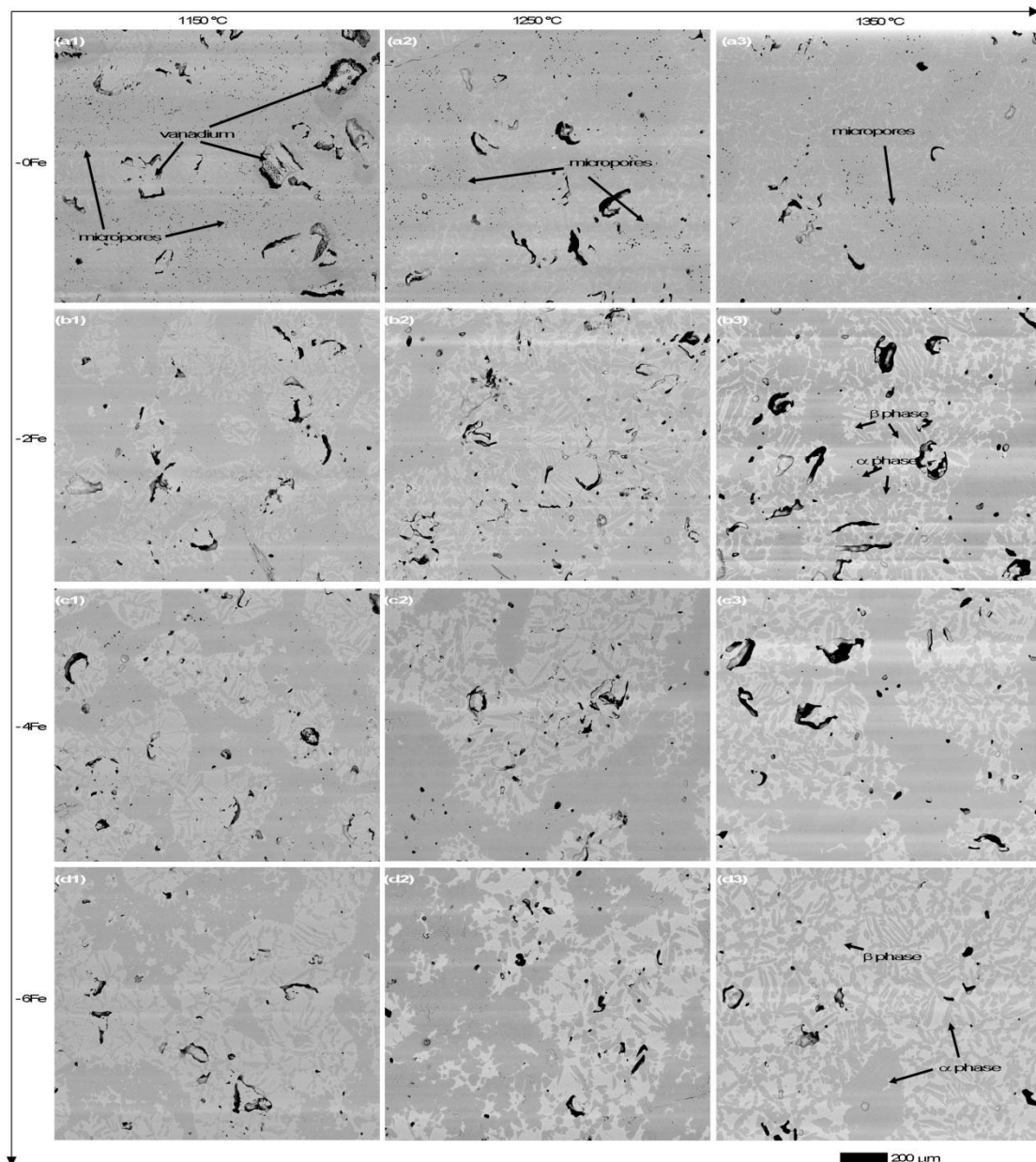


Figure 8-5: Cross-sectional SEM images of sintered titanium alloys at various temperatures and compositions



When sintered at temperatures of 1150 °C and 1250 °C, the porosity decreased with increasing Fe content. At the highest temperature (1350 °C) the relative sintered density of the sample with -2wt% Fe had the lowest density and the microstructure shows the highest porosity seen in Figure 8-5(b3). In comparison, the least porosity was observed in the cross-section of the specimen with -6%Fe shown in Figure 8-5(d3) which had the highest relative sintered density.

Two different kinds of pores are also observed in Figure 8-5 in regard to the pore size and shape. Irregular-shaped macropores with an average size of 50-200 µm were noted in all specimens under different sintering temperatures and compositions. The amount of these macropores decreased with the addition of iron content when sintered at temperatures of either 1150 °C or 1250 °C. At a temperature of 1350 °C, a large quantity of irregular-shaped macropores was observed in specimens with -2wt%Fe. The other kinds of pore observed were spherical with an average diameter of 5-15 µm. A large number of these micropores were distributed among the cross-sectional surface of Ti-6Al-4V at a sintering temperature of 1150 °C, and decreased with increasing sintering temperature. Interestingly, there were only very few micropores observed on the cross-sections of sintered alloys containing iron although their diameter was slightly larger than those in Ti-6Al-4V.

As also shown in Figure 8-5, the microstructures show two distinct regions or phases which appear as light and dark contrast in the SEM, with an increase in the light phase observed with increasing Fe content. It is also observed that the darker contrast regions appear to be in two different morphologies, with smaller needle-like or acicular grains and some much larger particles or grains. In order to further understand these microstructures, compositional analysis was conducted on Ti-6Al-4V sintered at 1150 °C and 1250 °C including EDS line scanning (Figure 8-6) and EDS mapping (Figure 8-7).

The image in Figure 8-6 shows a line scan across the area containing the macropores typically seen in the cross-section of Ti-6Al-4V (Figure 8-5).

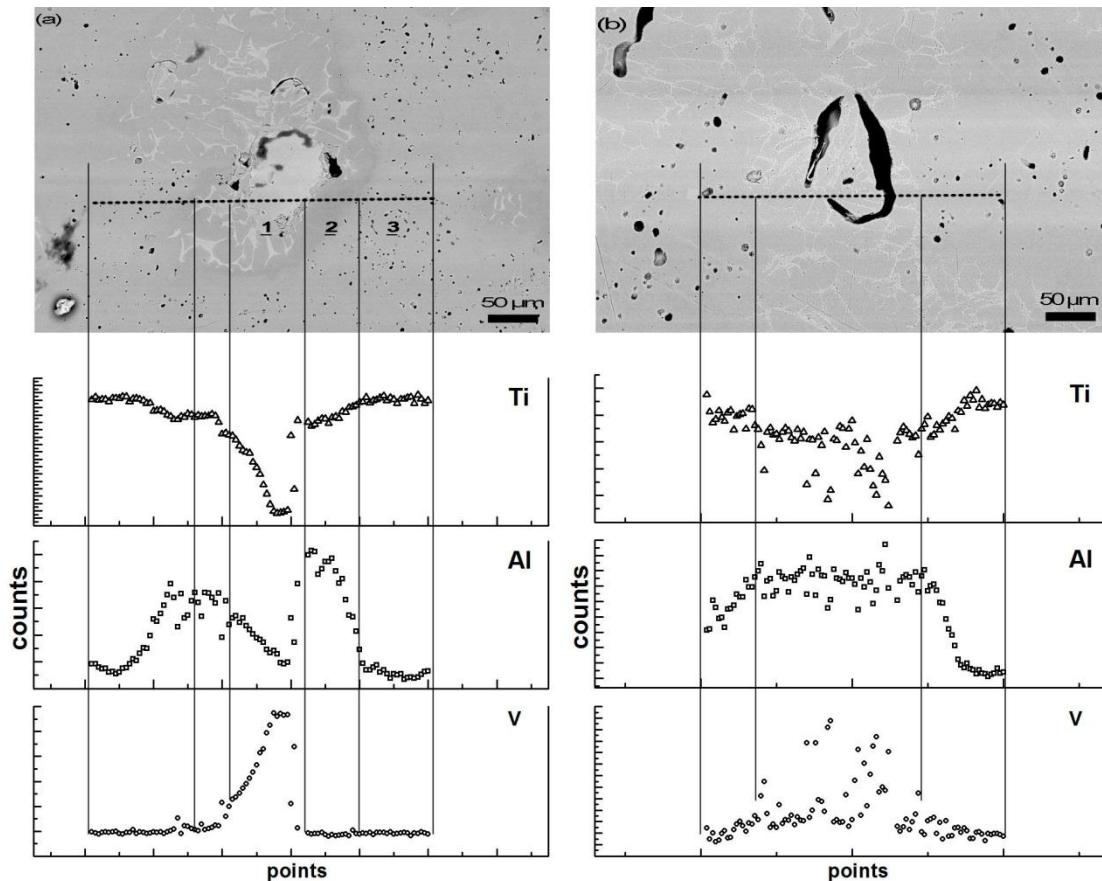


Figure 8-6: EDS line scanning of blended elemental Ti-6Al-4V specimens sintered at (a) 1150 °C and (b) 1250 °C

For the sample sintered at 1150 °C, (Figure 8-6a) the line scan was classified into three different regions depending on the colour contrast. The light contrast regions (particularly the particle at the centre of the pore) were rich in vanadium and contained no Al or Ti. The darkest contrast region around the pore contained both Al and Ti but no V. Moving away from the pore into the mid-contrast, matrix region there was an increase in the Ti content and a corresponding decrease

in Al. The sample sintered at the higher sintering temperature (Figure 8-6b) showed a much more homogenous distribution of all three elements although vanadium was slightly elevated in the lighter contrast regions.

EDS mapping was also carried out on the same materials to investigate the element distribution as highlighted in Figure 8-7.

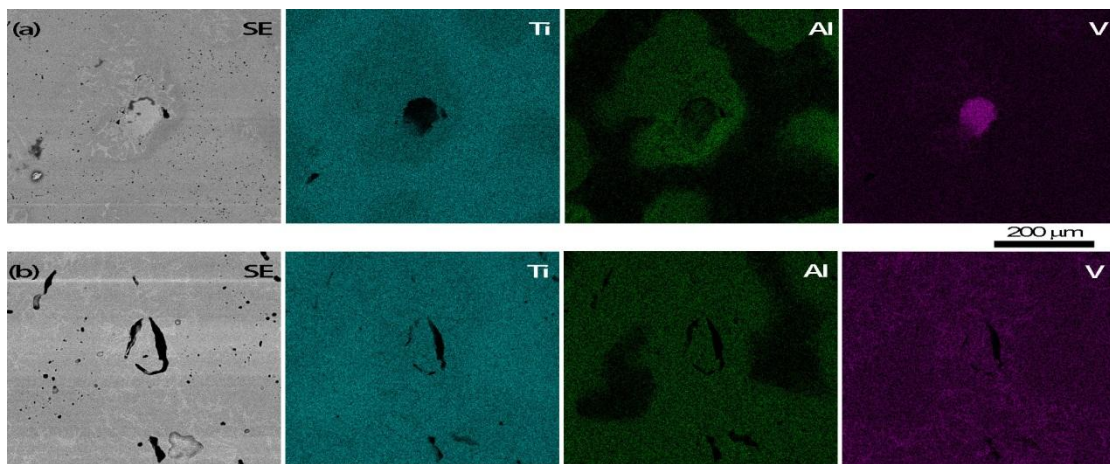


Figure 8-7: EDS mapping of blended elemental Ti-6Al-4V specimens sintered at (a) 1150 °C and (b) 1250 °C

The mapping results are in agreement with the line scanning observation in Figure 8-6. Figure 8-7a shows that region 1 is noticeably rich in vanadium whereas region 2 is rich in aluminium. Also, the intensity of titanium decreases gradually from region 3 to region 1 for specimens sintered at 1150 °C. At the higher sintering temperature (Figure 8-7b), the diffusion area of aluminium became distinctly wider and titanium achieved a more homogeneous elemental distribution when compared with sintering at 1150 °C. A remarkable difference was also witnessed for vanadium, which was no longer isolated in discrete particles but was much more homogeneously distributed.

EDS line scanning and mapping of specimens with 4 wt% iron are highlighted in Figure 8-8 when sintering at the highest temperature (1350 °C).

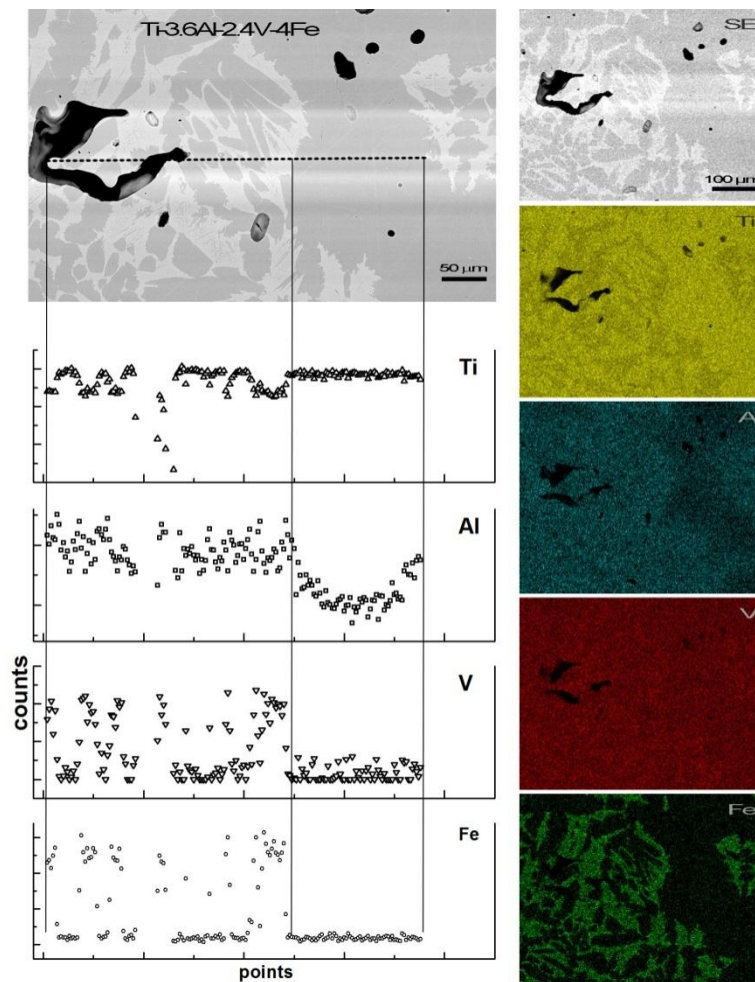


Figure 8-8: EDS mapping (a) and EDS line scanning (b) of Ti-3.6Al-2.4V-4Fe sintered at 1350 °C

In Figure 8-8, inhomogeneous microstructural zones can also be distinguished by dark and light contrast regions. It is observed from the corresponding EDS line scanning and mapping that iron is rich in grains within the light region and is absent in the darker regions. The intensity of aluminium in the blocky darker regions is slightly weaker than those in the lighter contrast areas

while the Ti concentration shows the opposite trend, being lower in the lighter regions than in the darker grains. Comparing sintering at the highest temperature (Figure 8-8) to lower temperatures shown in Figure 8-6 and Figure 8-7, improved elemental distribution homogeneity was observed. For example, the contrast of aluminium shown by EDS mapping in Figure 8-8 is not as strong as shown in Figure 8-7.

#### 8.3.4 Phase determination

The phase analysis of sintered titanium alloys is demonstrated in Figure 8-9, including the XRD patterns of Ti-6Al-4V sintered under different sintering temperatures (Figure 8-9a) and the Ti-Al-V-Fe alloys sintered under a constant temperature of 1350 °C (Figure 8-9b). The XRD patterns of specimens sintered at 1150°C (Figure 8-9a), show that the samples consisted of alpha titanium referred to JCPDS 44-1294 with some  $Ti_3Al$  peaks [162] observed at lower temperatures. The presence of the  $Ti_3Al$  phase at lower temperatures is indicative of the alloying process being incomplete at these temperatures and supports the microstructural observations. At the highest temperature of 1350 °C only alpha titanium peaks were observed and there were no obvious peaks indicating the presence of  $\beta$ -Ti. However, it is important to point out the full width at half maximum (FWHM) was large at the highest sintering temperature, which probably indicates the existence of different compositional solid solution of titanium alloys. This is compatible with the microstructure observation shown in Figure 8-7. In Figure 8-9(b), peaks attributed to the beta titanium phase were observed for the sintered Ti-Al-V-Fe alloys, as suggested by the literature [86, 97], and their intensity increased with increasing iron content in the alloy composition. This indicates that iron stabilizes the beta phase in titanium alloys and more beta can be retained after cooling from the sintering temperature if the iron content is increased. The presence of  $\beta$ -Ti is also in good agreement with the observation that there was no brittle TiFe intermetallic phase formed with similar amount of Fe utilised in Figure 2-10.

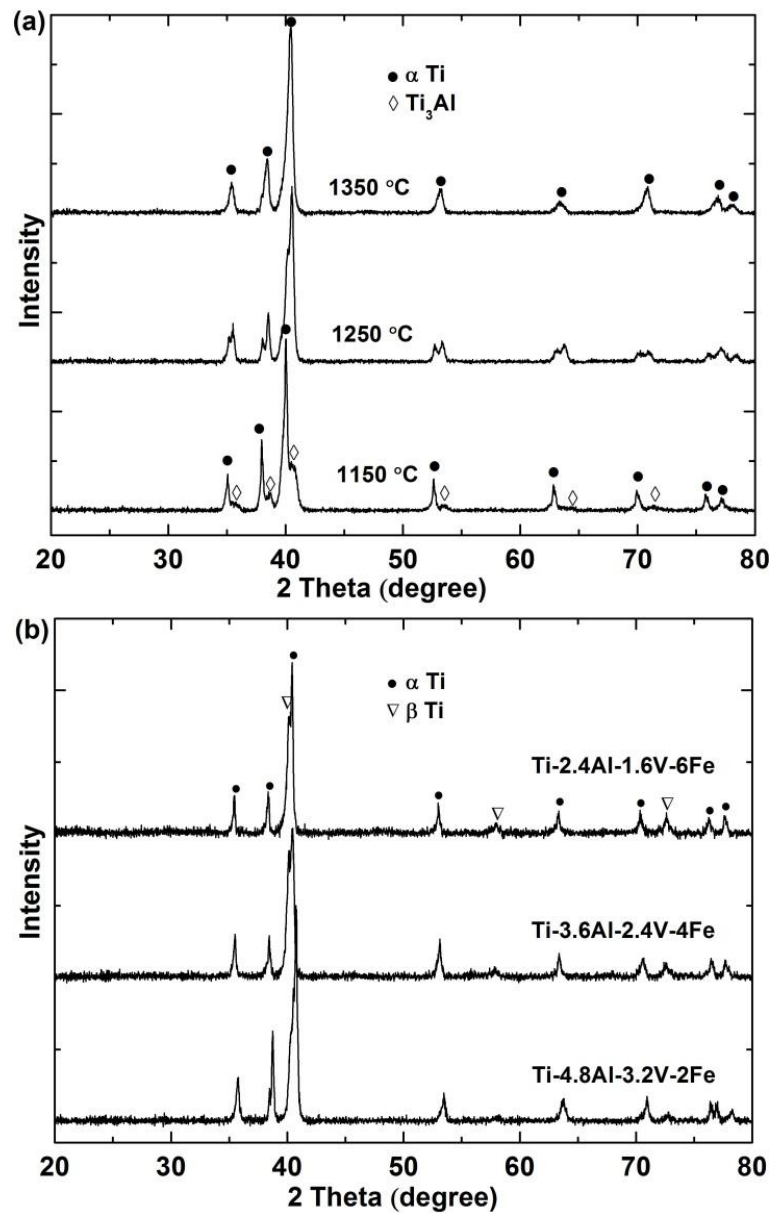


Figure 8-9: XRD patterns of (a) Ti-6Al-4V sintered at various temperatures and (b) Ti-Al-V-Fe of various Fe concentrations sintered at 1350 °C

### 8.3.5 Mechanical properties and fractography

Results of tensile testing of the samples are illustrated in Figure 8-10.

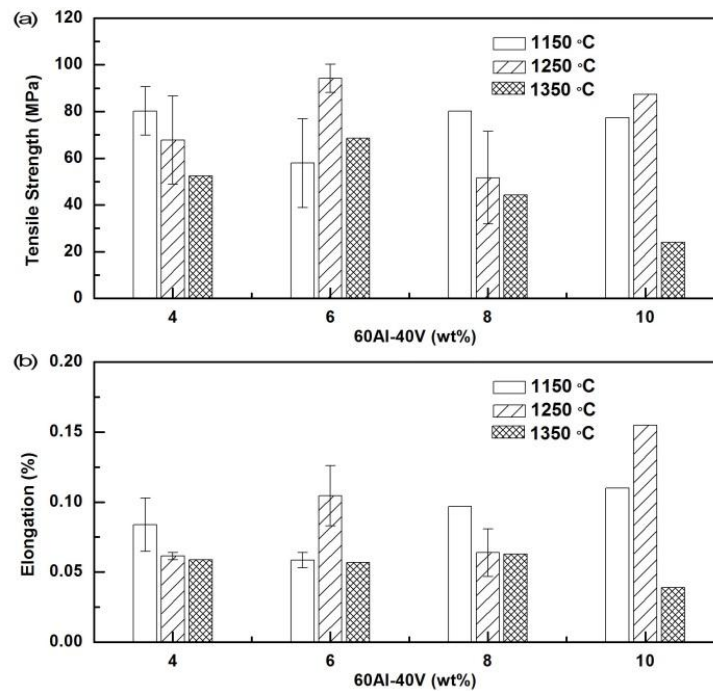


Figure 8-10: Tensile strength (a) and elongation (b) of sintered titanium alloys as a function of master alloy powder content at various temperatures

In general, the tensile mechanical properties were very poor for blended elemental titanium alloys with values of <100 MPa tensile strength and 0.05-0.15 % elongation. Specimens sintered at the highest temperature (1350 °C) appeared to have a lower tensile strength and ductility compared with sintering at lower temperatures (1150 °C and 1250 °C). Although 3-5 repeats were prepared for each data point, some error data are not available in Figure 8-10 due to the specimens breaking prior to tensile testing caused by their lack of ductility. Since extremely low mechanical properties are affected by various parameters such as macroporosity, impurity levels etc. in addition to the lack of available repeats, this makes it difficult to judge whether there was any

significant effect of sintering temperature on mechanical properties. The corresponding fractographs of the as-sintered Ti-2.4Al-1.6V-6Fe at 1250 °C are shown in Figure 8-11.

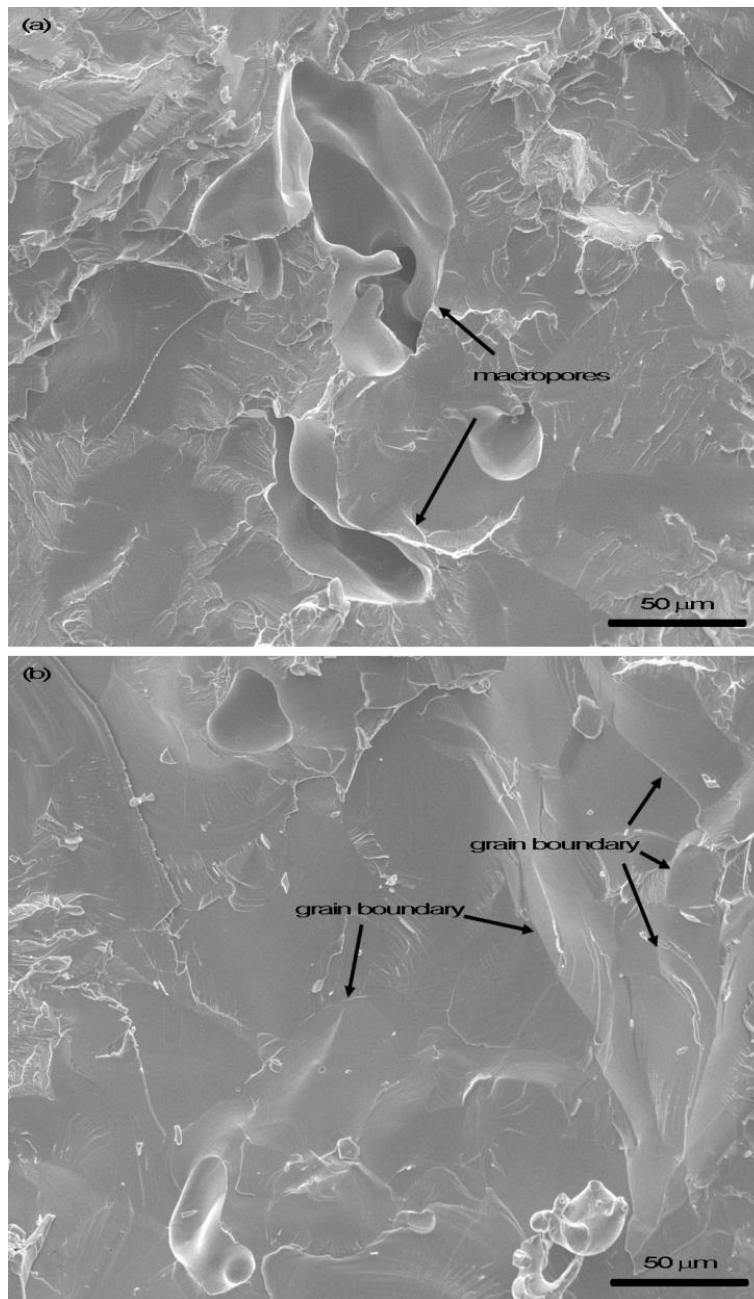


Figure 8-11: Representative fracture morphologies of Ti-2.4Al-1.6V-6Fe sintered at 1250 °C: (a) macropores and (b) brittle fracture surface



Irregular-shaped macropores are observed in Figure 8-11(a) which would result in stress concentration during tension. It can also be seen that the brittle fracture dominates the tensile failure of as-sintered specimens (Figure 8-11b).

## **8.4 Discussion**

### **8.4.1 Microporosity formation**

Two different kinds of pores were formed during sintering, which are defined here as micropores (5-15  $\mu\text{m}$ ) and macropores (50-200  $\mu\text{m}$ ) as shown in Figure 8-5. The micropores observed in Figure 8-5 were spherical and isolated in sintered specimens especially in Ti-6Al-4V even at the lowest sintering temperature (1150  $^{\circ}\text{C}$ ). Pore spheroidization indicates that sintering had entered into the final stage at the lowest temperature (1150  $^{\circ}\text{C}$ ). Although the green density was only about 63% for all of these samples, the sintered density at this lowest temperature was around 93% for the Ti-6Al-4V specimen and increased with increasing iron content up to around 96%. It is considered that the reasonably high levels of densification even at low temperatures and for samples with low green density, as evidenced by the densification results and the presence of isolated small pores, is due mainly to the high sintering driving force resulting from the high surface free energy when using the ultrafine titanium powder, and improved diffusion with the additions of iron.

The evolution of the microporosity for samples with different iron contents as a function of temperature can be seen in the SEM fractographs shown in Figure 8-12.

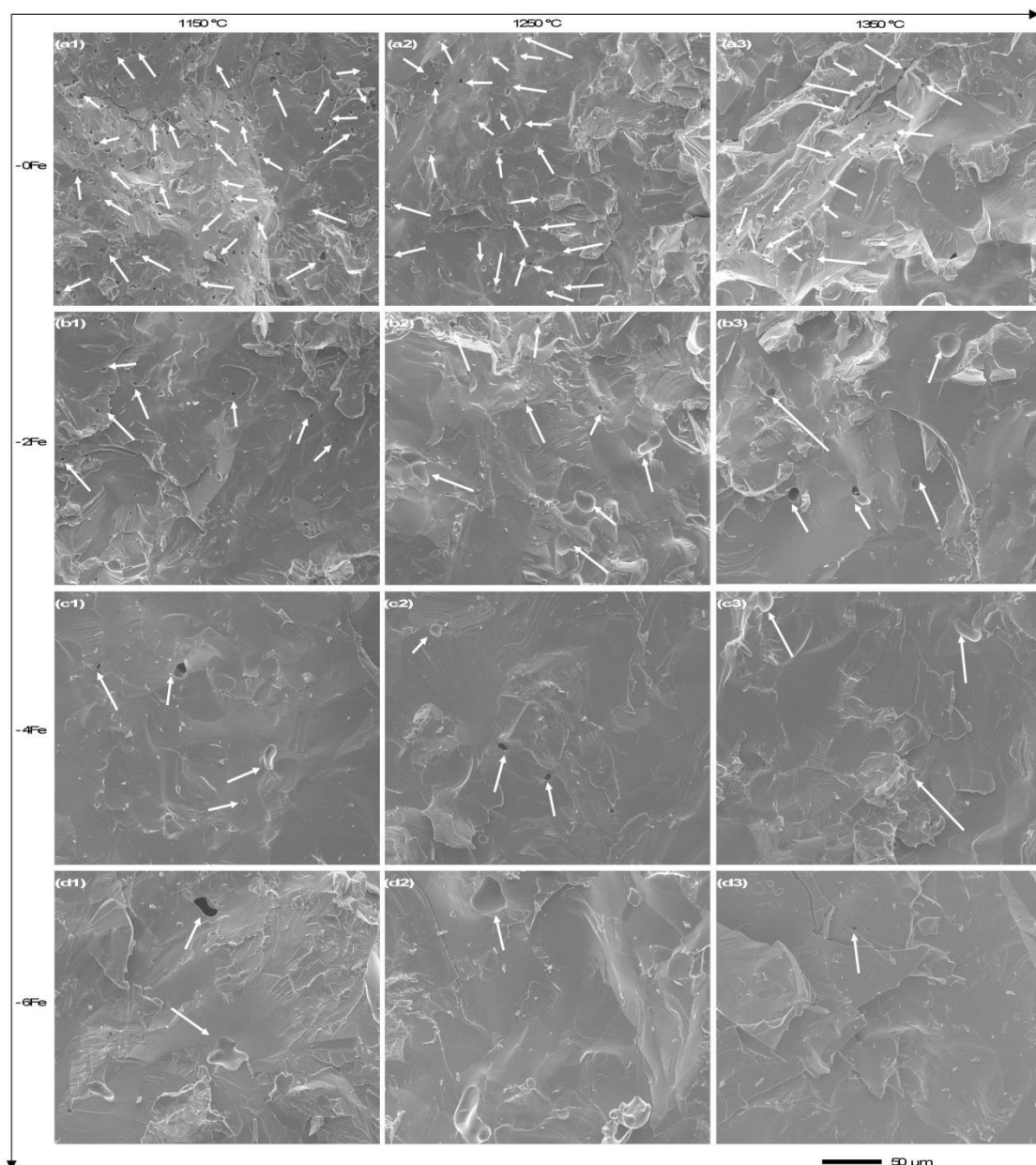


Figure 8-12: SEM fractographs with micropores of tensile specimens sintered at various temperatures and compositions

The micropores shown in Figure 8-12 are in accordance with the observations made from Figure 8-5, whereby the Ti-6Al-4V specimens show the largest number of micropores (diameter  $<10\ \mu\text{m}$ ). Although the amount of microporosity in these samples decreased with sintering temperature, the amount of micropores in the Ti-6Al-4V at any temperature was higher than the

titanium alloy specimens containing iron. For the Fe containing samples, the microporosity decreased with increasing iron content. This indicates that the micropores remaining following sintering of ultrafine titanium powder could be mostly eliminated through the addition of iron and thereby raising the densification.

The diffusion coefficient of elements in ultrapure materials follows an Arrhenius relationship:

$$D = D_0 \exp(-Q/RT) \quad (8-4)$$

where  $D_0$  is the pre-exponential factor ( $\text{m}^2 \text{s}^{-1}$ ),  $Q$  the activation energy ( $\text{kJ mol}^{-1}$ ),  $R$  the molar gas constant and  $T$  the absolute temperature (K). These parameters can be obtained for both the self diffusion of  $\beta$ -Ti and the interdiffusion of Al, V and Fe in pure  $\beta$ -Ti [171] as shown in Table 8-2.

*Table 8-2: Selfdiffusion of  $\beta$ -Ti and Interdiffusion of Al, V and Fe in Pure  $\beta$ -Ti [171]*

Specimen	Diffusion type	Temperature ( $^{\circ}\text{C}$ )	$D_0$ ( $\text{m}^2 \text{s}^{-1}$ )	$Q$ ( $\text{kJ mol}^{-1}$ )
$\beta$ Ti	Selfdiffusion	899 - 1540	$3.58 \times 10^{-8}$	130.6
Al in $\beta$ Ti	Interdiffusion	920 - 1600	$1.14 \times 10^{-5}$	213.1
V in $\beta$ Ti	Interdiffusion	902 - 1543	$3.1 \times 10^{-8}$	134.8
Fe in $\beta$ Ti	Interdiffusion	969 - 1645	$7.8 \times 10^{-7}$	132.3

Diffusion coefficients were calculated using the data presented in Table 8-2 and the ratio of interdiffusion of the different elements to the self-diffusion in Ti are presented in Figure 8-13 over the temperature range of 1000-1400  $^{\circ}\text{C}$ .

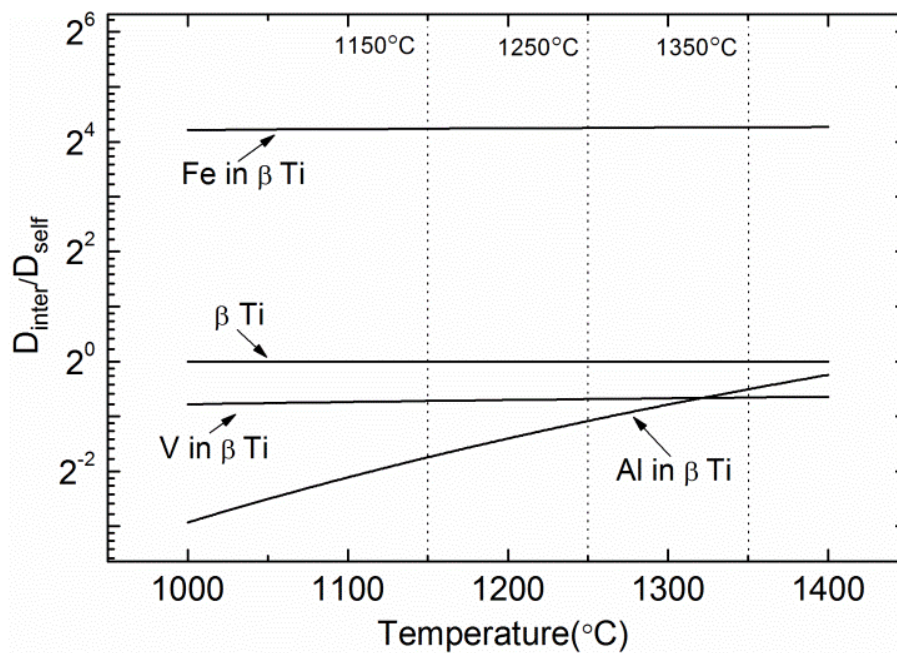


Figure 8-13: Temperature dependence of ratio of interdiffusion coefficients to selfdiffusion coefficient of  $\beta$ -Ti

The interdiffusion coefficient (Ti-Fe) is over 16 times higher than the self-diffusion coefficient ( $\beta$ -Ti) and is also much higher than the interdiffusion coefficients for Ti-Al and Ti-V (both  $<1$ ). This indicates that iron is a fast diffuser in  $\beta$ -Ti, and empirical rules of diffusion suggest that the addition of fast diffusers can enhance self-diffusion rates of both the solute and solvent atoms [100]. Additions of a fast diffuser such as iron can therefore enhance the densification of titanium during sintering.

#### 8.4.2 Macroporosity formation

A fractograph of the Ti-6Al-4V sample sintered at 1150 °C is presented in Figure 8-14 as well as corresponding compositional analysis.

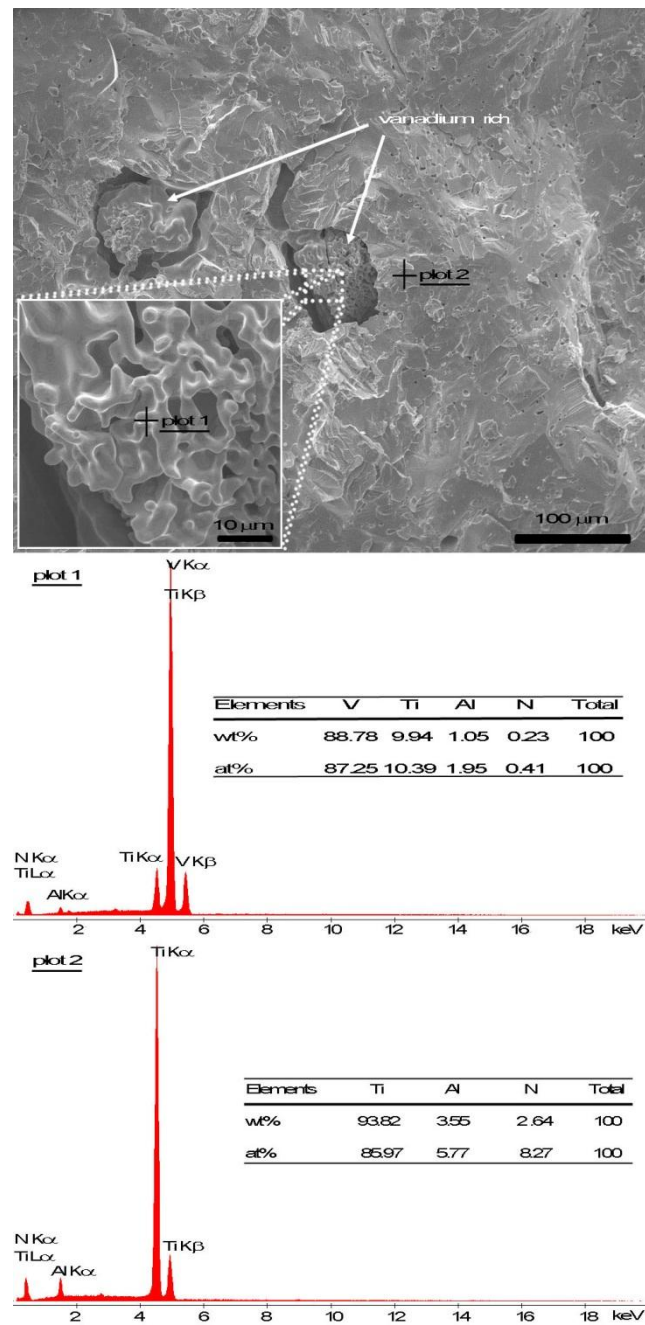


Figure 8-14: Macropores shown in fracture surface of Ti-6Al-4V specimens sintered at 1150 °C

Two macropores ~100  $\mu\text{m}$  in diameter are observed in Figure 8-14, and material with a “coral-like” structure was observed inside the pores. Compositional analysis was conducted on the coral-

like material (plot 1) and the more dense surrounding area (plot 2). The EDS spectra and analysis show that the coral-like material was predominantly vanadium (88.78 wt%) whilst the surrounding area was composed of titanium (93.82 wt%) and a small amount of aluminium (3.55 wt%) but no vanadium. The presence of vanadium-rich “coral-like” material with a smooth cellular wall is considered to be correlated with the evaporation of aluminium according to the following analysis.

Theoretical calculation of the evaporation of binary alloys can be determined based on the Miedema model and Langmuir equation [172-174]. For instance, Guo and his co-workers calculated the theoretical elemental evaporation of a TiAl melt during casting with this model, which had reasonable agreement with the experimental data [172, 174]. Furthermore, Chen et al. also utilized this model to calculate the evaporation of PM fabricated FeAl in good accordance with experimental observations [173].

The evaporation loss rate ( $N_{m,A}$ ) of the component A in a binary A-B alloy system is demonstrated by Langmuir theory [172, 175]:

$$N_{m,A} = K_L \times \varepsilon \times (P_A^e - P_A^g) \times \sqrt{M_A/T} \quad (8-5)$$

The Langmuir constant ( $K_L$ ) is equal to  $4.37 \times 10^{-4}$  when the partial pressure is described in Pascal [172, 174].  $\varepsilon$  is the condensation constant (for metals = 1) [172, 174].  $P_A^e$  indicates the saturated vapour partial pressure of element A in the system and  $P_A^g$  is the partial pressure of the component. Since the specimens were sintered under high vacuum and the volatiles are reactive with titanium substrate, it is proposed that  $P_A^g$  can be considered to be zero.  $M_A$  and  $T$  are the component's atomic mass and absolute temperature respectively.

The saturated vapor partial pressure  $P_A^e$  can be defined by:

$$P_A^e = \chi_A \times \gamma_A \times P_A^0 \quad (8-6)$$

where  $\chi_A$  and  $\gamma_A$  indicate the molar fractions and activity coefficient of component A in the binary system. The equilibrium pressure of pure component A,  $P_A^0$ , can be calculated for Al and V elements by the following formula [176]:

$$\log_{10} P_{Al}^0 = 14.465 - 17342T^{-1} - 0.7927 \log_{10} T \quad (8-7)$$

$$\log_{10} P_V^0 = 14.75 - 27132T^{-1} - 0.5501 \log_{10} T \quad (8-8)$$

The activity coefficient of component A ( $\gamma_A$ ) in a binary system is given by [177]:

$$\ln \gamma_A = \frac{\Omega}{RT} (1 - \chi_A)^2 \quad (8-9)$$

where  $R$  is the ideal gas constant and  $\Omega$  is an interaction parameter which can be obtained by calculating the molar enthalpy of mixing ( $\Delta H_{mix}$ ) for the binary system [177]:

$$\Delta H_{mix} = \Omega \times \chi_A \times \chi_B \quad (8-10)$$

where  $\chi_A$  and  $\chi_B$  are the molar fractions of component A and B respectively.

Substituting Equation 8-10 into Equation 8-9, gives:

$$\ln \gamma_B = \frac{\chi_A}{RT\chi_B} \Delta H_{mix} \quad (8-11)$$

$$\ln \gamma_A = \frac{\chi_B}{RT\chi_A} \Delta H_{mix} \quad (8-12)$$

Thus, the theoretical evaporation loss rate is dependent on the molar enthalpy of mixing ( $\Delta H_{mix}$ ), which can be determined using the model of Miedema [178]:

$$\Delta H_{mix} = \frac{2P\mathcal{f}(c^s)(\chi_A V_A^{2/3} + \chi_B V_B^{2/3})}{(n_{ws}^A)^{-1/3} + (n_{ws}^B)^{-1/3}} \times \left[ -(\phi_A - \phi_B)^2 + \frac{Q}{P} (n_{ws}^{A\ 1/3} - n_{ws}^{B\ 1/3})^2 - R/P \right] \quad (8-13)$$

where  $\mathcal{f}(c^s)$  is given by:

$$\mathcal{f}(c^s) = \mathcal{f}(\chi_A^s \chi_B^s) = \chi_A \chi_B V_A^{2/3} V_B^{2/3} / (\chi_A V_A^{2/3} + \chi_B V_B^{2/3})^2 \quad (8-14)$$

$V_A^{2/3}$ ,  $V_B^{2/3}$ ,  $n_{ws}^{A\ 1/3}$ ,  $n_{ws}^{B\ 1/3}$ ,  $Q$ ,  $P$ ,  $R$ ,  $\phi_A$  and  $\phi_B$  are all constants and are available in the literature [178]. Once the molar enthalpy of mixing is determined, the activity coefficients of Al and V can be calculated from Equation 8-11 and Equation 7-12 and combined with the



equilibrium pressure (Equation 8-7 and Equation 8-8) to give the saturated vapour pressure (Equation 8-6) and ultimately the evaporation rate (Equation 8-5).

The 3 : 2, weight ratio of Al to V in the 60 wt% Al – 40 wt% V master alloy results in an atomic ratio of Al to V of 17:6. Using these figures and the model described above, the dependence of the saturated vapor pressure and evaporation rate on temperature is plotted in Figure 8-15.

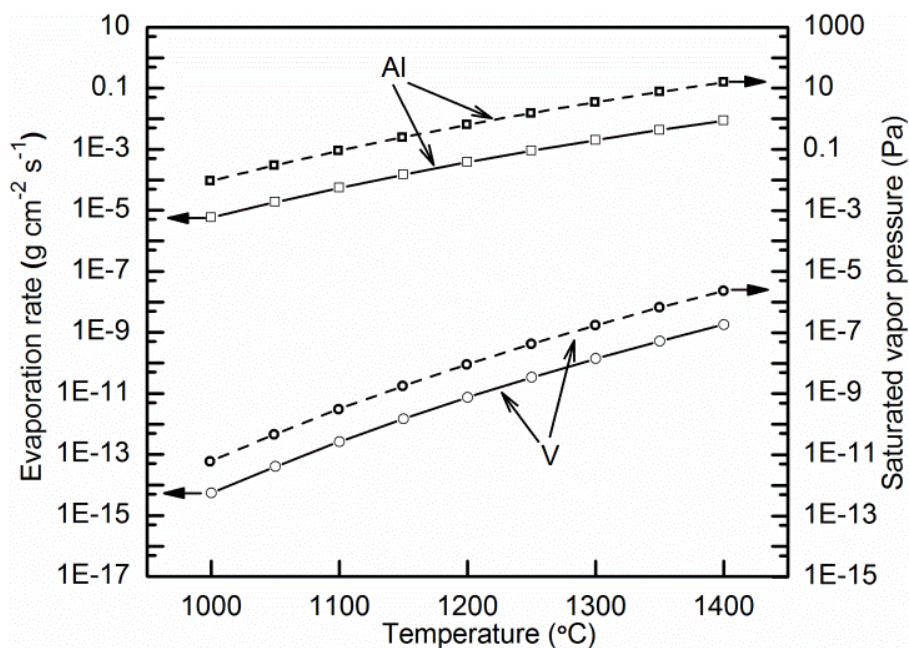


Figure 8-15: The dependence of evaporation rate and saturated vapour pressure on temperature

From Figure 8-15 it can be seen that the saturation vapour pressure of aluminium is  $9.2 \times 10^{-3}$  Pa at a temperature of 1000 °C and increases with temperature. This is higher than the furnace vacuum level of  $2 \times 10^{-3}$  Pa thus suggesting that the Al is in a state of free evaporation [172, 174].

The evaporation rate of aluminium and vanadium are  $1.48 \times 10^{-4}$  g cm<sup>-2</sup> s<sup>-1</sup> and  $1.48 \times 10^{-12}$  g cm<sup>-2</sup> s<sup>-1</sup> respectively at a temperature of 1150 °C seen from Figure 8-15. The median diameter of the

master powder particles was 142.31  $\mu\text{m}$  as shown in Figure 8-1. Assuming the particle is spherical and the compositional ratio is constant, the mass of aluminium and vanadium in this particle would be 3.15  $\mu\text{g}$  and 2.1  $\mu\text{g}$ , respectively. When sintering was conducted at the lowest temperature (1150  $^{\circ}\text{C}$ ) with a holding time of 3-hour, the total loss of aluminium and vanadium by evaporation would be  $1.02 \times 10^3 \mu\text{g}$  and  $1.02 \times 10^5 \mu\text{g}$  respectively. It can be seen that the evaporation loss of aluminium is three orders of magnitude higher than the actual content, whereas, the evaporation of vanadium can be neglected compared with its original mass. This indicates that aluminium had completed the evaporation process before the sintering ends, which is validated by the observation that aluminium is almost non-existent inside the pore shown in Figure 8-14. It is therefore suggested that the macropores are formed due to the high saturated vapor pressure resulting in the evaporation of aluminium and leaving a vanadium rich region inside the pores whose shape and size are taken from original master particles. These macropores would dramatically decrease both tensile strength and ductility.

Although the addition of Fe can reduce the solidus of titanium alloys [7], it is not possible to form a liquid phase between Ti-Fe according to the Ti-Fe phase diagram at the sintering temperature up to 1350  $^{\circ}\text{C}$  with the amounts of iron used in this work [96]. Thus, the evaporation of Al in master alloy powder is still responsible for the formation of macropores observed in Fe containing specimens presented in Figure 8-5. In addition, the macroporosity resulted from the evaporation of master Al-V powder is also mainly responsible for the comparatively low sintered density in relation with the use of ultrafine fine Ti powders presented in Figure 8-4.

#### 8.4.3 Microstructural evaluation and phase transformation

Haase et.al.[82] sintered c.p. Ti powder ( $<150 \mu\text{m}$ ) blended with a 60Al-40V master powder ( $<160 \mu\text{m}$ ) prepared by equal-channel angular pressing and the investigation revealed retarded dissolution of master alloy particles due to the formation of Al-rich and V-rich layers, which were

assumed to be comprised of intermetallic phases [82]. Therefore, for blended elemental Ti-6Al-4V sintered at the temperature of 1150 °C shown in Figure 8-6(a) and Figure 7-7(a), the phase of region 2 can be suggested as  $\alpha_2$ -Ti<sub>3</sub>Al [122], which is in agreement with the phase determination illustrated in Figure 7-9(a). Moreover, the diffusion of elements in  $\alpha_2$ -Ti<sub>3</sub>Al is much slower than in  $\beta$ -Ti, for example the diffusion coefficient of Al in  $\beta$ -Ti is almost 2-3 orders of magnitude higher than in  $\alpha_2$ -Ti<sub>3</sub>Al [122]. Therefore, such intermetallic phase may be considered as a diffusion barrier for vanadium diffusion which was left by the evaporation of aluminium from the master alloy powders. As indicated by Equation 8-4 the diffusion coefficient increases with temperature and the intermetallic phases would become no longer stable at higher temperature (1250 °C and 1350 °C) compared with 1150 °C. This is in accordance with the observation shown in the literature [82]. Therefore, only  $\alpha$ -Ti phase was observed at higher temperature with no intermetallic phase as shown in Figure 8-9(a).

The light region shown in Figure 8-5 is considered to be  $\beta$  phase because of the abundance of  $\beta$ -stabilizers such as iron and vanadium. The dark region is suggested to be  $\alpha$  phase at high temperature (1250 °C and 1350 °C) including both the blocky regions and acicular grains. Interestingly, the two different “alpha” morphologies are not consistent in composition. In the larger, blocky regions the Al content is much lower and this is thought to be a result of incomplete diffusion of the alloying elements into the Ti matrix because of the distance from the master alloy particle which is the source of aluminium. Such is compatible with the unusual microstructural observation.

#### 8.4.4 Mechanical properties

Although the microporosity was reduced with the addition of iron, the mechanical properties of these samples were poor as shown in Figure 8-10. This is thought to be due to the presence of

macroporosity, inhomogeneous microstructure, and high oxygen content in the as-received titanium powders. The macroporosity and microstructure inhomogeneity have been discussed sufficiently in sections. High oxygen levels in particular are detrimental to the mechanical properties in PM Ti components [5, 6, 17]. The dependence of oxygen content on median particle size for HDH titanium powder is summarized from the literature [6, 179] in Figure 8-16.

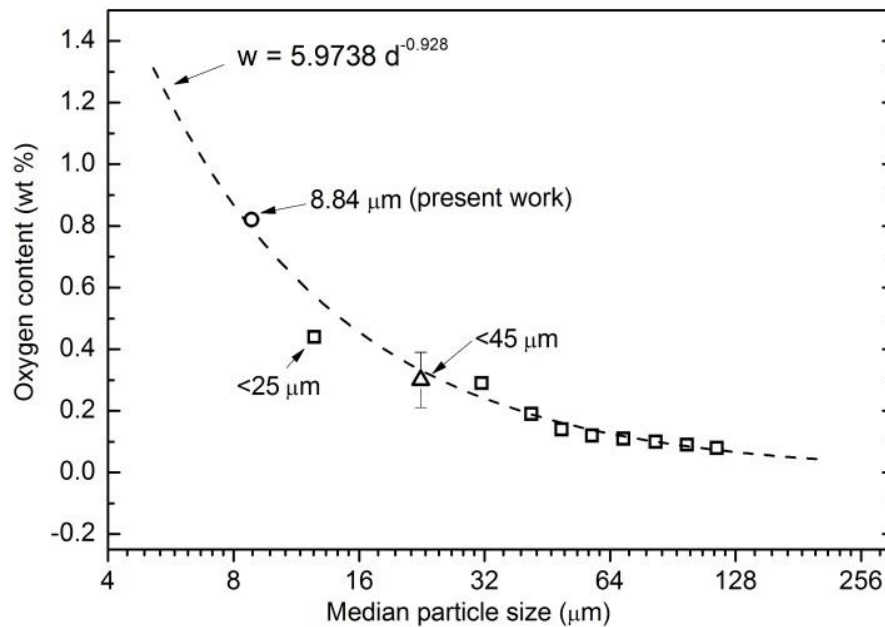


Figure 8-16: Dependence of oxygen content on median particle size of HDH titanium powder

The correlation between oxygen content and median particle size shown in Figure 8-16 can be expressed by a power-law equation:

$$w = 5.9738 d^{-0.928} \quad (8-15)$$

where  $w$  is the oxygen content (wt%) and  $d$  is the median particle size ( $\mu\text{m}$ ). The relationship between oxygen content (0.82 wt%) and the median particle size (8.84  $\mu\text{m}$ ) of the ultrafine powder used in this work fits well with this relationship. Since oxygen has high solubility in  $\beta$ -Ti [55], the oxygen element can enter into the titanium lattice and the oxide formed on the titanium particle surface would disappear at high sintering temperature [5]. Therefore, although ultrafine titanium powders have high interstitial impurity contents, it would not affect the densification of blended alloys.

It is suggested that the low room temperature ductility results observed for these samples arises from grain boundary embrittlement where the oxygen may precipitate from titanium grains due to much lower oxygen solubility at room temperature than at high temperature and form brittle oxides along the grain boundaries. Therefore this work has shown that although appropriate densification can be obtained at low temperatures when using the ultrafine titanium powder, the high levels of oxygen impurities could be one reason which results in poor mechanical properties.

Another possible reason for the poor mechanical properties could arise from the alloy design. Although Fe, as a low-cost fast  $\beta$ -stabiliser element, was added with the target to lower the cost and promote densification, in reality it also altered the alloy composition since it was used to balance out the weight loss of master powder (60Al-40V) rather than single  $\beta$ -stabiliser element (V). A number of possible solutions for achieving better mechanical properties may be proposed based on the results of this work. It is suggested to use low-impurity content ultrafine Ti powders in order to overcome the high oxygen issues described above. It is noted however that at the present time such powders are not commercially available. Utilising finer master Al-V powders should allow more rapid particle dissolution into the Ti matrix, and thus assist in eliminating the evaporations issues and providing a more homogeneous microstructure. Finally, in this work it was not possible to separate the issues related to the ultrafine Ti powder, the master alloy and the

iron additions. It would be useful to consider compositions where the Fe is used only to replace the equivalent  $\beta$ -stabilising element rather than replacing the combined  $\alpha$  and  $\beta$ -stabiliser. I.e. compositions such as 6Al-4V, 6Al-2V-2Fe and 6Al-4Fe.

## 8.5 Conclusions

Four different blended elemental titanium alloys were designed and sintered through varying the weight percentage of an ultrafine Ti powder with (Al-V) master alloy and iron powders. Spherical micropores were formed during sintering with ultrafine titanium powder even at the lowest sintering temperature for Ti-6Al-4V. With the addition of Fe, the microporosity was reduced and improved microstructural and compositional homogenization was observed. This is due to fast diffusion of iron in titanium and thereby enhancing densification. However, the tensile mechanical properties of these blended elemental titanium alloys were poor with values of <100 MPa tensile strength and 0.05-0.15 % elongation. This was mainly caused by high impurity content in the as-received powders and the formation of macropores around the original master alloy particles. Incomplete dissociation of the master alloy particles caused severe evaporation of aluminum resulting in the formation of macropores during sintering. At the lowest temperature of 1150 °C,  $\alpha_2$ -Ti<sub>3</sub>Al was initially formed around the master alloy particles, which was suggested as a diffusion barrier to vanadium. This intermetallic phase was decomposed and was not observed when samples were sintered at 1250 °C and 1350 °C.

Although reasonable densification could be obtained with ultrafine titanium powders and this could be improved with the addition of iron, the properties were low because of the high inherent oxygen, macroporosity resulting from the evaporation of Al in master powders, and inhomogeneous microstructure. Therefore, special precautions have to be taken when using these

powders, and based on the results of this work, suggestions are provided as to how improved mechanical properties may be achieved.

## 9. OVERALL SUMMARY AND KEY FINDINGS

Since limited works currently focus on the study of residual magnesium chloride impurities originating from the mainstream Ti sponge production process — Kroll process using molten magnesium reducing titanium chlorides to produce titanium sponges, the starting point of this thesis was an investigation of magnesium chloride impurities in Kroll-processed HDH titanium powders. Experimental results indicated that these impurities were present in the form of jigsaw-like particles on the surface of titanium powder particles and in the form of  $\text{Mg}(\text{OH})\text{Cl}$  and titanium chlorides revealed by surface chemical analysis. With a target to study the effect of chloride impurities on titanium sintering, such HDH titanium powders were sintered in a graphite furnace due to the potential capability to control the oxygen concentration in the furnace atmosphere resulting from the reaction between carbon and oxygen. However, severe contamination was observed on the surface of sintered titanium specimens indexed as a  $\text{Ti}(\text{CNO})$  porous layer whereas the cross-section was characterized as pure alpha titanium. In addition, typical sintering phenomena were observed on the cross-sections in regard to the evolution of pore size, pore shape and grain size with increasing sintering temperatures and holding times. In order to understand the effect of contamination on mechanical properties of sintered specimens, a large-sized cylinder was pressed and sintered. The results demonstrated that a ductility gradient was presented for the large-sized cylinder increasing from 0.23 % elongation for tensile slices obtained close to the surface, 3 % for slices taken from closer to the centre, and 6 % for samples manufactured from the central slices because of the gradient of interstitial contents. Meanwhile, interesting surface morphologies were observed on the surface and subsurface of sintered titanium where many hollow  $\text{Ti}(\text{CNO})$  spheres were present, which is considered to be detrimental to densification. The formation of spherical hollow particles is thought due to the



reaction between the gaseous carbon and gaseous titanium atoms decomposed from titanium chlorides arising from the decomposition of hydrated magnesium chlorides. In other words, the presence of chlorides is detrimental to the final sintering densification because of the formation of these hollow spheres. A model was suggested to understand the formation mechanism of these particles. Hydrated magnesium chlorides can decompose into  $\text{MgOHCl}$  and gaseous  $\text{HCl}$  which can react with titanium and form titanium chlorides. However, titanium chlorides are not stable at elevated temperature and release gaseous titanium ions. These titanium gaseous ions can further react with the atmosphere (gaseous carbon, nitrogen, oxygen) and form the spherical titanium oxycarbonitride. The formation of spheres is due to the lowest surface free energy state.

According to the above analysis, it can be seen that the contamination on the surface lead to low densification and poor mechanical properties. Therefore, in order to eliminate or reduce the contamination, the development of a cleaner furnace atmosphere was investigated through different contamination-reduction containment trials. For Ti and Ti-6Al-4V specimens sintered with these contamination-reduction methods, the surfaces showed metallic colour with no obvious surface scale and with good shape retention. The sintered densities and mechanical properties for samples sintered with contamination reduction solutions were higher than specimens directly exposed in the furnace. All of these results indicate that contamination reduction solutions can effectively control the interstitial contamination during the sintering of Ti and Ti-6Al-4V. In order to understand the contamination of the surface, a model based on the solution to Fick's second law for semi-infinite solids was proposed to calculate the maximum thickness of the contaminated scale using the thickness of  $\text{TiC}$  instead of  $\text{Ti(CNO)}$ , assuming that oxygen and nitrogen did not affect the diffusion of carbon in the titanium matrix. This model showed that this layer could not be a single phase  $\text{TiC}$  layer because the diffusion path at those conditions would not allow a film of the observed thickness to develop. It was suggested that the layer may be a mixture of  $\text{TiC}$  with a solid solution of C in Ti and calculations showed that,

within the range of assumptions made, the thickness of such a film could well be in the range of that measured.

The cost of master alloy powders (60Al-40V), for use in Ti alloy production, is expensive particularly vanadium which is also toxic. Thus, it is necessary to develop titanium alloys with low-cost alloying elements. Four different blended elemental titanium alloys were designed and sintered through varying the weight percentage of an ultrafine Ti powder with (Al-V) master alloy and iron powders. Small-sized spherical micropores ( $<15\ \mu\text{m}$ ) were formed during sintering with ultrafine titanium powder even at the lowest sintering temperature of  $1100\ \text{°C}$  for Ti-6Al-4V. The microporosity was reduced and improved microstructural and compositional homogenization was observed with the addition of Fe. However, the mechanical properties of these alloys were poor with values of  $<100\ \text{MPa}$  tensile strength and  $0.05\text{-}0.15\ \%$  elongation. It is believed that the high impurity content in the as-received powders and the formation of macropores around the original master alloy particles could be responsible for the low property values. Incomplete dissociation of the master alloy particles resulted in severe evaporation of aluminum resulting in the formation of macropores during sintering. An evaporation calculation model based on the Miedema model and Langmuir equation for binary alloys showed that the theoretical saturation vapour pressure of aluminium is much higher than the furnace vacuum level thus suggesting that the Al is in a state of free evaporation. In addition, the calculation also demonstrated the evaporated weight loss of aluminium during holding time in the sintering period was larger than the original aluminium content in Al-V master particles. Therefore, it is considered that the macropores are formed due to the high saturated vapor pressure resulting in the evaporation of aluminium and leaving a vanadium rich region inside the pores whose shape and size are taken from original master particles. These macropores would dramatically decrease tensile mechanical properties including both tensile strength and ductility.

## 10. CONCLUSIONS

Although powder metallurgy has the advantage of the potential as low-cost manufacturing technology because of its near net shape ability for fabrication of titanium and its alloys, there are still many research gaps to be filled such as the understanding of impurities in raw materials and new alloy design. In this study several works have been carried out to address these issues and the conclusions are brought together and shown below.

- Investigation of the magnesium chloride impurities in HDH Kroll-processed titanium powders showed the presence of jigsaw-like material located on the surface of titanium particles which was identified mainly in the form of  $\text{Mg}(\text{OH})\text{Cl}$  and titanium chlorides by surface chemical analysis. These chlorides are considered to arise from the decomposition of hydrated magnesium chlorides formed during sponge titanium processing, and are supported by a study of the thermal decomposition of pure hydrated magnesium chlorides which also demonstrates  $\text{Mg}(\text{OH})\text{Cl}$  can further decompose into gaseous hydrogen chloride and magnesium oxide.
- For the case of HDH c.p. titanium powder compacts, spherical hollow particles of  $\text{Ti}(\text{CNO})$  were observed on the surfaces of sintered Ti samples, but not on the sintered surface of pre-alloyed Ti-6Al-4V which is regarded as chlorine free. The formation of spherical hollow particles is postulated to be caused by the reaction between the gaseous carbon and gaseous titanium atoms decomposed from titanium chlorides. Therefore the presence of chlorides is detrimental to the final sintering densification because of the formation of these hollow spheres.
- Sintering of commercially pure titanium powders in a reducing atmosphere utilizing argon gas in a graphite lined furnace resulted in contamination from within the furnace, with a  $\text{Ti}(\text{CNO})$  scale formed on the surface with a thickness of 300 - 500  $\mu\text{m}$ . However, the interiors of sintered specimens were pure single phase alpha titanium and typical sintering phenomena were observed. With increasing sintering temperature, irregular and open pores in the interior of specimens

sintered at 1100 °C with an average size of 50-100  $\mu\text{m}$  became isolated and spherical pores with average diameter of 20 – 50  $\mu\text{m}$  were observed in the interiors of samples sintered at 1250 °C and 1400 °C. Grain sizes increased from around 50  $\mu\text{m}$  at 1100 °C, to around 90  $\mu\text{m}$  at 1250 °C and 200  $\mu\text{m}$  at 1400 °C for the specimens sintered with the same 4-hour soaking time.

- Based on an analysis using the solution to Fick's second law for semi-infinite solids, and the data from samples sintered at a temperature of 1250 °C with a soaking time of 4 hours, it was shown that the contaminated layer could not be a single phase and it was suggested that the interlayer below Ti(CNO) may be a mixture of Ti(CNO) with a solid solution of C in Ti. Subsequent calculations showed that, within the range of assumptions made, the thickness of such a film could well be in the range of that measured.
- Tensile mechanical properties of slices manufactured from a larger sintered sample with a relative sintered density of 95.8 % illustrated that the specimens from the interior of the sample had better mechanical properties than those taken from closer to the surface. The average ductility increased with the distance from the surface from 0.23 % to around 6 %. The average ultimate tensile strength of specimens within the sample were always higher than the surface, but went through a maximum with distance from the surface. The UTS increased from 259.3 MPa close to the surface to 570 MPa before decreasing to 389 MPa for the sample from the centre of the specimen due to lower interstitial contents resulting in less solid solution strengthening. The corresponding fracture mechanism changed from brittle intergranular fracture to cleavage fracture and final ductile fracture with dimples with increasing distance from the surface).
- The contaminated layer observed when samples were directly exposed to the surface environment was successfully eliminated by applying contamination reduction solutions. Samples sintered in this way showed a fine metallic lustre with no obvious surface scale and with good shape retention in comparison with the control arrangement. The sintered densities and densification levels for samples sintered with both contamination reduction solutions were also

higher than the control samples. Mechanical properties of the samples sintered with the contamination reduction method were much better than the control samples, with average tensile strengths showing almost twofold increase and ductility improving from 0.3 to 1.3%.

- When sintered at the same sintering conditions including sintering temperature, holding time, contamination reduction solution and etc., experiments demonstrated the sintered densities of specimens sintered in argon were higher than specimens sintered in vacuum probably because more interstitials are absorbed in argon atmosphere than in vacuum. The lower interstitial content for samples sintered in vacuum resulted in much higher ductility (9.7%) compared to the samples sintered in argon (1.3%).
- Four different blended elemental titanium alloys were designed and sintered through varying the weight percentage of an ultrafine Ti powder with (Al-V) master alloy and iron powders. Spherical micropores were formed during sintering with ultrafine titanium powder even at the lowest sintering temperature for Ti-6Al-4V. With the addition of Fe, the microporosity was reduced and improved microstructural and compositional homogenization was observed. This is due to fast diffusion of iron in titanium and thereby enhancing densification.
- The tensile mechanical properties of these blended elemental titanium alloys were poor with values of <100 MPa tensile strength and 0.05-0.15 % elongation. This was mainly caused by high impurity content in the as-received powders, the formation of macropores around the original master alloy particles, and inhomogeneous microstructure. Incomplete dissociation of the master alloy particles caused severe evaporation of aluminum resulting in the formation of macropores during sintering. At the lowest temperature of 1150 °C,  $\alpha_2$ -Ti<sub>3</sub>Al was initially formed around the master alloy particles, which was suggested as a diffusion barrier to vanadium. This intermetallic phase was decomposed and was not observed when samples were sintered at 1250 °C and 1350 °C.

## 11. FUTURE WORKS

In this thesis, the effects of contaminants including chlorine, carbon, nitrogen and oxygen, particle size and alloying elements are investigated on titanium sintering and effective contamination-reduction solutions are developed to remove interstitials in the graphite furnace. Specifically in this chapter, further discussion and suggestion to future works will be divided into three parts including the effect of residual magnesium chlorides on titanium sintering, sintering in the graphite furnace and development of Ti-Al-V-Fe alloys with ultrafine Ti.

### 11.1 Effect of chloride additions on titanium sintering

In chapter 4, jigsaw-like agglomerates were observed on the particle surface of Kroll-processed HDH c. p. titanium powders and further detailed surface chemical analysis carried out by XPS revealed that the magnesium and chlorine mainly existed as  $Mg(OH)Cl$  and titanium chloride respectively. This investigation of chloride impurities in HDH titanium powders gives the guidance to the effect of magnesium chloride impurities on titanium sintering. For example, it indicates the released hydrogen chloride gas and gaseous titanium chlorides may affect the sintering densification adversely. This is validated by sintering in the graphite furnace presented in Chapter 6, which illustrates the presence of chloride impurities in HDH powders resulted in the formation of hollow spheres on the surface and subsurfaces thereby being detrimental to the final sintering densification. However, more detailed works are still in need for future works.

It is thus suggested to conduct the study using different additions of chloride impurities in titanium powders on sintering in the graphite furnace with contamination reduction and/or in a high-vacuum furnace utilised in Chapter 8. This work is expected to understand the dependence

of chloride additions on possible microstructural evolution such as grain refinement, change of porosity and mechanical properties. Additional attention should be paid on the effect of possible solid decomposition reaction product – magnesium oxide (MgO) from hydrated magnesium chlorides demonstrated in Chapter 4.

### **11.2 Effect of sintering atmosphere pressures on titanium sintering in a graphite furnace**

It has been demonstrated that titanium sintering in the graphite furnace can be contaminated by the carbon potentials associated with oxygen and nitrogen arising from the backfilled argon gas and/or low vacuum levels in the furnace as presented in Chapter 5, and effective contamination-reduction solutions have been developed to remove these interstitials as illustrated in Chapter 7.

It is recommended to carry out sintering under different argon pressures to study its effect on titanium sintering. Theoretically, it should be possible to promote the densification if the internal pores are closed prior to the gas filling [13, 14] although determining the correct time to introduce the gas is difficult to judge during sintering, and is probably related to the pressure level. Therefore, experiments to investigate the level of gas pressure and the time of gas introduction and their effect on pore evolution and corresponding mechanical properties should be carried out.

### **11.3 Development of titanium alloys with ultrafine titanium powders using oxygen getter**

In Chapter 8, spherical micropores with a diameter  $<15\ \mu\text{m}$  were formed during sintering of Ti-6Al-4V with ultrafine titanium powder even at the lowest sintering temperature (1100 °C). Although reduced microporosity and improved microstructural and compositional homogenization was achieved through the addition of iron to the alloy, mechanical properties

were poor because of high oxygen content in the Ti powders and macroporosity formed by the evaporation of master powders.

It is suggested to utilise oxygen getters such as 0.6 wt% yttrium hydride (YH<sub>2</sub>) [123] or  $\leq 0.5$  wt% cerium silicide (CeSi<sub>2</sub>) [72] to reduce the detrimental effect of high-content oxygen. In addition, it is also necessary to use fine master powder replacing large-sized master powder utilised in Chapter 8 to avoid possible evaporation because fine powder can be dissolved into the titanium matrix before reaching sintering temperature.



## 12. REFERENCES

1. Lütjering, G. and J.C. Williams, *Titanium*. 2nd ed. 2007, Berlin Germany: Springer-Verlag.
2. Qian, M., G.B. Schaffer, and C.J. Bettles, *Sintering of titanium and its alloys*, in *Sintering of advanced materials: fundamentals and processes*, Z.Z. Fang, Editor. 2010, Woodhead Publishing: Philadelphia, USA. p. 324-355.
3. Leyens, C. and M. Peters, eds. *Titanium and titanium alloys: fundamentals and applications*. 2003, WILEY-VCH: Weinheim, Germany.
4. Eylon, D. and S.R. Seagle, *Titanium technology in the USA - an overview*. *Journal of Materials Science & Technology*, 2001. **17**(4): p. 439-443.
5. Qian, M., *Cold compaction and sintering of titanium and its alloys for near-net-shape or preform fabrication*. *International Journal of Powder Metallurgy*, 2010. **46** (5): p. 29-44.
6. Robertson, I.M. and G.B. Schaffer, *Review of densification of titanium based powder systems in press and sinter processing*. *Powder Metallurgy*, 2010. **53**(2): p. 146-162.
7. Qian, M., et al., *Design of low cost high performance powder metallurgy titanium alloys: some basic considerations*. *Key Engineering Materials*, 2012. **520**: p. 24-29.
8. Barnes, J.E., W. Peter, and C.A. Blue, *Evaluation of low cost titanium alloy products*. *Materials Science Forum*, 2009. **618-619**: p. 165-168.
9. Limberg, W., et al., *Influence of the sintering atmosphere on the tensile properties of MIM-processed Ti 45Al 5Nb 0.2B 0.2C*. *Materials Science and Engineering A*, 2012. **552**: p. 323-329.
10. Fang, Z.Z. and P. Sun, *Pathways to optimize performance/cost ratio of powder metallurgy titanium - a perspective*. *Key Engineering Materials*, 2012. **520**: p. 15-23.

11. Metal-powder: available from <http://www.metal-powder.net/view/25636/dynamet-supplies-titanium-alloys-to-boeing/> (accessed July, 2013).
12. Dynamet technology: available from <http://www.dynamettechnology.com/> (accessed July 2013).
13. German, R.M., *Powder metallurgy and particulate materials processing*. 2005, Princeton, USA: Metal Powder Industries Federation.
14. German, R.M., *Sintering theory and practice*. 1996, New York: John Wiley & Sons, Inc.
15. Segal, D., *Chemical synthesis of advanced ceramic materials*. 1989, New York: Cambridge University Press.
16. Robertson, I.M. and G.B. Schaffer, *Some effects of particle size on the sintering of titanium and a master sintering curve model*. Metallurgical and Materials Transactions A-Physical Metallurgy and Materials Science, 2009. **40A**(8): p. 1968-1979.
17. Wang, H.T., Z.Z. Fang, and P. Sun, *A critical review of mechanical properties of powder metallurgy titanium*. International Journal of Powder Metallurgy, 2010. **46** (5): p. 45-57.
18. Kuang, Y., T.L. Ngai, H. Luo, Y. Li, *SiC-Ti layered material prepared by binder-treated powder sintering*. Journal of Materials Processing Technology, 2009. **209**: p. 4607-4610.
19. Low, R.J., I.M. Robertson, G.B. Schaffer, *Excessive porosity after liquid-phase sintering of elemental titanium powder blends*. Scripta Materialia, 2007. **56**(10): p. 895-898.
20. Bautista, A., C. Moral, G. Blanco, F. Velasco, *Influence of sintering on the corrosion behavior of a Ti-6Al-4V alloy*. Materials and Corrosion, 2005. **56**(2): p. 98-103.
21. Dewidar, M.M. and J.K. Lim, *Properties of solid core and porous surface Ti-6Al-4V implants manufactured by powder metallurgy*. Journal of Alloys and Compounds, 2008. **454**(1-2): p. 442-446.
22. Abkowitz, S. and D. Rowell, *Superior fatigue properties for blended elemental P/M Ti-6Al-4V*. Journal of Metals, 1986. **38**(8): p. 36-39.

23. Ferri, O.M., T. Ebel and R. Bormann, *High cycle fatigue behaviour of Ti-6Al-4V fabricated by metal injection moulding technology*. Materials Science and Engineering: A, 2009. **504**(1-2): p. 107-113.
24. Lapovok, R., D. Tomus and B.C. Muddle, *Low-temperature compaction of Ti-6Al-4V powder using equal channel angular extrusion with back pressure*. Materials Science and Engineering: A, 2008. **490**(1-2): p. 171-180.
25. Frary, M., et al., *Microstructure and mechanical properties of Ti/W and Ti-6Al-4V/W composites fabricated by powder-metallurgy*. Materials Science and Engineering: A, 2003. **344**(1-2): p. 103-112.
26. Guo, S., X. Qu, X. He, T. Zhou, B. Duan, *Powder injection molding of Ti-6Al-4V alloy*. Journal of Materials Processing Technology, 2006. **173**(3): p. 310-314.
27. Yapici, G.G., et al., *Microstructure and mechanical properties of severely deformed powder processed Ti-6Al-4V using equal channel angular extrusion*. Scripta Materialia, 2003. **49**(10): p. 1021-1027.
28. Godfrey, T.M.T., et al., *Microstructure and tensile properties of mechanically alloyed Ti-6Al-4V with boron additions*. Materials Science and Engineering: A, 2000. **282**(1-2): p. 240-250.
29. Chen, G., P. Cao and N. Edmonds, *Porous NiTi alloys produced by press-and-sinter from Ni/Ti and Ni/TiH<sub>2</sub> mixtures*. Materials Science and Engineering: A, 2013. **582**: p. 117-125.
30. Froes, F.H. and D. Eylon, *Powder metallurgy of titanium alloys*. International Materials Reviews, 1990. **35**(3): p. 162-182.
31. Huang, P.Y., *Powder Metallurgy Principles*. 1997, Changsha, China: Metallurgy Industry Press.
32. Kang, S.L., *Sintering: densification, grain growth, and microstructure*. 2005, London, UK: Elsevier.

33. Ivasishin, O.M., et al., *Cost-effective blended elemental powder metallurgy of titanium alloys for transportation application*. Key Engineering Materials, 2000. **188**: p. 55-61.
34. Welsch, G., et al., *Deformation-behavior of blended elemental Ti-6Al-4V compacts*. Metallurgical Transactions A-Physical Metallurgy and Materials Science, 1983. **14**(4): p. 761-769.
35. Zhao, Z.L., et al., *Deformation behavior of isothermally forged Ti-5Al-2Sn-2Zr-4Mo-4Cr powder compact*. Journal of Materials Processing Technology, 2009. **209**(15-16): p. 5509-5513.
36. Minabe, M. and H. Endoh, *Development of high density sintered titanium alloys using a sinter-HIP process*. Metal Powder Report, 1990. **45**(10): p. 673-681.
37. Bocanegra-Bernal, M.H., *Hot Isostatic Pressing (HIP) technology and its applications to metals and ceramics*. Journal of Materials Science, 2004. **39**(21): p. 6399-6420.
38. Low, R.J., et al., *Sintering of titanium powder compacts for containerless Hot Isostatic Pressing*. Materials Science Forum, 2009. **618-619**: p. 509-512.
39. Luo, S.D., et al., *Microwave heating, isothermal sintering and mechanical properties of powder metallurgy titanium and titanium alloys*. Metallurgical and Materials Transactions A-Physical Metallurgy and Materials Science, 2013. **44A**(4): p. 1842-1851.
40. Chen, G.Z., D.J. Fray and T.W. Farthing, *Direct electrochemical reduction of titanium dioxide to titanium in molten calcium chloride*. Nature, 2000. **407**(6802): p. 361-364.
41. Chen, W., et al., *The investigation of die-pressing and sintering behavior of ITP CP-Ti and Ti-6Al-4V powders*. Journal of Alloys and Compounds, 2012. **541**: p. 440-447.
42. Froes, F.H., *Titanium powder metallurgy: A Review - Part 1*. Advanced Materials & Processes, 2012. **170** (9): p. 16-22.
43. Fuwa, A. and S. Takaya, *Producing titanium by reducing TiCl<sub>2</sub>-MgCl<sub>2</sub> mixed salt with magnesium in the molten state*. JOM, 2005. **57**(10): p. 56-60.

44. Van Vuuren, D.S., S.J. Oosthuizen and M.D. Heydenrych, *Titanium production via metallothermic reduction of  $TiCl_4$  in molten salt: problems and products*. Journal of the South African Institute of Mining and Metallurgy, 2011. **111**(3): p. 141-148.
45. Takedal, O. and T.H. Okabe, *Synthesis and enrichment of titanium subchlorides in molten salts*, in *Innovations in Titanium Technology*, ed. M.N. Gungor, M.A. Imam and F.H. Froes. 2007, Warrendale: Minerals, Metals & Materials Soc. p. 69-78.
46. Doblin, C., A. Chryss and A. Monch, *Titanium powder from the TiRO (TM) process*. Key Engineering Materials, 2012. **520**: p. 95-100.
47. Glenn, A., C. Doblin and C. MacRae, *A high temperature ESEM investigation into the separation of  $MgCl_2$  from  $MgCl_2 - Ti$  mixture*. Microscopy and Microanalysis, 2009. **15**: p. 680-681.
48. Ivasishin, O.M., et al., *Role of Surface Contamination in titanium PM*. Key Engineering Materials, 2012. **520**: p. 121-132.
49. Peter, W., et al., *Current status of Ti PM: progress, opportunities and challenges*. Key Engineering Materials, 2012. **520**: p. 1-7.
50. Baril, E., L.P. Lefebvre, and Y. Thomas, *Interstitial elements in titanium powder metallurgy: sources and control*. Powder Metallurgy, 2011. **54**(3): p. 183-187.
51. Chen, G., et al., *Debinding behaviour of a water soluble PEG/PMMA binder for Ti metal injection moulding*. Materials Chemistry and Physics, 2013. **139**(2-3): p. 557-565.
52. Chen, G., et al., *Debinding Kinetics of a Water Soluble Binder System for Titanium Alloys Metal Injection Moulding*. Key Engineering Materials, 2012. **520**: p. 174-180.
53. Chen, G., et al., *Using an agar-based binder to produce porous NiTi alloys by metal injection moulding*. Intermetallics, 2013. **37**: p. 92-99.
54. Sidambe, A.T., et al., *Metal injection moulding of CP-Ti components for biomedical applications*. Journal of Materials Processing Technology, 2012. **212**(7): p. 1591-1597.

55. Massalski, T.D., in *Binary Alloys Phase Diagrams*, H. Okamoto, P.R. Subramanian and L. Kasprzak, Editors. 1990, OH: ASM International Materials Park.
56. Guryn, S.V., I.N. Pogrelyuk and V.N. Fedirko, *Carbooxidation of titanium alloys by contact and noncontact methods*. Metal Science and Heat Treatment, 2004. **46**(9-10): p. 440-444.
57. Guryn, S.V., I.N. Pogrelyuk and V.N. Fedirko, *Mechanism of carbooxidation of titanium by thermal diffusion saturation*. Metal Science and Heat Treatment, 2006. **48**(3-4): p. 181-184.
58. Yan, M., et al., *Impacts of trace carbon on the microstructure of as-sintered biomedical Ti-15Mo alloy and reassessment of the maximum carbon limit*. Acta Biomaterialia, 2014. **10**(2): p. 1014-1023.
59. Zhao, D., et al., *Microstructure and mechanical behavior of metal injection molded Ti-Nb binary alloys as biomedical material*. Journal of the Mechanical Behavior of Biomedical Materials, 2013. **28**: p. 171-182.
60. Li, S.F., et al., *Powder metallurgy Ti-TiC metal matrix composites prepared by in situ reactive processing of Ti-VGCFs system*. Carbon, 2013. **61**: p. 216-228.
61. Sidambe, A.T., F. Derguti and I. Todd, *Metal injection moulding of low interstitial titanium*. Key Engineering Materials, 2012. **520**: p. 145-152.
62. Kondoh, K., et al., *Multi-walled carbon nanotubes reinforced titanium composites via powder metallurgy process*. Key Engineering Materials, 2012. **520**: p. 261-268.
63. Wasz, M.L., et al., *Effect of oxygen and hydrogen on mechanical properties of commercial purity titanium*. International Materials Reviews, 1996. **41**(1): p. 1-12.
64. Yuan, B.G., et al., *Influence of hydrogen content on tensile and compressive properties of Ti-6Al-4V alloy at room temperature*. Materials Science and Engineering: A, 2010. **527**(16-17): p. 4185-4190.

65. Low, R.J., M. Qian, and G.B. Schaffer, *Sintering of titanium with yttrium oxide additions for the scavenging of chlorine impurities*. Metallurgical and Materials Transactions A-Physical Metallurgy and Materials Science, 2012. **43A**(13): p. 5271-5278.
66. Alman, D.E. and S.J. Gerdemann, *Sintering of sponge and hydride-dehydride titanium powders*. P/M Science & Technology Briefs, 2004. **6**(1): p. 11-14.
67. Fan, Z., et al., *Effect of Cl on microstructure and mechanical properties of in situ Ti/TiB MMCs produced by a blended elemental powder metallurgy method*. Journal of Microscopy-Oxford, 1997. **185**: p. 157-167.
68. Andersen, P.J. and P.C. Eloff, *Development of higher performance blended elemental powder metallurgy Ti alloys*. in *Powder metallurgy of titanium alloys*. 1980. Las Vegas, Nevada: Metallurgical Society of AIME.
69. Mahajan, Y., et al. *Microstructure property correlation in cold pressed and sintered elemental Ti-6Al-4V powder compacts*. in *Powder metallurgy of titanium alloys*. 1980. Las Vegas, Nevada: Metallurgical Society of AIME.
70. Jackson, A., J. Motteff and F. Froes, *On the effect of NaCl on porosity in elemental-blend powder-metallurgy Ti-5Al-2.5Sn*. Metallurgical Transactions A, 1984. **15**(1): p. 248-249.
71. Moody, N.R., et al., *The role of inclusion and pore content on the fracture-toughness of powder-processed blended elemental titanium alloys*. Metallurgical Transactions A-Physical Metallurgy and Materials Science, 1993. **24**(1): p. 161-174.
72. Yang, Y.F., et al., *Impurity scavenging, microstructural refinement and mechanical properties of powder metallurgy titanium and titanium alloys by a small addition of cerium silicide*. Materials Science and Engineering: A, 2013. **573**: p. 166-174.
73. Liu, Y., et al., *Rare earth elements: is it necessary for PM Ti alloys*. Key Engineering Materials, 2012. **520**: p. 41-48.

74. Bedjanian, Y. and E. Loukhovitskaya, *Adsorption of water vapor on  $MgCl_2 \times 6H_2O$  salt surface*. Atmospheric Environment, 2011. **45**(14): p. 2373-2378.
75. Bedjanian, Y. and E. Loukhovitskaya, *Water interaction with  $MgCl_2 \times 6H_2O$  and NaCl surfaces: measurements of the uptake coefficient*. Journal of Atmospheric Chemistry, 2009. **63**(2): p. 97-108.
76. Jeong, M.-S., et al., *A unified model for compaction and sintering behavior of powder processing*. Finite Elements in Analysis and Design, 2012. **53**: p. 56-62.
77. Xia, Y., et al., *Cobalt-doped Ti-48Al-2Cr-2Nb alloy fabricated by cold compaction and pressureless sintering*. Materials Science and Engineering: A, 2013. **574**: p. 176-185.
78. Robertson, I.M. and G.B. Schaffer, *Refinement of master densification curves for sintering of titanium*. Metallurgical and Materials Transactions A-Physical Metallurgy and Materials Science, 2010. **41A**(11): p. 2949-2958.
79. Bolzoni, L., et al., *Modification of sintered titanium alloys by Hot Isostatic Pressing*. Key Engineering Materials, 2012. **520**: p. 63-69.
80. Lapovok, R., et al., *The effect of hydrogenation on the ECAP compaction of Ti-6Al-4V powder and the mechanical properties of compacts*. Materials Science and Engineering: A, 2009. **513-514**: p. 97-108.
81. Lapovok, R., D. Tomus and B.C. Muddle, *Low-temperature compaction of Ti-6Al-4V powder using equal channel angular extrusion with back pressure*. Materials Science and Engineering: A, 2008. **490**(1-2): p. 171-180.
82. Haase, C., et al., *Production of Ti-6Al-4V billet through compaction of blended elemental powders by equal-channel angular pressing*. Materials Science Engineering: A, 2012. **550**: p. 263-272.



- 
83. Ivasishin, O.M., et al., *Synthesis of alloy Ti-6Al-4V with low residual porosity by a powder metallurgy method*. Powder Metallurgy and Metal Ceramics, 2002. **41**(7-8): p. 382-390.
  84. Geetha, M., et al., *Ti based biomaterials, the ultimate choice for orthopaedic implants – A review*. Progress in Materials Science, 2009. **54**(3): p. 397-425.
  85. Wikipedia: available from <http://en.wikipedia.org/wiki/Iron> (accessed on 26th August, 2013).
  86. Yang, Y.F., et al., *Sintering of Ti-10V-2Fe-3Al and mechanical properties*. Materials Science and Engineering: A, 2011. **528**(22-23): p. 6719-6726.
  87. Dobrescu, M., S. Dimitriu and M. Vasilescu, *Studies on Ti-Al-Fe low-cost titanium alloys manufacturing, processing and applications*. Metalurgia International, 2011. **16**(4): p. 73-76.
  88. Min, X.H., et al., *Effects of Fe addition on tensile deformation mode and crevice corrosion resistance in Ti-15Mo alloy*. Materials Science and Engineering: A, 2010. **527**(10-11): p. 2693-2701.
  89. Esteban, P.G., E.M. Ruiz-Navas and E. Gordo, *Influence of Fe content and particle size on the processing and mechanical properties of low-cost Ti-xFe alloys*. Materials Science and Engineering: A, 2010. **527**(21-22): p. 5664-5669.
  90. Chen, T.F., et al., *Thermodynamic investigation of Fe-Ti-Y ternary system*. Transactions of Nonferrous Metals Society of China, 2009. **19**(1): p. 199-204.
  91. Gunawarman, et al., *Effect of  $\beta$  phase stability at room temperature on mechanical properties in  $\beta$ -rich  $\alpha+\beta$  type Ti-4.5Al-3V-2Mo-2Fe alloy*. ISIJ International, 2002. **42**(2): p. 191-199.

92. Gunawarman, B., et al., *Mechanical properties of Ti-4.5Al-3V-2Mo-2Fe and possibility for healthcare applications*. Materials Science and Engineering: C, 2005. **25**(3): p. 296-303.
93. Ouchi, C., H. Fukai, and K. Hasegawa, *Microstructural characteristics and unique properties obtained by solution treating or aging in  $\beta$ -rich  $\alpha+\beta$  titanium alloy*. Materials Science and Engineering: A, 1999. **263**(2): p. 132-136.
94. Liu, Y., et al., *Design of powder metallurgy titanium alloys and composites*. Materials Science and Engineering: A, 2006. **418**(1-2): p. 25-35.
95. Simchi, A. and G. Veltl, *Behaviour of metal powders during cold and warm compaction*. Powder Metallurgy, 2006. **49**(3): p. 281-287.
96. Wei, W., et al., *Effect of Fe addition on sintering behaviour of titanium powder*. Powder Metallurgy, 2003. **46**(3): p. 246-250.
97. Chen, B.Y., K.S. Hwang and K.L. Ng, *Effect of cooling process on the alpha phase formation and mechanical properties of sintered Ti-Fe alloys*. Materials Science and Engineering: A, 2011. **528**(13-14): p. 4556-4563.
98. Savvakis, D.G., et al., *Effect of iron content on sintering behavior of Ti-V-Fe-Al near-beta titanium alloy*. Metallurgical and Materials Transactions A-Physical Metallurgy and Materials Science, 2012. **43A**(2): p. 716-723.
99. Yang, Y.F., et al., *The sintering, sintered microstructure and mechanical properties of Ti-Fe-Si alloys*. Metallurgical and Materials Transactions A-Physical Metallurgy and Materials Science, 2012. **43A**(12): p. 4896-4906.
100. Yang, Y.F., et al., *The effect of Si additions on the sintering and sintered microstructure and mechanical properties of Ti-3Ni alloy*. Materials Science and Engineering: A, 2011. **528**(24): p. 7381-7387.

101. Luo, S.D., et al., *Characteristics of microwave sintering of titanium powder compacts*, in *the 12<sup>th</sup> World Conference on Titanium*, I. Zhou, et al., Editors. 2011, Beijing: Science Press Beijing. p. 1826-1829.
102. Luo, S.D., et al., *Sintering of titanium in vacuum by microwave radiation*. Metallurgical and Materials Transactions A-Physical Metallurgy and Materials Science, 2011. **42A**(8): p. 2466-2474.
103. Luo, S.D., et al., *Novel fabrication of titanium by pure microwave radiation of titanium hydride powder*. Scripta Materialia, 2013. **69**(1): p. 69-72.
104. Hunt, P., *Additive manufacturing at TITANIUM 2012*. Titanium Today, 2013. **1**(1): p. 36-37.
105. Narayan, J., *A new mechanism for field-assisted processing and flash sintering of materials*. Scripta Materialia, 2013. **69**(2): p. 107-111.
106. Olevsky, E., I. Bogachev and A. Maximenko, *Spark-plasma sintering efficiency control by inter-particle contact area growth: A viewpoint*. Scripta Materialia, 2013. **69**(2): p. 112-116.
107. Luo, S.D., et al., *Microwave sintering of titanium*. Key Engineering Materials, 2010. **436**: p. 141-147.
108. Bruce, R.W., et al., *Microwave sintering and melting of titanium powder for low-cost processing*. Key Engineering Materials, 2010. **436**: p. 131-140.
109. Upadhyaya, A., S.K. Tiwari and P. Mishra, *Microwave sintering of W-Ni-Fe alloy*. Scripta Materialia, 2007. **56**(1): p. 5-8.
110. Breval, E., et al., *Comparison between microwave and conventional sintering of WC/Co composites*. Materials Science and Engineering: A, 2005. **391**(1-2): p. 285-295.
111. Saitou, K., *Microwave sintering of iron, cobalt, nickel, copper and stainless steel powders*. Scripta Materialia, 2006. **54**(5): p. 875-879.

112. Zhou, C., et al., *Effect of heating rate on the microwave sintered W–Ni–Fe heavy alloys*. Journal of Alloys and Compounds, 2009. **482**(1–2): p. L6-L8.
113. Buchelnikov, V.D., et al., *Heating of metallic powders by microwaves: Experiment and theory*. Journal of Applied Physics, 2008. **104**(11): p. 113505.
114. Kutty, M.G. and S.B. Bhaduri, *Gradient surface porosity in titanium dental implants: relation between processing parameters and microstructure*. Journal of Materials Science: Materials in Medicine, 2004. **15**(2): p. 145-150.
115. Robson, A.E., R.L. Morgan and R.A. Meger, *Demonstration of a plasma mirror for microwaves*. IEEE Transactions on Plasma Science, 1992. **20**(6): p. 1036-1040.
116. Tomasini, L., et al., *Laser induced stimulated emission for hydrogen atom density measurements in a hydrogen pulsed microwave discharge*. Applied Physics Letters, 1996. **69**(11): p. 1553-1555.
117. Elahinia, M.H., et al., *Manufacturing and processing of NiTi implants: A review*. Progress in Materials Science, 2012. **57**(5): p. 911-946.
118. Akerfeldt, P., R. Pederson and M.L. Antti, *Microstructure and mechanical properties of laser metal deposited Ti-6Al-4V*, in the 12<sup>th</sup> World Conference on Titanium, I. Zhou, et al., Editors. 2011, Beijing: Science Press Beijing. p. 1730-1734.
119. Handtrack, D., et al., *Fabrication of ultra-fine grained and dispersion-strengthened titanium materials by spark plasma sintering*. Materials Science and Engineering: A, 2006. **437**(2): p. 423-429.
120. He, W., et al., *Preparation of ultrafine Ti powder by inhibitor coated/HDH combined method*. Powder Metallurgy, 2013. **56**(3): p. 239-244.
121. He, W., et al., *Fabrication and properties of ultrafine Ti powder by NaCl coated/hydrogenation-dehydrogenation combined method*. The Chinese Journal of Nonferrous Metals (Chinese Version), 2012. **22**(1): p. 158-164.

122. Mishin, Y. and C. Herzig, *Diffusion in the Ti-Al system*. Acta Materialia, 2000. **48**(3): p. 589-623.
123. Yan, M., et al., *Simultaneous gettering of oxygen and chlorine and homogenization of the  $\beta$  phase by rare earth hydride additions to a powder metallurgy Ti-2.25Mo-1.5Fe alloy*. Scripta Materialia, 2012. **67**(5): p. 491-494.
124. Lee, Y.T., et al., *Effect of degassing treatment on microstructure and mechanical properties of P/M Ti-6Al-4V*. Powder Metallurgy International, 1990. **22**(1): p. 11-16.
125. Hill, S.D. and R.V. Mrazek, *Vacuum evaporation of salt from titanium sponge*. Metallurgical Transactions, 1974. **5**(1): p. 53-58.
126. Low, R.J., M. Qian and G.B. Schaffer, *Chloride impurities in titanium powder metallurgy- a review*, in the 12<sup>th</sup> World Conference on Titanium, I. Zhou, et al., Editors. 2011, Beijing: Science Press Beijing. p. 1770-1774.
127. Kashani-Nejad, S., K.W. Ng and R. Harris, *MgOHCl thermal decomposition kinetics*. Metallurgical and Materials Transactions B-Process Metallurgy and Materials Processing Science, 2005. **36B**(1): p. 153-157.
128. Eom, H.C., H. Park and H.S. Yoon, *Preparation of anhydrous magnesium chloride from ammonium magnesium chloride hexahydrate*. Advanced Powder Technology, 2010. **21**(2): p. 125-130.
129. Kashani-Nejad, S., K.W. Ng and R. Harris, *Preparation of MgOHCl by controlled dehydration of MgCl<sub>2</sub> center dot 6H<sub>2</sub>O*. Metallurgical and Materials Transactions B-Process Metallurgy and Materials Processing Science, 2004. **35B**(2): p. 405-406.
130. Long, G.M. and P.H. Ma, *The reaction of MgCl<sub>2</sub> center dot 4H<sub>2</sub>O with CCl<sub>2</sub>F<sub>2</sub>*. Thermochemica Acta, 2003. **403**(2): p. 231-235.
131. Kipouros, G.J. and D.R. Sadoway, *A thermochemical analysis of the production of anhydrous MgCl<sub>2</sub>*. Journal of Light Metals, 2001. **1**(2): p. 111-117.

132. Goso, X. and A. Kale, *Production of titanium metal powder by the HDH process*. Journal of the South African Institute of Mining and Metallurgy, 2011. **111**(3): p. 203-210.
133. Moustydesbuquoit, C., J. Riga, and J.J. Verbist, *Solid-state effects in the electronic-structure of  $TiCl_4$  studies by XPS*. Journal of Chemical Physics, 1983. **79**(1): p. 26-32.
134. Haukka, S., et al., *Dispersion and distribution of titanium species bound to silica from  $TiCl_4$* . Langmuir, 1993. **9**(12): p. 3497-3506.
135. Yu, C.Z. and M.I. Jones, *Investigation of chloride impurities in hydrogenated-dehydrogenated Kroll-processed titanium powders* Powder Metallurgy, 2013. **56**(4): p. 304-309.
136. Seyama, H. and M. Soma, *X-Ray photoelectron spectroscopic study of montmorillonite containing exchangeable divalent-cations*. Journal of the Chemical Society-Faraday Transactions I, 1984. **80**: p. 237-248.
137. Moulder, J.F., et al., *Handbook of X-ray photoelectron spectroscopy*, ed. J. Chastain. 1992, Eden Prairie, MA: Perkin-Elmer Corporation.
138. Siokou, A., D. Kefalas and S. Ntais, *XPS study of hydrated  $MgCl_2$  impregnated on flat  $SiO_2/Si(100)$  Mo and Au substrates*. Surface Science, 2003. **532**: p. 472-477.
139. Sleigh, C., et al., *On the determination of atomic charge via ESCA including application to organometallics*. Journal of Electron Spectroscopy and Related Phenomena, 1996. **77**(1): p. 41-57.
140. Castillo, R., et al., *Influence of the amount of titania on the texture and structure of titania supported on silica*. Journal of Catalysis, 1996. **161**(2): p. 524-529.
141. Jia, Q., et al., *Thermodynamic study of thermal decomposition of magnesium chloride compounds*. Chinese Journal of Inorganic Chemistry, 2011. **27**(8): p. 1529-1535.
142. Esmail, W.A., et al., *The effect of magnesium chloride hydrate on the fire retardation of cellulosic fibers*. Journal of Thermal Analysis and Calorimetry, 2001. **63**(3): p. 831-838.

143. Danes, F.E., E. Saintaman and L. Coudurier, *Thermodynamic Study of the Thermal-Decomposition of Magnesium-Chloride Hydrates*. Journal of Thermal Analysis, 1988. **34**(3): p. 821-833.
144. Henriques, V.A.R., et al., *Production of Ti-13Nb-13Zr alloy for surgical implants by powder metallurgy*. Journal of Materials Science, 2010. **45**(21): p. 5844-5850.
145. Xu, Q., et al., *The development of porous titanium products using slip casting*. Journal of Materials Processing Technology, 2013. **213**(8): p. 1440-1446.
146. Arensburger, D.S., V.S. Pugin, and I.M. Fedorchenko, *Properties of electrolytic and reduced titanium powders and sinterability of porous compacts from such powders*. Soviet Powder Metallurgy and Metal Ceramics, 1968. **7**(5): p. 362-367.
147. Dean, R.S., et al., *Preparation and Properties of Ductile Titanium*. Transactions of the American Institute of Mining and Metallurgical Engineers, 1946. **166**: p. 369-381.
148. Wang, L., et al., *Preparation conditions and porosity of porous titanium sintered under positive pressure*. Materials and Manufacturing Processes, 2013. **28**(11): p. 1166-1170.
149. *Furnace masters difficult metals*. Metal Powder Report, 2004. **59**(6): p. 12.
150. Heaney, D.F. and R.M. German, *Advances in the sintering of titanium powders*, in *Proceedings of the PM2004 Powder Metallurgy World Congress*, H. Danninger and R. R., Editors. 2004, European Powder Metallurgy Association: Vienna, Austria. p. 222-227.
151. Kanto Yakin Kogyo Cooperation: available from [http://www.k-y-k.co.jp/en/sanso\\_e.html](http://www.k-y-k.co.jp/en/sanso_e.html) (accessed March, 2013).
152. Yu, C.Z., P. Cao and M.I. Jones, *Effect of contaminants on sintering of Ti and Ti-6Al-4V alloy powders in an argon-back-filled graphite furnace*. Key Engineering Materials, 2012. **520**: p. 139-144.
153. Matweb: available from <http://www.matweb.com> (accessed January 2013).

154. Matthew J. Donachie, J., *Titanium: a technical guide*. 2nd ed. 2000, Materials Park, Ohio: ASM International.
155. Knacke, O., O. Kubaschewski and K. Hesselmann, eds. *Thermochemical properties of inorganic substances*. 2nd ed. 1991, Berlin: Springer-Verlag.
156. Kuo, D.H. and C.N. Shueh, *Growth and properties of TiCl<sub>4</sub>-derived CVD titanium oxide films at various C-2/H-2 inputs*. *Chemical Vapor Deposition*, 2003. **9**(5): p. 265-271.
157. Kubala, N.G., P.C. Rowlette and C.A. Wolden, *Plasma-enhanced atomic layer deposition of anatase TiO<sub>2</sub> Using TiCl<sub>4</sub>*. *The Journal of Physical Chemistry C*, 2009. **113**(37): p. 16307-16310.
158. Palasantzas, G., G. Krishnan and B.J. Kooi, *Formation and stability of hollow MgO nanoshells*. *Journal of Nanoscience and Nanotechnology*, 2010. **10**(7): p. 4374-4377.
159. Nakamura, R., et al., *Formation of hollow ZnO through low-temperature oxidation of Zn nanoparticles*. *Materials Letters*, 2007. **61**(4-5): p. 1060-1063.
160. Thomas, A., M.M. Titirici and M. Antonietti, *A generalized synthesis of metal oxide hollow spheres using a hydrothermal approach*. *Chemistry of Materials*, 2006. **18**(16): p. 3808-3812.
161. Fujita, T., et al., *Microstructure and properties of titanium alloy produced in the newly developed blended elemental powder metallurgy process*. *Materials Science and Engineering: A*, 1996. **213**(1-2): p. 148-153.
162. Bolzoni, L., et al., *Mechanical behaviour of pressed and sintered titanium alloys obtained from prealloyed and blended elemental powders*. *Journal of the Mechanical Behavior of Biomedical Materials*, 2012. **14**: p. 29-38.
163. Qian, M., *Powder metallurgy of titanium at the 12<sup>th</sup> world conference on titanium*. *Materials China*, 2011. **30**(8): p. 50-53.



164. Huryn, S.V., et al., *Selection of a medium for the carboxidation of titanium alloys*. Materials Science, 2003. **39**(6): p. 835-840.
165. Anisimov, A.S., et al., *Mechanistic investigations of single-walled carbon nanotube synthesis by ferrocene vapor decomposition in carbon monoxide*. Carbon, 2010. **48**(2): p. 380-388.
166. De Barros, M.I., et al., *Influence of internal diffusion barriers on carbon diffusion in pure titanium and Ti-6Al-4V during diamond deposition*. Diamond and Related Materials, 1999. **8**(6): p. 1022-1032.
167. Emamian, A., S.F. Corbin and A. Khajepour, *In-Situ deposition of metal matrix composite in Fe-Ti-C system using laser cladding process*, in *Metal, Ceramic and Polymeric Composites for Various Uses*, Cuppoletti, J., Editor, 2011. p. 33-60.
168. Esteban, P.G., et al., *Low-cost titanium alloys? Iron may hold the answers*. Metal Powder Report, 2008. **63**(4): p. 24-27.
169. Carman, A., et al., *Role of alloying elements in microstructure evolution and alloying elements behaviour during sintering of a near-beta titanium alloy*. Materials Science and Engineering: A, 2011. **528**(3): p. 1686-1693.
170. Kang, K.S., et al., *Reduction characteristics of CuFe<sub>2</sub>O<sub>4</sub> and Fe<sub>3</sub>O<sub>4</sub> by methane; CuFe<sub>2</sub>O<sub>4</sub> as an oxidant for two-step thermochemical methane reforming*. International Journal of Hydrogen Energy, 2008. **33**(17): p. 4560-4568.
171. Neumann, G. and C. Tuijn, *Self-Diffusion and impurity diffusion in pure metals: handbook of experimental data*, in *Pergamon Materials Series*. 2008, The Netherlands, Amsterdam: Elsevier. p. 1-349.
172. Su, Y.Q., et al., *Composition control of a TiAl melt during the induction skull melting (ISM) process*. Journal of Alloys and Compounds, 2002. **334**: p. 261-266.

- 
173. Chen, G., et al., *Effect of aluminium evaporation loss on pore characteristics of porous FeAl alloys produced by vacuum sintering*. Journal of Materials Science, 2012. **47**(3): p. 1244-1250.
  174. Guo, J.J., et al., *Evaporation behavior of aluminum during the cold crucible induction skull melting of titanium aluminum alloys*. Metallurgical and Materials Transactions B-Process Metallurgy and Materials Processing Science, 2000. **31B**(4): p. 837-844.
  175. Langmuir, I., *The vapor pressure of metallic tungsten*. Physical Review, 1913. **2**(5): p. 329-342.
  176. *CRC handbook of chemistry and physics*. 91st ed, ed. W.m. Haynes and D.r. Lide. 2011, Cleveland: CRC Press. Section 4-136.
  177. Porter, D.A., K.E. Easterling and M.Y. Sherif, *Phase transformations in metals and alloys (3rd ed.)*. 2009, Boca Raton, FL: CRC Press.
  178. Miedema, A.R., P.F. de Chatel and F.R. de Boer, *Cohesion in alloys - fundamentals of a semi-empirical model*. Physica B, 1980. **100**(1): p. 1-28.
  179. McCracken, C., *Production of fine titanium powders via the hydrid-dehydride (HDH) process*. PIM International, 2008. **2**(2): p. 55-57.